LIFETIME MEASUREMENTS OF THE NEUTRON-RICH ^{36,38}SI ISOTOPES

By

Mara Mikelah Grinder

A DISSERTATION

Submitted to
Michigan State University
in partial fulfillment of the requirements
for the degree of

Physics - Doctor of Philosophy

2022

ABSTRACT

LIFETIME MEASUREMENTS OF THE NEUTRON-RICH ^{36,38}SI ISOTOPES

By

Mara Mikelah Grinder

The shell structure of nuclei far from stability evolves from the standard shell model picture that accurately describes stable nuclei. Experimental evidence has been given by changes in structural properties of nuclei such as the shell closures. The evolution of shell structure is gradual and must be studied by looking systematically at isotopic or isotonic nuclear chains. Studies of these chains can deepen the understanding of shell structures, magic numbers and the collective natures of nuclei far from stability.

The neutron rich silicon isotopes display evidence of shell evolution seen in the ratio of the low-lying excitation energies. ^{34}Si has a closed shell nature with a proton bubble structure which evolves along the isotopic chain to the absence of the N=28 shell closure expected in ^{42}Si. Another complementary way to probe these changes is by studying the reduced transition rates of the first 2^+ and 4^+ states. The ratio of the reduced transition rates has characteristic values for different collective modes. However, these values are not known for isotopes that are more neutron rich than ^{30}Si. The reduced transition rates can be compared to various theoretical models to understand the changes taking place in this neutron-rich region.

This work discusses an experiment that studied ^{36}Si and ^{38}Si to determine the lifetimes of their excited states and to determine the reduced transition rates of the first 2^+ and 4^+ states in both nuclei. From these B(E2) values, the ratio is calculated and compared to the collective models and shell model calculations. The recoil distance measurement was conducted at the National Superconducting Cyclotron Laboratory using the S800 Spectrograph,

the GRETINA array, and the TRIPLEX plunger. The experiment successfully measured the lifetimes of the 2_1^+ and 4_1^+ states in ^{38}Si and the 4_1^+ and 6_1^+ states in ^{36}Si. Results from the measurement included the confirmation of the 2383-keV state in ^{38}Si that had only been seen once before. The B(E2) values determined from the experiment indicate the reduced collectivity for the first 4^+ states of ^{36,38}Si indicating the persistence of the N=20 magic number through ^{36}Si and ^{38}Si.

Dedicated to Peppernut Grinder.

ACKNOWLEDGMENTS

I would like to thank my research advisor, Dr. Hironori Iwasaki, for guiding me through the Ph.D program and helping me navigating all of the logistics that arose from my funding requirements. His help was invaluable to completing my degree.

Next, I am grateful to my guidance committee, Dr. Alexandra Gade, Dr. Alex Brown, Dr. Laura Chomiuk, and Dr. Wade Fisher for taking time to give great recommendations and suggestions to further improve my thesis work which made this work more complete.

There were a great number of people that contributed to the successful completion of the experiment described in this thesis. I would like to thank the members of the lifetime group for all of their time during the experiments and the discussions had throughout the analysis process. Additionally, the members of the gamma group always provided great support during the experiments. Also, the experiment couldn't have been completed without the help of all of the staff at the National Superconducting Cyclotron Laboratory that all played a role to provide the beam and equipment needed.

To the people who helped further my interests and skills in physics at Eastern Washington University and the Idaho National Laboratory, I am greatly appreciative of all of the time you invested in me. I would not be where I am today without your support and the opportunities you gave me.

Finally, I would like to thank my friends and family. Especially I would like to thank my fellow students Sara and Dayah for always being willing to share tea time and conversation. I will remember some of those discussions forever. I would also like to specifically thank Anne and Doug Park for providing me and my kitten a home away from home. I am extremely grateful for the tech support that my brother Paul provided. And finally, thank you to my

parents, Brian and Joyce Grinder, for giving me the best foundation to succeed in whatever path I chose to follow. There are so many things they have done for me that I will never fully understand the impact of, but they have made me the person I am today.

TABLE OF CONTENTS

LIST OF TABLES . . . . . **ix**

LIST OF FIGURES . . . . . **x**

Chapter 1 Introduction **1**
1.1 Nuclear Landscape 1
1.2 Shell Model 3
1.2.1 Shell Evolution 5
1.3 Collectivity 8
1.3.1 Triaxiality 8
1.4 Nuclear Shapes 10
1.4.1 Bubble Structures 12
1.5 Electromagnetic Transition Strengths 12
1.6 History of Silicon Isotopes 16

Chapter 2 Experimental Methods of Determining Electromagnetic Transition Strengths **21**
2.1 In-Beam Gamma ray Spectroscopy 22
2.1.1 Gamma ray Interactions 22
2.1.2 Doppler Shift and Corrections 24
2.2 Lifetime Measurements 26
2.2.1 Doppler Shift Attenuation Method 27
2.2.2 Recoil Distance Methods 29
2.2.3 Fast Timing Technique 34

Chapter 3 Experimental Devices **36**
3.1 National Superconducting Cyclotron Laboratory 36
3.1.1 SuSI Ion Source 38
3.1.2 Coupled Cyclotrons 39
3.1.3 A1900 Fragment Separator 40
3.1.4 GRETINA 42
3.1.4.1 Addback Method 46
3.1.5 S800 Spectrograph 46
3.1.5.1 The Focal Plane 47
3.1.5.2 The Analysis Line 48
3.1.6 TRIple PLunger for EXotic Beams 49
3.1.7 Experimental Setup 54
3.1.8 Calibration Procedure 55
3.1.9 G4Lifetime Simulations 65
3.1.9.1 Beam Parameters 66

Chapter 4 Lifetime Analysis of ^{36}Si and ^{38}Si **69**
4.1 Silicon Isotopic Chain 69
4.2 Recoil Distance Measurement for ^{36}Si 70
4.2.1 Gamma ray Spectra 74
4.2.1.1 Target Only Data 75
4.2.1.2 Two Foil Data 77
4.2.1.3 Long distance data 80
4.2.2 Laboratory Frame Background 83
4.3 Recoil Distance Measurement for ^{38}Si 85
4.3.1 Gamma ray Spectra 85
4.3.1.1 Target Only Data 85
4.3.1.2 Three Foil Data 87
4.3.1.3 Long distance data 89
4.3.2 Laboratory Frame Background 91
4.4 ^{36,38}Si Lifetime Analysis 91

Chapter 5 Discussion of Results **93**
5.1 Experimental Systematics Along Isotopic Chain 94
5.2 Comparisons to Shell Model Calculations 95

Chapter 6 Conclusion **99**

APPENDIX **101**

REFERENCES **103**

LIST OF TABLES

Table 3.1: This table summarizes the information on which distance settings of the TRIPLEX plunger device were used for each secondary beam produced from the primary beam. The primary beam was used to produce all secondary beams. The distance setting labeled "Target Only" denotes when there was data taken with only the target foil installed in the TRIPLEX for that beam setting. The distance setting for two foil data is the distance between the target and first degrader. For the three foil column, the first number indicates the distance between the target and the first degrader and the second number indicates the distance between the first and second degrader foils. 55

Table 4.1: This table summarizes the information on the characteristic ratios of the yrast energy levels and B(E2) for various types of collectivity. These values are taken from Reference [13]. 70

Table 4.2: This table summarizes the information on the quantities measured in this experiment for the various transitions seen. Table includes the state information including the initial population in percentage, the energy of the state in keV, the energy of the gamma ray emmitted from the state in keV and the lifetime of the state. All lifetimes are as measured in this experiment except for the one marked with a [1], which is the accepted NNDC value. 92

Table 5.1: A summary of the information gathered in this experiment. Lifetimes and B(E2) values for the transitions measured are listed in the table. The lifetime for the 2_1^+ transition in ^{36}Si is taken from Reference [1]. All B(E2) ratios are with the listed transition to the B(E2;$2_1^+ \rightarrow 0_1^+$). 97

Table 5.2: This table summarizes the information from two shell model calculations. The first set of values used the SDPF-MU effective interaction(with tensor component). The second set used the SDPF-MU interaction(without tensor component). The calculations are used to determine the B(E2) values for the even-even isotopes of Si from ^{34}Si to ^{42}Si. A_p and A_n are the bare E2 matrix elements. The B(E2) values were calculated using the effective charges $e_p = 1.35$ and $e_n = 0.35$ for protons and neutrons respectively. 98

LIST OF FIGURES

Figure 1.1: A figure depicting every known nuclei with the y axis being proton number and the x axis being the neutron number of the nucleus. Each nucleus is color coded by its half-life shown in the chart. The nuclei have a very wide range of half-life values covering at least 30 orders of magnitude. Taken from Reference [1]. 2

Figure 1.2: A figure depicting the standard shell model orbitals and the origin of the magic numbers. Taken from Reference [5]. 4

Figure 1.3: Comparison of the energy of the yrast 2^+ state of even-even isotopes in Ca and Si with neutron numbers from 18 to 30. Ca has 20 protons and Si has 14, both considered magic numbers. At N=20, a magic number, both nuclei exhibit an increase in the 2^+ energy level indicating a doubly magic, closed shell nature. As expected at the next classical magic number, N=28, Ca exhibits another increase in the energy. However, in the Si isotope, the expected increase was not observed. Figure comes from Reference [9]. 6

Figure 1.4: An example of the $J_<$ and $J_>$ tensor force causing attractive and repulsive effects to the orbitals. Figure comes from Reference [11]. 7

Figure 1.5: Description of the energy levels of three different collective modes, vibrational, an asymmetric rotor (triaxial nucleus), and a symmetric rotor. Figure comes from Reference [13]. 9

Figure 1.6: Surface plots showing even-even Si isotopes from ^{36}Si at the top of the figure to ^{42}Si at the bottom. The radial axis is related to the deformation parameter β and the angular axis is the gamma parameter γ. The red dot shows the minima of the surface. If the red dot is at 0 degrees, the nucleus is prolate in shape. If it is at 60 degrees, it will be an oblate shape. If the minimum is somewhere in the center of the surface, this indicates a triaxialy deformed nucleus. The left and right column shows the calculation with and without the tensor force [14], respectively. The left column does not include the tensor force in the calculation. Figure comes from Reference [14]. 11

Figure 1.7: The top two figures show the neutron (a) and proton (b) density distributions in the ^{34}Si nucleus. The bottom two figures show the neutron (c) and proton (d) density distributions in the ^{36}Si nucleus. The neutron and proton distributions are very similar in ^{36}S. ^{34}Si displays a reduced density of protons in the center of the nucleus as compared to the neutron density. This is an example of a proton bubble structure. Figure comes from Reference [16]. 13

Figure 1.8: The upper portion of the figure shows the measured γ-ray energies for even-even Si isotopes from ^{26}Si to ^{38}Si. The lower figure shows the measured B(E2; $0^+ \rightarrow 2^+$) values for the same nuclei. Both data sets are compared with Shell model calculations. Figure comes from Reference [19]. 18

Figure 1.9: Energies of the yrast 2^+ and 4^+ states in Si isoptoes with N=22-28(bottom) and the energy ratio R(4/2) (top). Figure comes from Reference [21]. . 19

Figure 1.10: Depiction of ^{38}Si experimental level scheme with transitions on the left compared to a Shell model calculation of the levels on the right. Figure comes from Reference [23]. 20

Figure 2.1: A plot of various direct and indirect lifetime measurement techniques and the range of lifetimes they can measure. Of particular interest is the Recoil Distance Measurement (RDM) that has a sensitive range of 1ps to 10ns. Taken from Reference [33]. 27

Figure 2.2: A schematic describing the basic concept of a three foil Recoil Distance Lifetime Measurement. The top of the figure describes how the different foils work to slow the reaction products created when the beam reacts with the target. The three peaks shown at the bottom of the figure show how a single gamma transition gets broken into three components, one for each foil for which the reaction products interact. The fully shifted peak comes from the decays between the target and first degrader, also called the target component. The reduced-shifted peak comes from the decays between the first and second degrader/stopper and is also known as the reduced component. The unshifted component comes from decays that occur within the stopper/second degrader foil or after the foil, if the beam is not fully stopped within the foil. This component is also known as the slow component where the velocity of the reaction products is the lowest. The figure is taken from Reference [26]. 33

Figure 2.3: A figure showing the mean lifetime measurement of the 2_1^+ state in ^{200}Hg measured using the centroid difference method. The black line shows the standard order for stop and start signals where the red line shows the reversed start and stop signals. The difference in the centroids of these two distributions give 2τ. Figure taken from Reference [38]. 35

Figure 3.1: A schematic of the NSCL from Reference [42] showing a detailed view of the different experimental areas and some of the different detection systems available at the NSCL. 37

Figure 3.2: The above figure depicts a schematic looking down into the NSCL of the configuration of the ion source leading into the K500 and then the K1200 cyclotrons and then into A1900 fragment separator. Taken from Reference [40]. 40

Figure 3.3: Figure (a) shows the geometry of the crystals in each detector module with both types of hexagons labeled A and B. Figure (b) shows the segmentation of each hexagonal germanium crystal. This figure was taken from Reference [49]. 43

Figure 3.4: A photo of the configuration of the nine GRETINA modules for the experiment. The GRETINA crystals are surrounding the beam pipe TRIPLEX plunger device which is mounted in the beam pipe attached to the entrance of the S800 Spectrograph. 45

Figure 3.5: A schematic of the S800 Spectrograph focal plane. This highlights the various detectors including the Cathode Ray Drift Chambers (CRDCs), the ion chamber, the plastic scintilators, and the hodoscope. 47

Figure 3.6: A photo of the TRIPLEX plunger along with a labeled schematic. (A) is the outer casing, (B) is showing one of the piezeoelectric motors, (C) is the outermost support ring for the second degrader, (D) is the stationary middle ring holding the first degrader, (E) is the inner ring that supports the target foil, (F) (G) and (H) are the locations of the target foil, first degrader, second degrader and their holding cones, respectively. The figure is taken from Reference [53]. 50

Figure 3.7: An example of parts of the GUI for controlling the TRIPLEX motors and measurement tools. The figure is taken from Reference [53]. 53

Figure 3.8: A plot showing the spectra of the incoming beam. From this plot an incoming beam gate is made to begin the calibration and particle identification. An example beam gate is shown in red for ^{44}Cl. 56

Figure 3.9: Plots showing the effects of the Timing Scintillator calibrations. The top row is before calibration and the bottom row is after calibration. The left column is the calibration for the AFP, angle at the focal plane, variable. The right column is the calibration for the AFP, x position at the focal plane, variable. The horizontal axis is the measured Time of Flight and the vertical axis is the AFP or XFP measurement respectively. After a proper calibration, the intense blobs will be shifted from a tilted position to being vertical. 58

Figure 3.10: Plots showing the effects of the Ion chamber gain calibrations. The top figure is before calibration and the bottom figure is after calibration. The horizontal axis is the ion chamber channel number and the vertical axis is the response measured in each section. Before the gain matching, each pad has a similar response. After the calibration, the measured response becomes more cohesive across the ionization chamber. 60

Figure 3.11: Plots showing the effects of the CRDC gain calibrations. The top figure is before calibration and the bottom figure is after calibration. The horizontal axis is the CRDC pad number and the vertical axis is the response measured in each section. Before the gain matching, response varied strongly by pad. After the calibration, the measured response becomes more consistent across the CRDC. 61

Figure 3.12: The left figure shows an example of what a mask run data set looks like. The right shows a Reference schematic of the mask plate. A key feature to note is the "L" shaped sequence of dots that allows for the orientation of the plate to be determined. Data is taken in the CRDC just long enough for the positions of the mask holes to become clear enough to calibrate the y positions in the CRDC. 62

Figure 3.13: An example of a fully run-by-run corrected data set. The top row shows the distributions of the Ata variable on the left and the bta parameter on the right. The bottom row shows the Yfp parameter on the left and the Yta parameter on the right. All distributions are centered around zero to give the sharpest PID plot. 64

Figure 3.14: A particle identification plot from the ^{44}Cl secondary beam, target only data set. The vertical axis is the energy loss through the ion chamber and the horizontal axis is the time of flight. Each blob is a different nuclei that has been determined through the calibration process. The blob corresponding to ^{38}Si is centered around (-630, 750). 65

Figure 3.15: This is a figure generated with visualisation packages available in the Geant4 toolkit. It shows a rendered diagram of the GRETINA modules and crystals surrounding the beam pipe holding the foils. The view is looking down the beam axis upstream. This figure is generated with the geometry information given to the simulation. 67

Figure 3.16: Four spectra are used to match beam parameters from data to calibrate the beam information for the simulation. The top left figure show the DTA spectrum, the top right the ATA spectrum, the bottom left the BTA spectrum and the bottom right is the YTA spectrum. Data is shown in blue and the simulated beam is in red. 68

Figure 4.1: The figure shows the ratio of the energy of the gamma transition of the yrast 2^+ and 4^+ states for even-even silicon isotopes. This value is used to understand the collectivity of the nucleus and to understand some characteristics properties of the isotope. The two dotted lines show the theoretical values of the vibrational and rotational limits of this ratio that have been calculated from the energy levels of the perfect harmonic oscillator potential. Data comes from References [1, 9, 13, 19]. 71

Figure 4.2: The figure shows the level scheme of ^{36}Si as taken from the NNDC [1]. The energies of the levels are given on the right and the energy of the transitions are labeled in blue. All energies are listed in keV. 73

Figure 4.3: An example from a three foil ^{38}Si measurement of a two dimensional gamma ray figure. Gamma ray energy in keV is on the x axis and the y axis is the measured gamma ray emission angle (in radians) from the beam axis. The structure around 1074 keV is the $2^+ \rightarrow 0^+$ transition in ^{38}Si. The figure shows how the gamma transition is split into two components (with non-visible third components); one of which is angled and the other being a vertical line. Since the energy of a gamma ray is not Doppler shifted if it is emitted at a 90 degree angle, both components meet at $\pi/2$ radians in the center of mass frame, corresponding to approximately 1.2 radians in the laboratory frame as shown in the figure. Therefore an angle cut corresponding to 40 degrees is used in the multi foil measurement for better peak resolution while minimizing the loss of statistics. 74

Figure 4.4: A gamma ray spectrum showing the Target Only data for ^{36}Si in blue compared with a GEANT4 simulation in red. The small peak on the left is the 6^+ transition and the larger peak on the right is a combination of the 2^+ and 4^+ transitions as they are closer in energy than the resolution of the system due to the effects of the Doppler broadening after the Doppler shift correction. 76

Figure 4.5: This figure shows the gamma ray spectra focused on the two foil data using a 2mm Be target and a 0.58mm Ta degrader for ^{36}Si. The top figure shows the 0mm separation distance data set with the 0.5 mm data set immediately below and the 1mm data set is the bottom spectra. For all three, the data is shown in blue with a comparison with a GEANT4 simulation in red with the 4^+ lifetime being 10ps. 79

Figure 4.6: A gamma spectra showing the effects of neutron background reactions. Data with distance settings 0mm, 0.5mm and 1mm separations are added in the figure. The peak shown on the left is the Doppler shifted component of the ^{27}Al reactions at 850 keV. The small component to the left side of the other feature is the Doppler shifted component of the ^{27}Al reaction and the ^{70}Ge(n,n') reaction around 1000 keV. The right side of the feature around 840 keV is the slow component of the 6^+ transition in ^{36}Si. The is data shown by the cross symbols where the vertical lines represent statistical errors. Simulated neutron background contributions shown in blue below the fit. The red line is the GEANT4 simulation with the added neutron background. 81

Figure 4.7: The long distance ^{36}Si gamma ray spectrum. The distance between the target and first degrader foils was 22mm. This spectra is used to constrain the ratio of reaction products being produced in the degrader as compared with the products being produced in the target foil. 82

Figure 4.8: The top spectrum shows the laboratory frame gamma spectra with the peaks corresponding to the various background reactions. The bottom spectrum shows how these reactions shift in energy after the Doppler shift correction has been applied to reconstruct the ^{36}Si transitions. 84

Figure 4.9: A partial level scheme for ^{38}Si with information experimentally determined by this work. Spin and parities of the states are listed on the left hand side and the energy of the states are listed in keV in black on the right hand side. Transitions that were seen are shown in blue arrows and the energies are in keV in blue. 86

Figure 4.10: The figure shows the target only data for ^{38}Si. Three transitions are visible with gamma ray energies of 1074 keV, 1159 keV, and 1308 keV. . 87

Figure 4.11: The three foil ^{38}Si gamma ray spectrum. The distance between the target and first degrader foils was 1mm and the distance between the first and second degraders was 10mm. This spectra is used to determine the lifetime of the excited states. The red and blue lines show GEANT4 simulations with a simulated 2^+ lifetime of 12ps and 6ps respectively. . 88

Figure 4.12: The long distance ^{38}Si gamma ray spectrum. The distance between the target and first degrader foils was 25mm and the distance between both degraders was also 25mm. This spectra is used to constrain the ratio of reaction products being produced in the degraders as compared with the products being produced in the target foil. 90

Figure 5.1: The left plot shows the known B(E2;$2_1^+ \rightarrow 0_1^+$) values in black and the (E2:$4_1^+ \rightarrow 2_1^+$) values in red for even-even isotopes of Si with Neutron numbers (N) from 20 to 28. The right plot compares the ratio of the B(E2) values for both ^{36}Si and ^{38}Si measured in this experiment and the theoretical ratios summarized in table 5.2. 94

Figure A1: A plot of all isotopes with known B(E2) ratios less than 1. The horizontal axis is the neutron number and the vertical axis is the proton number. The black horizontal lines indicate the standard magic numbers 2,8,20,28,50,82, and 126. 102

Chapter 1

Introduction

1.1 Nuclear Landscape

Nuclei are the central core of every atom. These nuclei are very small, on the order of 10-$^{-14}$m compared to the atomic scale of 10^{-10}m. They are made up of two kinds of nucleons, neutrons and protons. The number of protons in the nucleus will determine the element. For example nuclei with one proton are all hydrogen atoms and nuclei with two protons are all helium. The number of neutrons does not change the element, but the isotope. Nuclei are categorized by their proton number and their total nucleon number. Nuclei are commonly referred to by their chemical symbol determined by the number of protons (Z), such as C for nuclei with Z=6, with a superscript notation for the total number of nucleons A = N + Z. So ^{12}C is a nucleus with Z=N=6.

To visualize all of these nuclei, an organizational chart called the Chart of the Nuclides was developed and can be seen in Figure 1.1. The y axis is the increasing number of protons in the nucleus and the x axis is the increasing number of neutrons. Each square represents a unique nucleus with unique properties. Many kinds of information, including the mass, decay and excitation properties, can be depicted in these charts. This figure shows the half lives of the nuclei. Nuclei that are stable are commonly colored black and form a line in the center of the chart called the line of stability. This chart is continuously being added to with the discovery of new isotopes and other kinds of information, such as the half lives of the

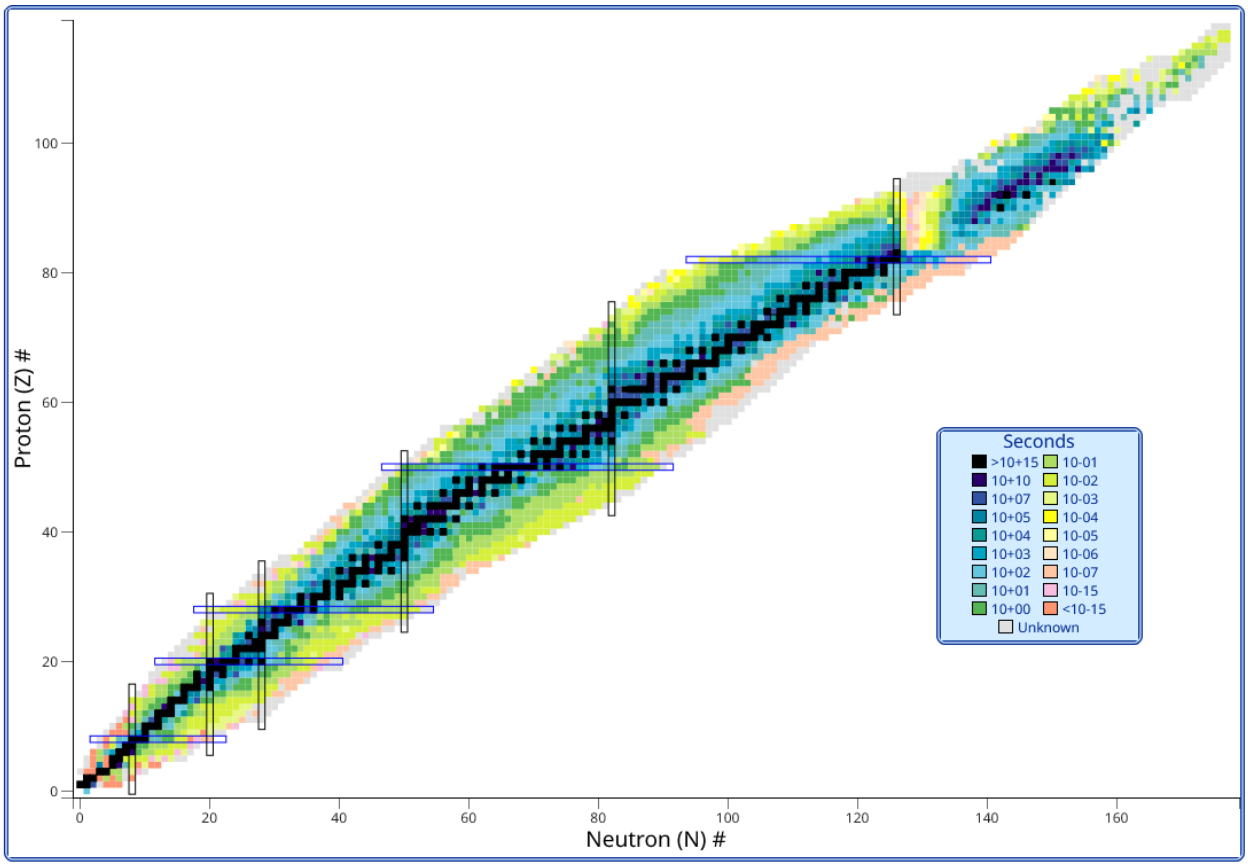

Figure 1.1: A figure depicting every known nuclei with the y axis being proton number and the x axis being the neutron number of the nucleus. Each nucleus is color coded by its half-life shown in the chart. The nuclei have a very wide range of half-life values covering at least 30 orders of magnitude. Taken from Reference [1].

nuclei, while they are being studied throughout the world.

The protons and neutrons inside of a nucleus interact via the strong force. The strong force is what binds specific combinations of protons and neutrons into nuclei that can be studied. The weak interaction is what contributes to nuclear decays. The strong force, plus the Pauli exclusion principle, which states that fermions are distinct particles and must always be distinguishable by their quantum numbers (such as spin and parity) from other fermions, give rise to the intricate structure inside nuclei.

Both protons and neutrons are spin 1/2 fermions (s=1/2) and must occupy a unique state in the nucleus. This means that they do not have the same set of quantum numbers,

such as spin and angular momentum. Since protons and neutrons are very similar particles, the only major difference is that protons have a positive charge and neutrons have zero charge, a quasi-quantum number called isospin can also factor into discussions about nuclear structure. Protons have an isospin value of +1/2 and neutrons have an isospin of -1/2 [2].

1.2 Shell Model

When nuclear properties were studied as a whole using figures like the one in Figure 1.1, certain proton and neutron numbers kept being found to be local maximums or minimums for certain observables. These numbers were deemed magic numbers as they at first seemed to magically change the properties of the nuclei. One way to explain the emergence of these values was a nuclear model called the Shell model [3, 4]. Unlike other models such as the Liquid Drop model, the Shell model is based on a central potential denoted V(r). While this seems like an unlikely choice as the nucleus is held together by a complex set of interactions between all of the nucleons inside of the nucleus, due to the short range of the Strong force the main component of these interactions come from only neighboring nucleons. This causes the central potential to be a reasonable approximation of forces within the nucleus.

The Shell model arranges the nucleons into shells following the Pauli exclusion principle. Since protons and neutrons are distinct particles, there will be a set of shells for the protons and one for the neutrons. Protons and neutrons, however, are very similar with the primary difference being their charges. One consequence of this is that both protons and neutrons have magic numbers. The Shell model uses a three dimensional harmonic oscillator as way to understand these magic numbers. However, while a plain harmonic oscillator can reproduce the first few magic numbers (2,8 and 20), the next magic number, 28 is missing.

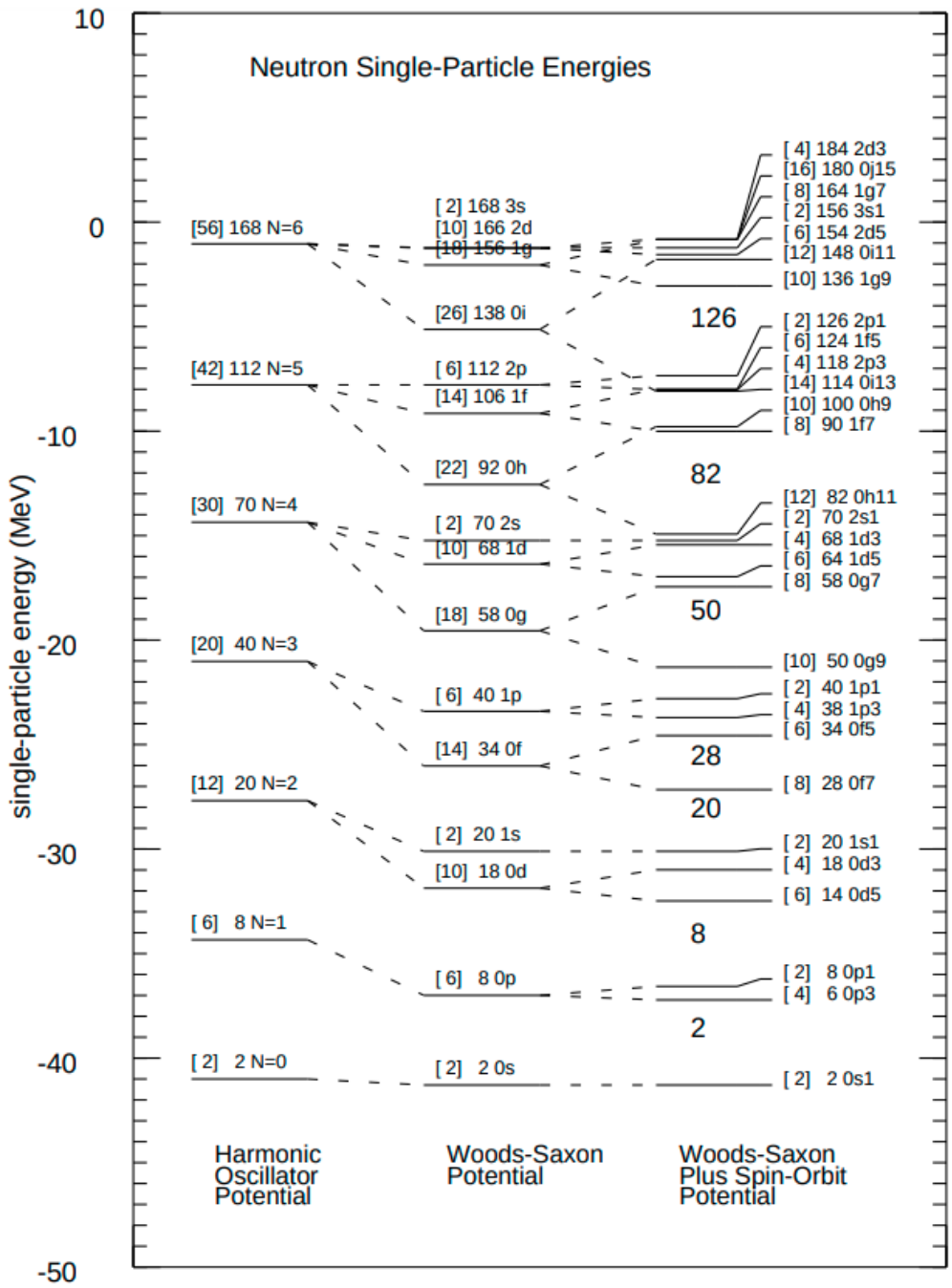

Figure 1.2: A figure depicting the standard shell model orbitals and the origin of the magic numbers. Taken from Reference [5].

The harmonic oscillator solution produces many degenerate energy states. When a second order spin orbital effect is included in the calculation, these energy states split apart. After this additional calculation is added, the magic numbers can be very well reproduced and understood with this model. Figure 1.2 shows the classic shell model levels and their magic numbers.

1.2.1 Shell Evolution

The Shell model can be used to describe trends within the nuclear landscape and has been a powerful tool to predict stable nuclei. However, far from the line of stability, these predictions begin to break down. In one region located around ^{32}Mg, a breakdown occurs of the classic magic numbers seen in the shell gaps. This region is now known as the island of inversion where the standard order of levels changes creating new magic numbers [6–8].

When the standard order of the single-particle orbitals in atomic nuclei changes, traditional magic numbers disappear and new magic numbers can emerge instead. This phenomenon does not happen instantaneously in a single nucleus and can be identified by tracking nuclear properties along the chain of nuclei that share the same proton or neutron numbers, known as isotopic or isotonic chains. By studying the excitation energies and transition strengths of the excited states, the evolution of nuclear properties can be related to changes in the shell structure. An example is given in Figure 1.3 which shows the 2^+ excitation energies measured for Ca and Si isotopes with neutron numbers N=18-30. Magic numbers N=20 and 28 persist in the Ca isotopes, whereas N=28 disappears for ^{42}Si.

One possible explanation of the change in certain energy orbitals can be attributed to a specific portion of the tensor force. This interaction focuses on the proton neutron interaction between two closely related shells between $J_<$ and $J_>$ [10–12]. One is known as the J upper,

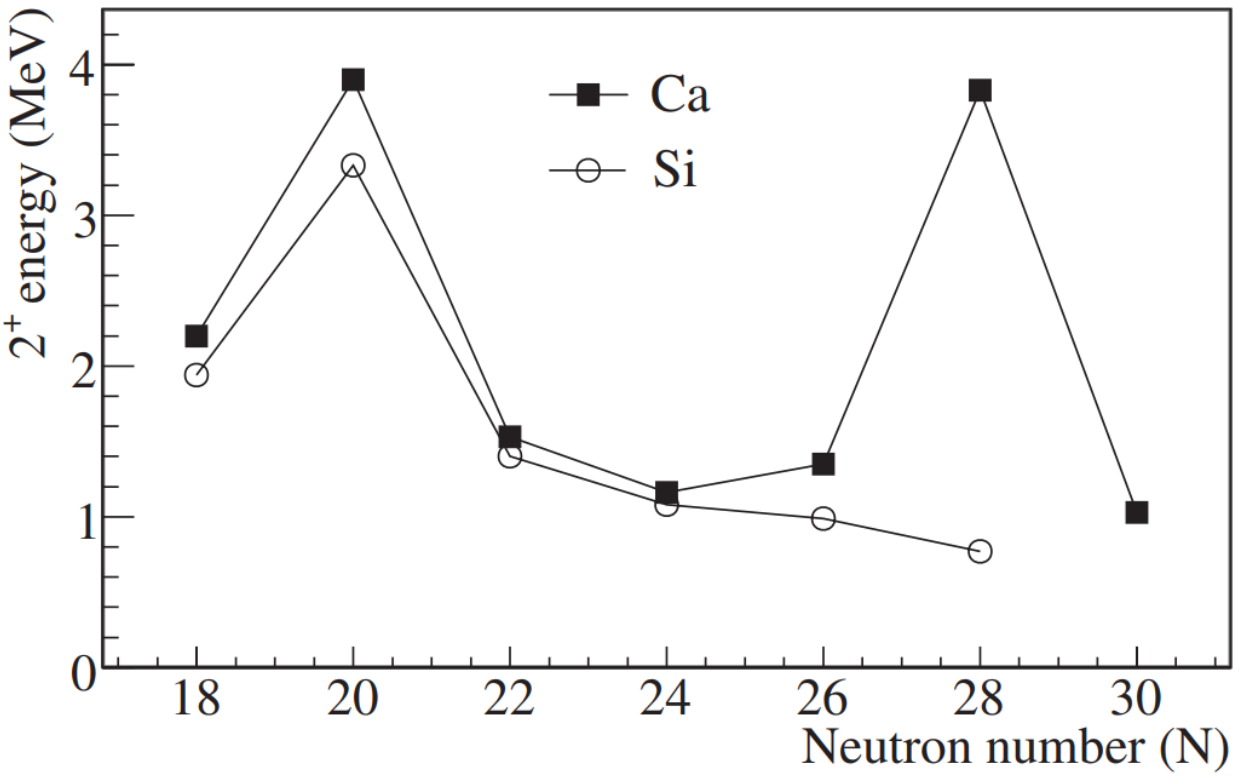

Figure 1.3: Comparison of the energy of the yrast 2^+ state of even-even isotopes in Ca and Si with neutron numbers from 18 to 30. Ca has 20 protons and Si has 14, both considered magic numbers. At N=20, a magic number, both nuclei exhibit an increase in the 2^+ energy level indicating a doubly magic, closed shell nature. As expected at the next classical magic number, N=28, Ca exhibits another increase in the energy. However, in the Si isotope, the expected increase was not observed. Figure comes from Reference [9].

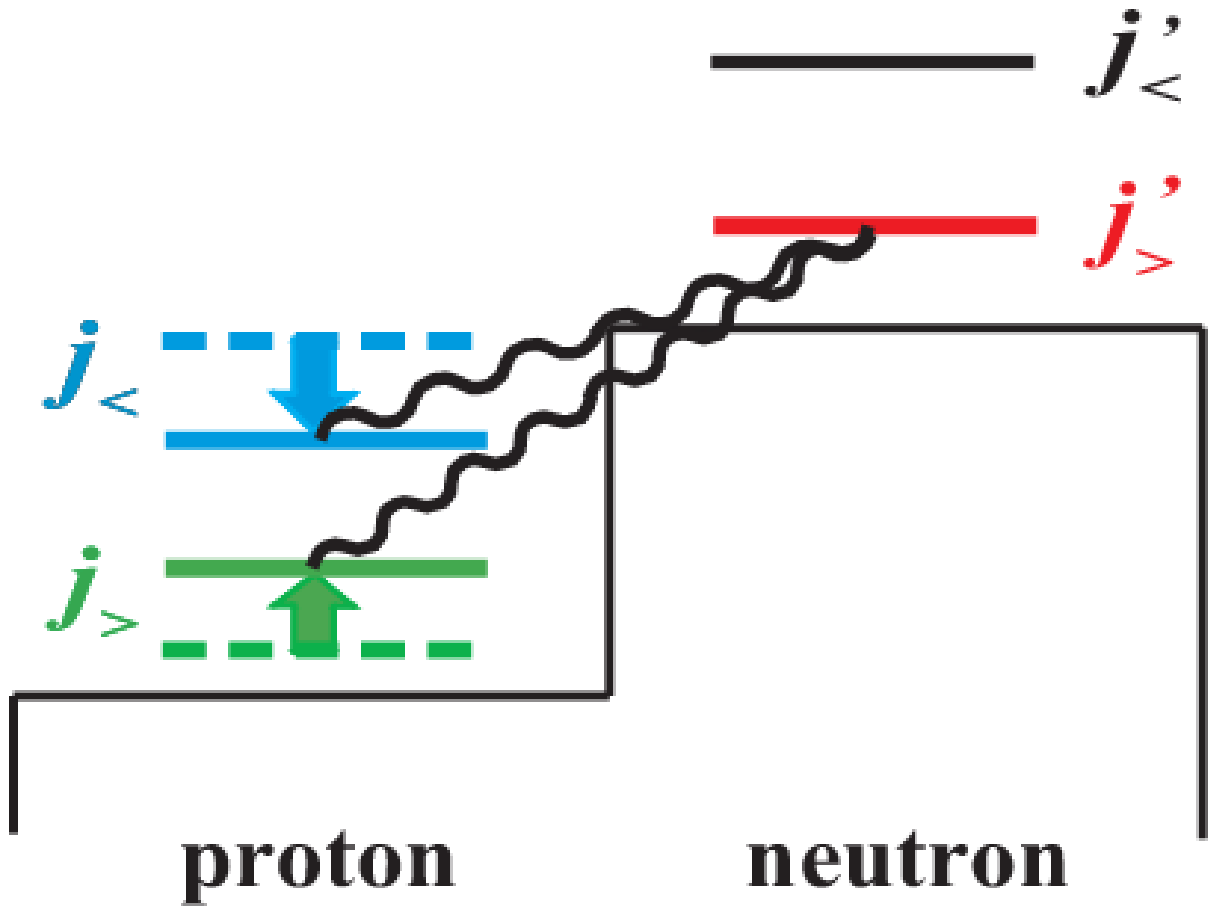

Figure 1.4: An example of the $J_<$ and $J_>$ tensor force causing attractive and repulsive effects to the orbitals. Figure comes from Reference [11].

$J_>$ and is defined as $l+1/2$. The other orbital of interest is the J lower, $J_<$ and is defined as $l-1/2$. This tensor force states that as more nucleons(like neutrons) are added to $J_>$ shells, the attractive interaction with other nucleons (protons) in $J_<$ shells increase. If neutrons and protons are occupied in both $J_>$ or $J_<$ orbitals, the force will be repulsive. A schematic representation of this can be seen in Figure 1.4.

1.3 Collectivity

Nuclei are made up of many protons and neutrons that can either act as individual particles or as more cohesive groups within the nuclei. Collectivity is a measure of how coherent the nuclear motion is and how the particles are behaving as a group. This can simplify a complex many body problem into a simpler few body problem. Several collective modes are useful to discuss such as rotational and vibrational modes and triaxial deformation.

A nucleus is said to be rotational when the nuclei are formed into a symmetric rotor. When the neutrons and protons are continuously moving from a prolate to oblate form, this is known as the vibrational mode. When the nuclei are behaving as an asymmetric rotor with no axis of symmetry, this is known as a triaxial mode. Each one of these modes can be used to calculate the energy ratios of the excited states. They form unique patterns shown in Figure 1.5. From these calculated energies, characteristic ratios of the energy levels and transition strengths can be calculated and used to identify nuclei with these collective modes.

1.3.1 Triaxiality

Triaxiality is a specific collective mode for when there is no axial symmetry in the nucleus. Due to the lack of a symmetric axis, two parameters β and γ need to be introduced to describe the nuclear shape as defined in Equation 1.1. However, the nucleus will still have a characteristic level scheme as seen in the center column of figure 1.5. Due to the lack of a symmetric axis, two parameters, β and γ, need to be introduced to describe the nuclear

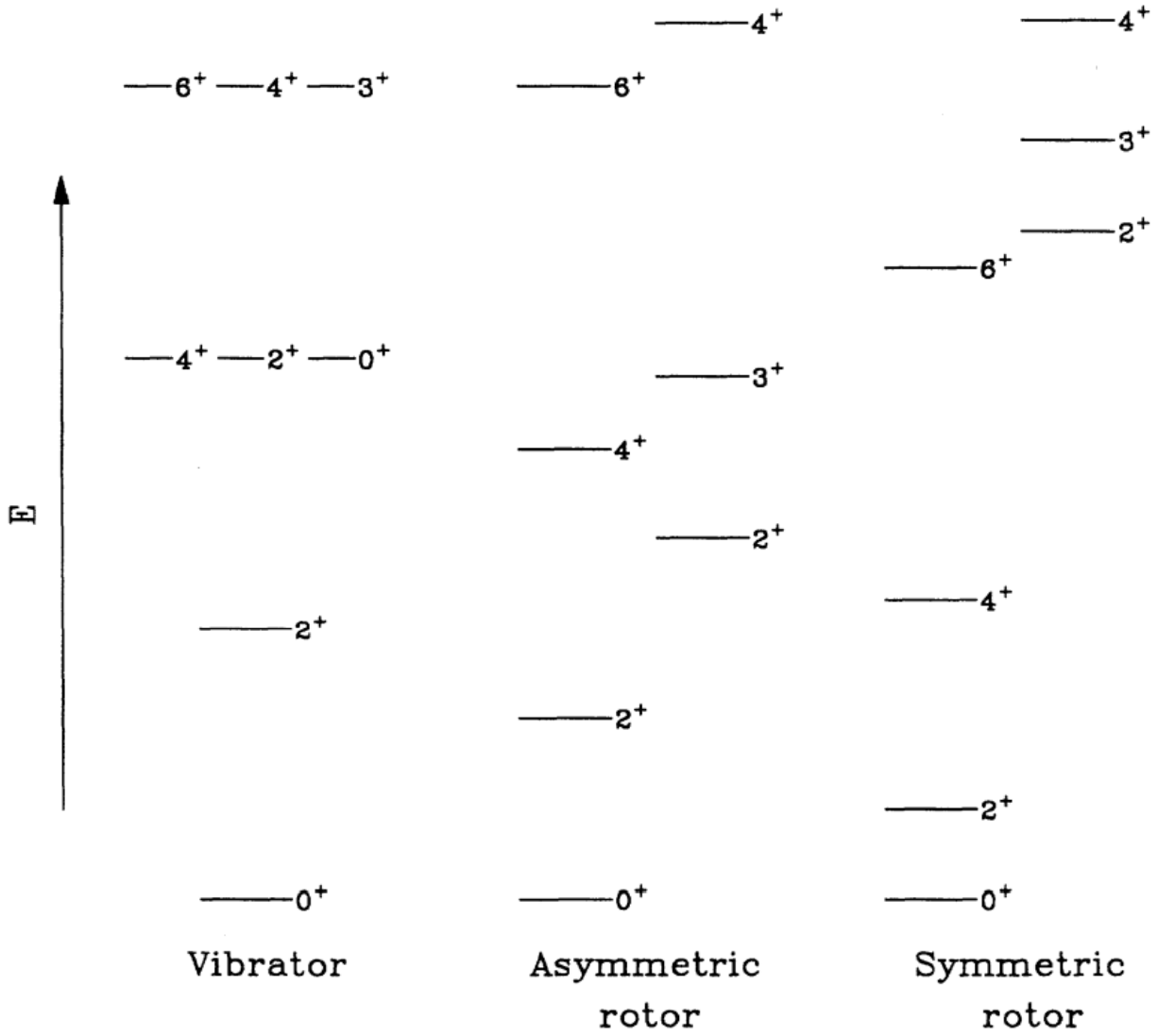

Figure 1.5: Description of the energy levels of three different collective modes, vibrational, an asymmetric rotor (triaxial nucleus), and a symmetric rotor. Figure comes from Reference [13].

shape. The Equation 1.1 describes the deformation:

$$R = R_0 \left[1 + \sum_{\mu} \alpha_\mu Y_{2\mu}(\theta, \phi) \right] \tag{1.1}$$

where R_0 is the radius of a spherical nucleus of the same volume, $Y_{2\mu}$ are the spherical harmonics of order 2, and α_μ are the expansion coefficients. The α_μ get expanded to $\alpha_0 = \beta\cos(\gamma)$ and $\alpha_2 = \alpha_{-2} = \beta\sin(\gamma)$. A β value less than zero indicates an oblate nucleus and a value greater than zero indicates a prolate deformation.

A surface energy plot can be used to predict nuclei with triaxial collectivity. Figure 1.6 shows surface energy plots calculated for silicon isotopes from ^{36}Si to ^{42}Si [14]. When the red dot locating the minimum of the surface is in the center of one of the triangles, this indicates no axis of symmetry and the nucleus is acting as an asymmetric rotor. Based on how deformed the nucleus is it will have a different β value (corresponding to Q_0 in Figure 1.6). Depending on the γ value, the degree of triaxiality changes and the energy levels will have different patterns with the characteristic energy ratios. In this work, $\gamma = 30°$ is taken as the example for triaxial collectivity.

1.4 Nuclear Shapes

Although quadrupole deformation as described in the previous section is one of the fundamental collective modes of nuclei, novel shapes that deviate from the standard spherical, oblate and prolate shapes can appear. One famous occurrence of this is a pear shaped nucleus found for ^{220}Rn and ^{224}Ra; Reference [15]. In these nuclei, the center of charge distribution is off the center of the nucleus, yielding non-zero electric dipole moments(EDM). Further

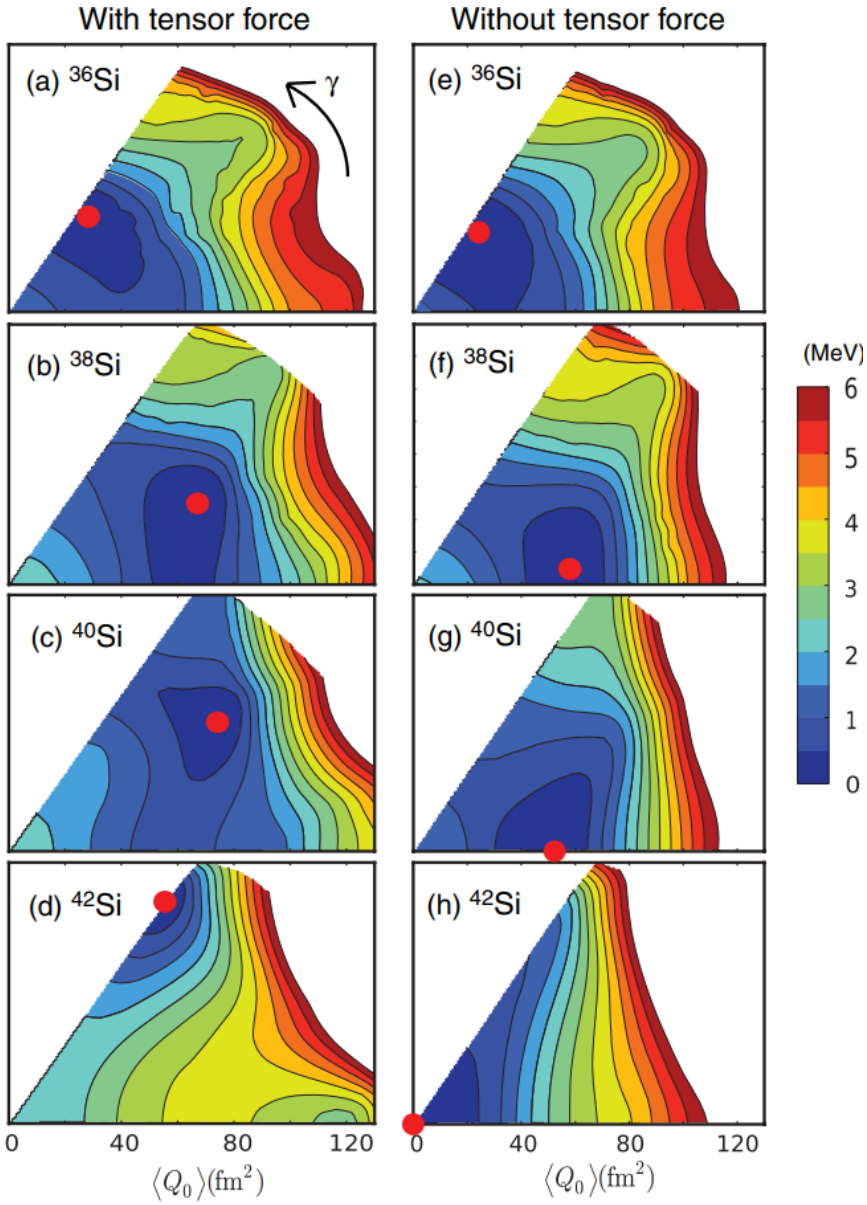

Figure 1.6: Surface plots showing even-even Si isotopes from ^{36}Si at the top of the figure to ^{42}Si at the bottom. The radial axis is related to the deformation parameter β and the angular axis is the gamma parameter γ. The red dot shows the minima of the surface. If the red dot is at 0 degrees, the nucleus is prolate in shape. If it is at 60 degrees, it will be an oblate shape. If the minimum is somewhere in the center of the surface, this indicates a triaxialy deformed nucleus. The left and right column shows the calculation with and without the tensor force [14], respectively. The left column does not include the tensor force in the calculation. Figure comes from Reference [14].

research is being conducted to search for other novel nuclear shapes.

1.4.1 Bubble Structures

An example of unique nuclear shapes that are relevant to the neutron-rich Si isotopes studied in this work is the bubble structure identified for ^{34}Si. When there is a lessening of the neutron or proton density in the center of the nucleus, bubble structures occur. This creates a "bubble" in the center of the nucleus. Figure 1.7 shows the neutron density (left) and proton density (right) in ^{34}Si on the top two figures [16]. The conical depression in the center shows the lack of protons in middle of the nucleus and the other shows how the neutrons are more dense in the center of the nucleus rather than evenly distributed throughout the nucleus. The bottom two figures show the neutron (left) and proton (right) densities for ^{36}S. The neutron distributions are very similar, but the comparison shows the clear decrease in the protons in the center of ^{34}Si.

1.5 Electromagnetic Transition Strengths

Electromagnetic transition strengths are a measure of the overlap in wave functions between two states in a nucleus and can be used to characterize collective modes and nuclear deformation. Excited states in nuclei spontaneously decay into another state. These transitions can be characterized by their lifetimes (τ), which are related to the half-life of the state by Equation 1.2:

$$\tau = \frac{t_{1/2}}{Ln(2)} \tag{1.2}$$

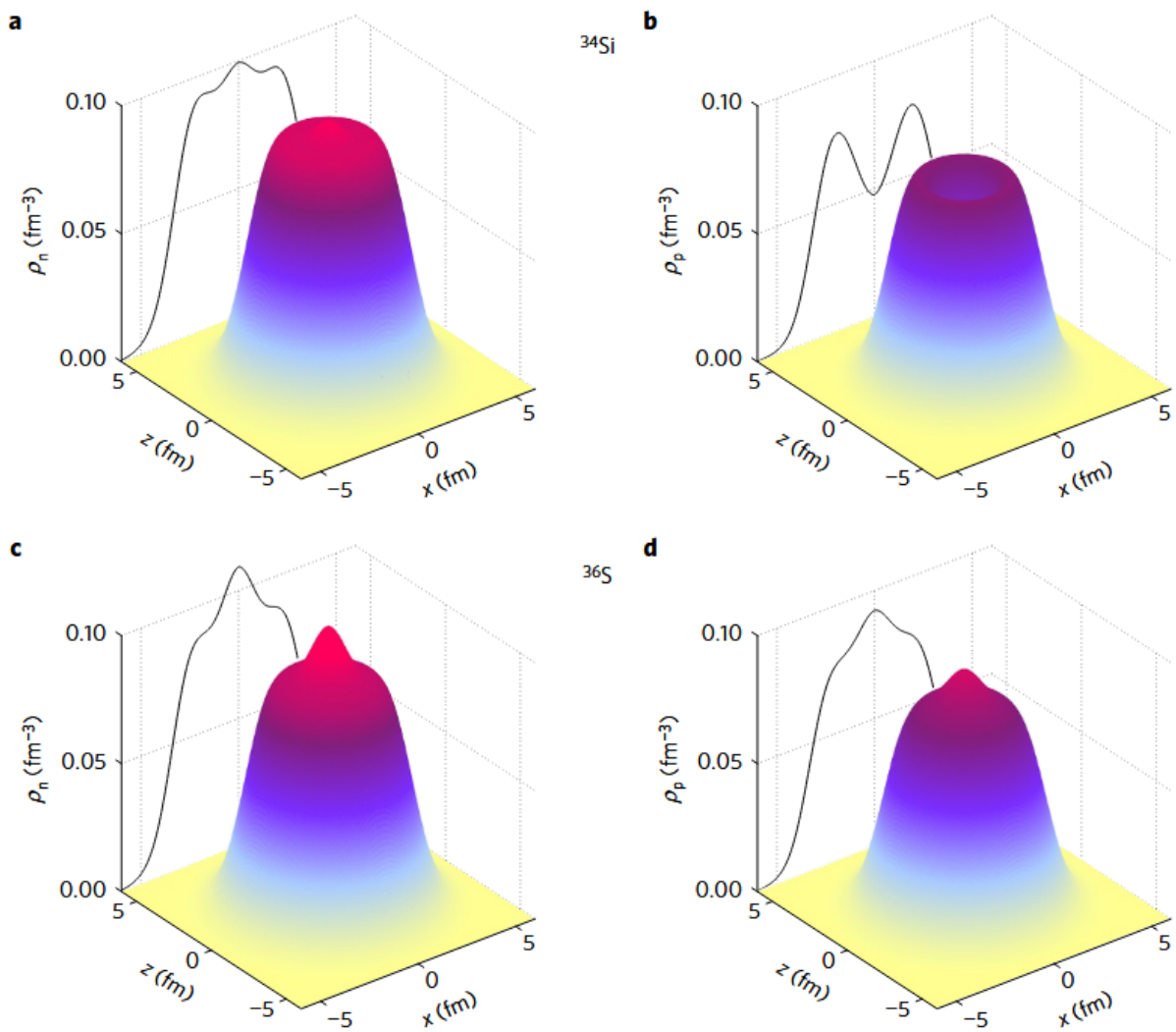

Figure 1.7: The top two figures show the neutron (a) and proton (b) density distributions in the ^{34}Si nucleus. The bottom two figures show the neutron (c) and proton (d) density distributions in the ^{36}Si nucleus. The neutron and proton distributions are very similar in ^{36}S. ^{34}Si displays a reduced density of protons in the center of the nucleus as compared to the neutron density. This is an example of a proton bubble structure. Figure comes from Reference [16].

Where $t_{1/2}$ is the time it takes for half of a sample quantity of the state to decay into a different state. When an excited state decays it releases a form of radiation. The most common carrier of this radiation is a γ-ray, which has a spin value of one [5]. Due to angular momentum conservation, this limits the possible γ-ray decays to one that changes the angular momentum λ. The allowable values for λ for a decay from an initial state, J_i, to a final state, J_f, is governed by equation 1.3:

$$|J_f - J_i| \leq \lambda \leq J_f + J_i \tag{1.3}$$

The strong interaction causes parity to also be conserved. A transition is considered an electric, E, transition when the parity of the transition $\pi = \pi_i \pi_f (-1)^l = 1$, or magnetic, M, when $\pi = \pi_i \pi_f (-1)^l = -1$. Therefore, each transition can be described by their angular momentum and parity, $\pi\lambda$.

The decay rate is characterized by equation 1.4:

$$W = \sum_{\pi,\lambda} \left(\frac{8\pi(\lambda+1)}{\lambda[(2\lambda+1)!!]^2} \right) \left(\frac{k^{2\lambda+1}}{\hbar} \right) \frac{|\langle \Psi_f || O(\pi\lambda) || \Psi_i \rangle|^2}{(2J_i+1)} \tag{1.4}$$

where π is either E or M, k is the wave number of the γ-ray ($E_\gamma/\hbar c$), and λ is the angular momentum. The $|\langle \Psi_f || O(\pi\lambda) || \Psi_i \rangle|^2$ component is the reduced matrix element of the operator O. Of further interest is the reduced transition strength which is the last term and can be written as follows:

$$B(\pi\lambda) = \frac{|\langle \Psi_f || O(\pi\lambda) || \Psi_i \rangle|^2}{(2J_i+1)} \tag{1.5}$$

This averages the impact of the angular momentum terms by using the quantity $(2J_i + 1)$.

The previous equations are used to calculate transition strengths from a lower initial

state, to a higher-lying excited state, $B(i \rightarrow f)$. However, often times it is useful to compare transition strengths that are from the higher-lying state to the lower, notated $B(f \rightarrow i)$. To convert these strengths, the following factor must be included.

$$B(f \rightarrow i) = \frac{2J_i + 1}{2J_f + 1} B(i \rightarrow f) \tag{1.6}$$

The most common electromagnetic transitions are E1, E2 and M1 transitions. The following equations are used to calculate these transition strengths using the half-life and energy of the gamma ray released in the decay.

$$B(E1) = \frac{0.435}{E_\gamma^3 t_{1/2,p}} e^2 fm^2 MeV^3 fs \tag{1.7}$$

$$B(E2) = \frac{564}{E_\gamma^5 t_{1/2,p}} e^2 fm^4 MeV^5 ps \tag{1.8}$$

$$B(M1) = \frac{39.4}{E_\gamma^3 t_{1/2,p}} \mu_N^2 MeV^3 fs \tag{1.9}$$

The $t_{1/2,p}$ is the partial half life of the state and accounts for states that can decay by more than one branch. These reduced transition strengths can be compared to the Weisskopf estimate [17]. Since the Weisskopf estimate assumes a nucleus has single-particle nature, this comparison can be used to discuss the collective motion of the nucleus. If the nucleus has a transition strength that is significantly larger than the Weisskopf estimate the transition is said to be of a collective nature. Equations 1.10 and 1.11 are used to calculate the Weisskopf estimates of electric and magnetic transitions respectively.

$$B_W(E\lambda) = \left(\frac{1}{4\pi}\right)\left[\frac{3}{3+\lambda}\right]^2 (1.2A^{1/3})^{2\lambda} e^2 fm^{2\lambda} \tag{1.10}$$

$$B_W(M\lambda) = \left(\frac{10}{\pi}\right)\left[\frac{3}{3+\lambda}\right]^2 (1.2A^{1/3})^{2\lambda-2} \mu_N^2 fm^{2\lambda-2} \tag{1.11}$$

Reduced transition strengths can be used to study shell closures and the collective natures of nuclei. In order to study nuclear structure, of particular interest for this study are the B(E2; $2^+ \rightarrow 0^+$) and the B(E2; $4^+ \rightarrow 2^+$) to study shell closures and the ratio of B(E2; $4^+ \rightarrow 2^+$)/B(E2; $2^+ \rightarrow 0^+$) to discuss a degree of collectivity of the nucleus.

1.6 History of Silicon Isotopes

The neutron rich isotopes of silicon have been studied over decades since its discovery [18]. The B(E2; $0^+ \rightarrow 2^+$) values for silicon isotopes with N=18-24 were measured for the first time by intermediate-energy Coulomb excitation as described in Reference [19]. Figure 1.8 shows the energy of the first 2^+ state for silicon isotopes from ^{26}Si to ^{38}Si as measured experimentally and compares them with theoretical calculations in the upper portion of the figure. The lower half of the figure shows the B(E2) values for the same set of isotopes. The lowest B(E2) was seen indicating that the expected N=20 shell closure exists in ^{34}Si. Additionally, in 2006 the yrast 2^+ state for ^{40}Si was found to be only 986(5)keV, which is lower than would be expected if ^{42}Si would have a closed shell [20]. This indicated that N=28 may not be a good magic number in this region. The first 2^+ state in ^{42}Si was measured in Reference [9]. The energy of the yrast 2^+ state was found to be 770(19)keV, even lower in energy than the 2^+ state seen previously in ^{40}Si, which confirmed the supposition of the

disappearance of the N=28 shell gap. Figure 1.3 compares the 2^+ energies of the Ca and Si isotopes from N=18 to N=30. The classic shell gaps at N=20 and 28 are seen in ^{40}Ca, ^{48}Ca and ^{34}Si, but the expected rise in 2^+ energy for the N=28 shell gap at ^{42}Si didn't occur.

Reference [21] performed an experiment to measure the 4^+ states in these neutron rich silicon isotopes for the purpose of calculating the $E(4^+)/E(2^+)$ ratio to investigate the deformation through the isotopic chain. Figure 1.9 plots the energies of the first 2^+ and 4^+ states in silicon isotopes from ^{36}Si to ^{42}Si in the lower half of the figure and the upper portion shows the $E(4^+)/E(2^+)$ ratio, which shows that the experimental value transitions from the vibrational limit of 2.0 towards the rotational limit of 3.33 [13, 21].

In 2014 a set of one nucleon knockout reactions were performed to study the changing shell gaps in the Si isotopic chain [22]. The study found that the N=14 shell closure remained up until ^{40}Si, but the N=28 shell gap was non-existent since neutrons were not being hindered in crossing the gap. The robust shell closure at Z=14 for ^{34}Si indicates the absence of the $s_{1/2}$ orbital, demonstrating a bubble structure in which there is an absence of protons in the center of the nucleus as reported in Reference [16]. The neutron and proton density distributions can be seen on the top row of figure 1.7. Finally, detailed spectroscopy on ^{38}Si was performed in Reference [23] and experimental decay scheme is compared for one of Shell model calculations in Figure 1.10. Although the Si isotopic chain has been extensively studied experimentally, there still remains open questions as to how shell model calculations can capture structural changes around ^{42}Si [24], in particular those beyond the first 2^+ state.

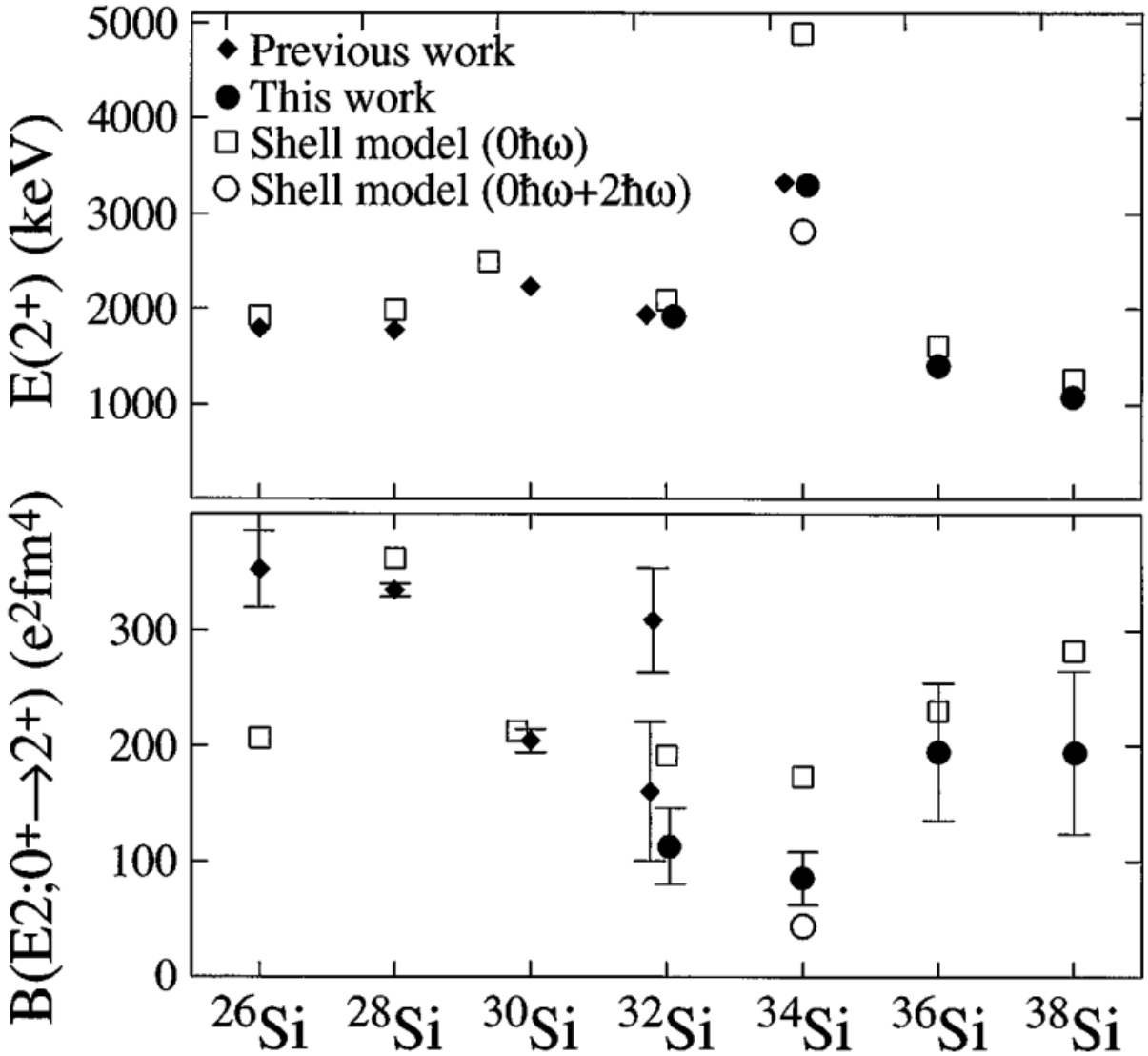

Figure 1.8: The upper portion of the figure shows the measured γ-ray energies for even-even Si isotopes from ^{26}Si to ^{38}Si. The lower figure shows the measured B(E2; $0^+ \rightarrow 2^+$) values for the same nuclei. Both data sets are compared with Shell model calculations. Figure comes from Reference [19].

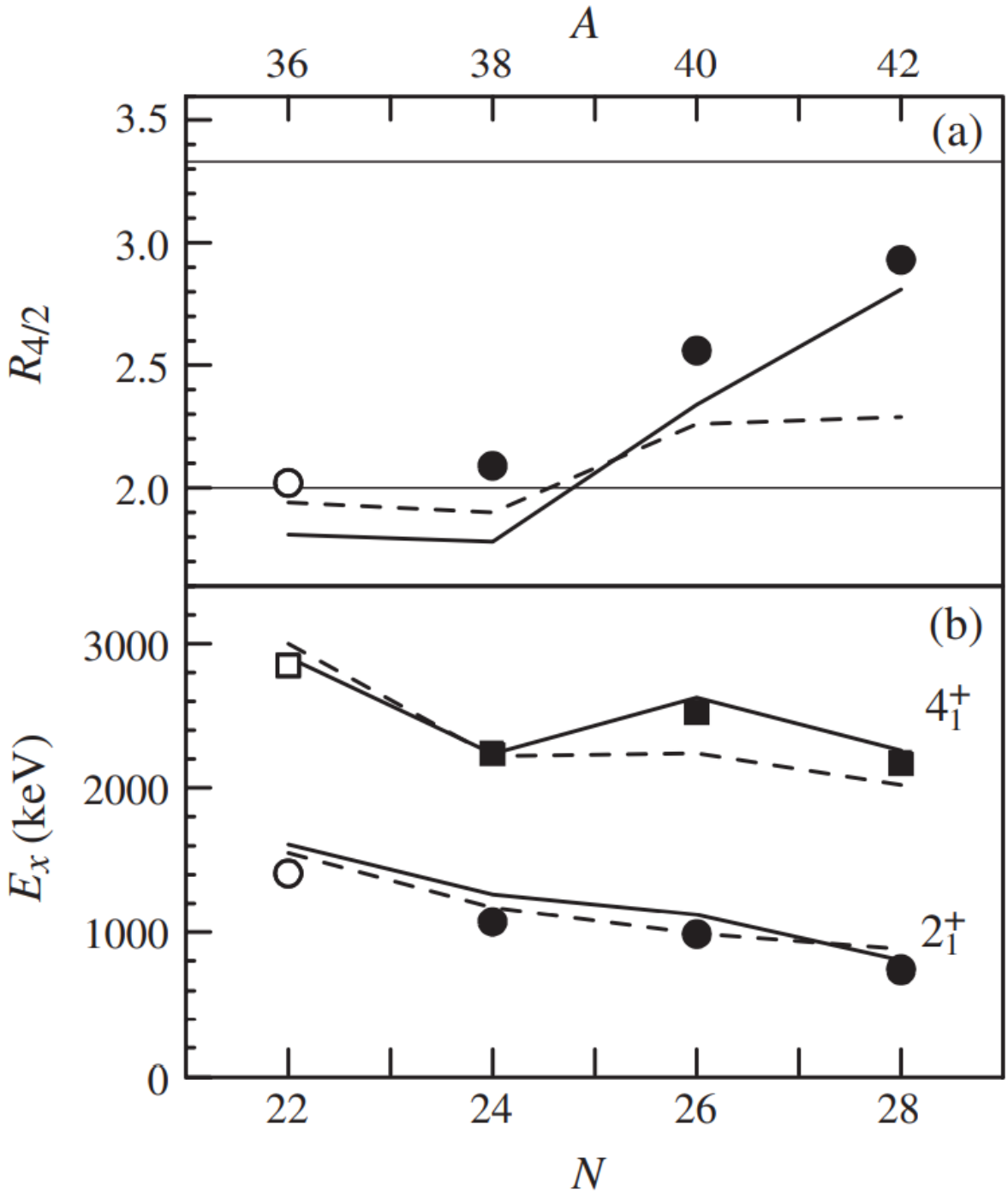

Figure 1.9: Energies of the yrast 2^+ and 4^+ states in Si isoptoes with N=22-28(bottom) and the energy ratio R(4/2) (top). Figure comes from Reference [21].

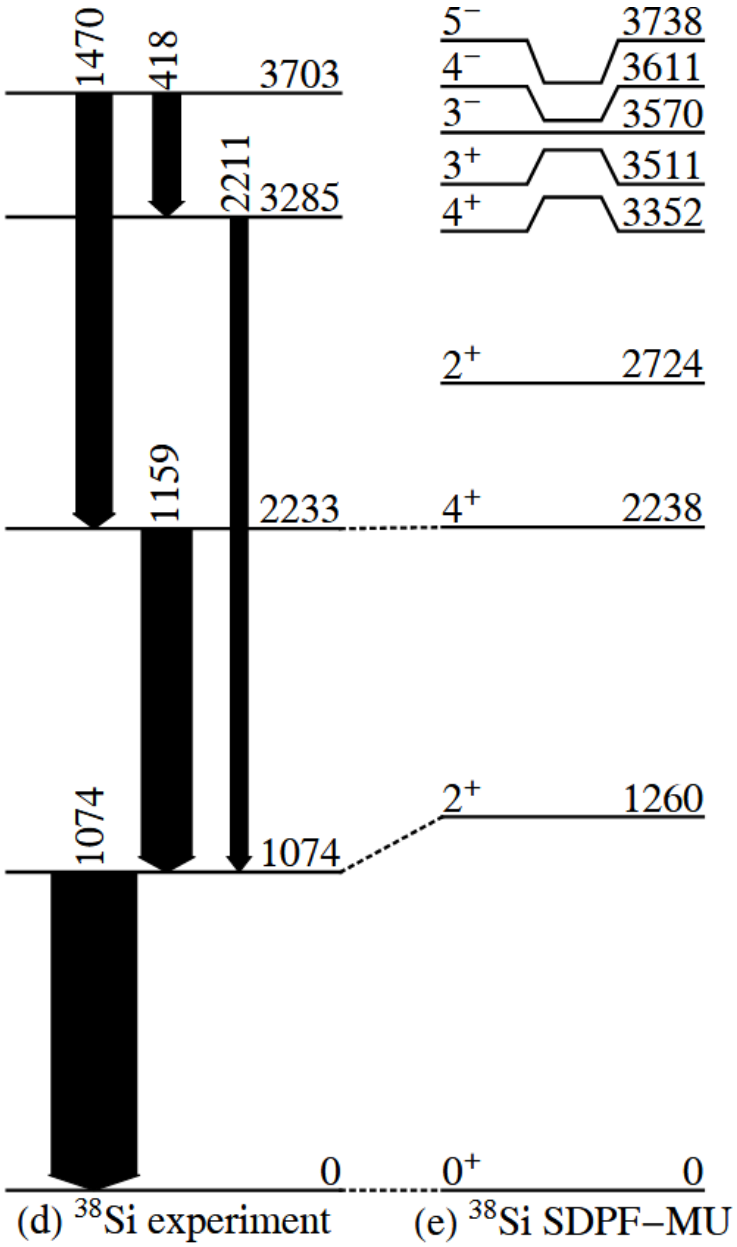

Figure 1.10: Depiction of ^{38}Si experimental level scheme with transitions on the left compared to a Shell model calculation of the levels on the right. Figure comes from Reference [23].

Chapter 2

Experimental Methods of Determining Electromagnetic Transition Strengths

The experiment described in this thesis consists of the application of in-beam gamma ray spectroscopy [25, 26]. In particular the excited states of two nuclei were studied, ^{36}Si and ^{38}Si [26]. The experiment first utilized a ^{44}Cl secondary beam to study the level scheme of ^{36,38}Si and subsequently excited state lifetimes of ^{36}Si. Two foil measurements were performed with the TRIPLEX device. Secondly, a beam of ^{45}Cl was produced to study excited-state lifetimes of ^{38}Si using the three foil setting of the TRIPLEX. Each of the ^{36}Si and ^{38}Si reaction products were identified and gamma rays were observed in coincidence. This made it possible to study the gamma ray transitions from each nucleus of interest.

Discussed in this chapter are various techniques that were used to take the data from the experiment. Some of these techniques include various gamma ray spectroscopy techniques, since a key component of the experiment involved understanding the kinematics of the released gamma rays. Further discussed will be various lifetime measurements, such as the Recoil Distance Method, that were utilized to extract the lifetimes of these excited transitions.

2.1 In-Beam Gamma ray Spectroscopy

In-Beam Gamma ray spectroscopy was initially developed in the 1960-70s [27] to study nuclear excited states following fusion evaporation reactions. The in-beam technique was named to differentiate it from off-beam techniques such as beta decay or activation studies. In the present study, in-beam gamma ray spectroscopy was applied in inverse kinematics, to measure the energy of a gamma ray emitted from a nucleus in flight [25, 28–30]. This requires an in-depth understanding of how gamma rays interact with matter. It also requires knowledge of the kinematics between the gamma ray and nucleus which depends on the speed the nucleus is moving when the gamma ray is emitted.

2.1.1 Gamma ray Interactions

Gamma rays interact with matter primarily through three modes: 1) Photoelectric absorption, 2) Compton scattering and 3) pair production [31].

Photoelectric absorption occurs when the energy in a gamma ray is fully transferred to a nucleus that fully absorbs the energy and there is no remaining energy traveling away as a gamma ray. This process causes the excited nucleus to transfer this energy to a photo electron that then carries the energy as described in Equation 2.1, where E_b is the binding energy of the electron that got ejected from the atom. In most cases, this binding energy is very small compared to the energy of the gamma ray that was absorbed and doesn't affect the accuracy of the gamma ray measurement.

$$E_{e^-} = E_\gamma - E_b \tag{2.1}$$

The photoelectric effect is most prevalent with gamma rays of low energy, below a few

hundred keV, and is enhanced when the Z of the absorbing material is high. Equation 2.2 shows how the absorption coefficient is related to the Z of the absorbing material and the energy of the incident gamma ray and where n is usually between 4 and 5 and is determined from the absorption cross sections of various materials [31].

$$\sigma \propto \frac{Z^n}{E_\gamma^{3.5}} \tag{2.2}$$

Photoelectric effects are most relevant for gamma ray spectroscopy, and therefore materials with high Z, such as Ge, are used as gamma-ray detectors to take advantage of the higher cross sections for photoelectric effects.

Compton scattering occurs when a gamma ray scatters off an electron, transferring a part of its energy to an electron and then scatters away along an angle determined by the kinematic equation shown in Equation 2.3,

$$E' = \frac{E}{1 + \frac{E}{m_0 c^2}(1 - cos(\theta))} \tag{2.3}$$

where E is the initial energy of the gamma ray, E' is the new energy of the scattered gamma ray, m_0 is the electron mass (0.511 MeV) and θ is the scattering angle. The maximum value for this equation, θ equal to π, is where the Compton edge feature will appear. Since Compton scattering relies on scattering off an electron from the target material, the Compton scattering cross section is directly proportional to the Z of the material [31].

Pair production is the third and final way that gamma rays interact with matter. This effect can only occur when the gamma ray energy is at least 1.02 MeV. This is the energy necessary to produce the electron and positron pair. These then annihilate and create two

511 keV gamma rays that can then be seen in the gamma ray detector. This effect is also Z dependant with the cross section being proportional to Z^2 [31].

2.1.2 Doppler Shift and Corrections

Gamma rays that come from a nucleus in motion experience a Doppler shift. This causes the observed energies to be seen at a different energy from the center of mass frame. This then needs to be corrected to obtain the true energy of the gamma ray. The equation 2.4 below shows the relation between the laboratory frame energy, E_{lab}, and the gamma ray energy in the center of mass frame, E_{cm}. This relation depends not only on the energy of the center of mass gamma ray, but also the speed at which the emitting particle is traveling and the angle the gamma ray is emitted as measured from the path of the emitting particle. Therefore, in order to accurately correct for the Doppler shift, the velocity of the recoil nucleus and the gamma-ray emission angle must be able to be measured. This is done by using the detectors mentioned in Chapter 3 and described in detail in Reference [32].

The relation between E

$$E_{lab} = \frac{E_{cm}}{\gamma(1 - \beta cos(\theta))} \tag{2.4}$$

In equation 2.4, γ is the Lorentz factor,

$$\gamma = \frac{1}{\sqrt{1 - \beta^2}} \tag{2.5}$$

where β is defined as the fraction of the speed of light v/c. However, this equation is generally less useful for gamma rays emitted in flight as the usual gamma energy of note is the E_{cm}. Equation 2.6 [26] is equivalent to 2.4 solved for the more relevant quantity E_{cm}.

Equation 2.6 is also useful to understand how lab frame background gamma rays will

behave after the Doppler shift correction is applied. It is necessary to understand where background gamma rays, such as neutron induced reactions on aluminum, will be shifted to see if they will interfere with gamma rays of interest from the studied nuclei.

$$E_{cm} = \gamma(1 - \beta cos(\theta))E_{lab} \tag{2.6}$$

The conversion of Doppler shifted gamma rays back into center of mass frame gamma rays requires two parameters to be well understood, β and θ. This introduces uncertainties in the center of mass gamma-ray energies as it is hard to determine the exact velocity of the emitting particle. The angle, θ, can also have a degree of ambiguity that comes from the ability to determine the exact position of the decay. This causes an effect called Doppler broadening, where the full-energy peak is broader than it would be if the decay occurred from a stopped particle. However, application of the in-flight techniques has a few advantages. With relativistic heavy ion beams more exotic particles can be produced in quantities that would not be possible for short-lived states in a stopped beam experiment giving rise to experiments to study more isotopes farther from stability. Another advantage is the fact that the gamma rays, due to the Lorentz boost, will be forward focused, with an increased solid angle in the forward angles as opposed to a nearly isotropic distribution for the gamma rays from a stopped particle. This allows for the detectors to be arranged in such a way to more efficiently capture the gamma rays from the decays of interest. Since the decay position is related to the lifetime of the excited state, the effect of the distribution of gamma rays in the photopeak can be a lifetime effect giving rise to techniques to measure the lifetime, such as the Doppler Shift Attenuation Method. Other lifetime measurements, such as the Recoil Distance Method, take advantage of the fact that the Doppler shift is sensitive to the

velocity of the beam and utilize degrader foils to purposely slow the beam to create distinct regions of decay.

2.2 Lifetime Measurements

Reaction products created via a beam reacting in a target can be produced in excited states. These excited states will then decay, transitioning to a lower energy state. These decays occur following the radioactive decay formula shown in Equation 2.7.

$$N(t) = N_0 e^{-t/\tau} \tag{2.7}$$

where N is the number of particles remaining as a function of time, N_0 is the initial number of particles and τ is the lifetime. The lifetime of excited states in nuclei gives insight into the structure of the nucleus and give information of the electromagnetic transition strengths that are a useful quantity to understand the collectivity of nuclei, shape co-existance, and configuration mixing.

Various types of methods have been devised to study the lifetimes of excited states in nuclei as illustrated in Fig 2.1. From direct methods, such as the Recoil Distance Method or the Doppler Shift Attenuation Method, to indirect methods, such as Particle Resonance Spectroscopy to Coulomb Excitation, these various methods can measure lifetimes from one attosecond to lifetimes that can be measured in years [33]. Direct measurements are preferred as the lifetime is measured directly and does not rely on theoretical models that require outside inputs. The need to measure this wide range of lifetimes has given rise to many lifetime measurement techniques, a few of which are described here in this chapter: Doppler-Shift Attenuation Method (1fs-1ps), Recoil Distance Method (1ps-10ns) and Fast

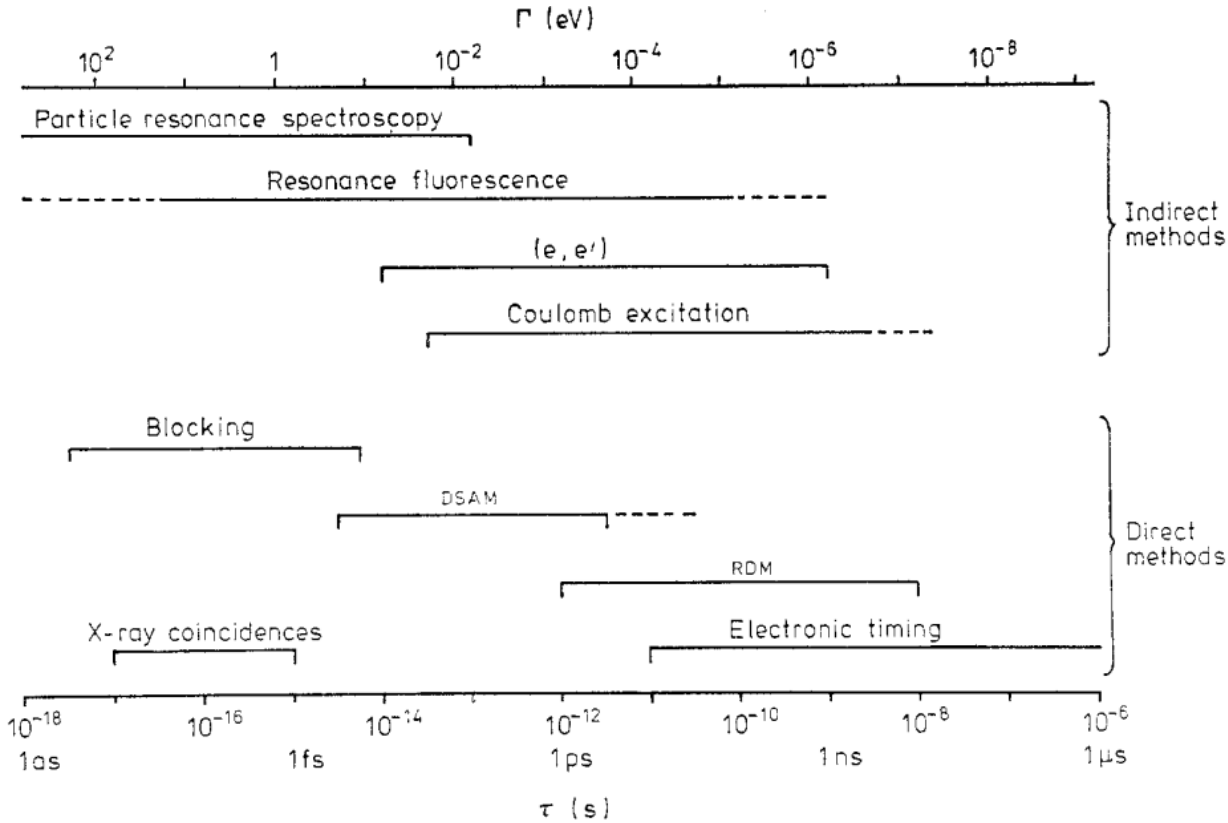

Figure 2.1: A plot of various direct and indirect lifetime measurement techniques and the range of lifetimes they can measure. Of particular interest is the Recoil Distance Measurement (RDM) that has a sensitive range of 1ps to 10ns. Taken from Reference [33].

Timing (>100ps). Only the Recoil Distance Method was used to analyze the data described in this thesis.

2.2.1 Doppler Shift Attenuation Method

The Doppler Shift Attenuation Method (DSAM) [33,34] is a lifetime measurement technique appropriate to directly measure lifetimes of short lived transitions from 1fs($10^{-15}s$) to a few picoseconds ($10^{-9}s$). This technique uses a thick target or a target with a thick backing. The lifetime of the state must be comparable to the time it will take the nucleus of interest to stop in the target. This causes the reacted nuclei to decay within the target as they are being slowed to a stop. This creates a spectrum of velocities of the recoiled nuclei when they

decay. The Doppler shifted gamma rays from the short lived transition will then, after a Doppler shift correction is applied, create a broad photopeak that will have a distribution of events sensitive to the lifetime of the transition being studied.

This technique relies heavily on understanding the velocity of the ion as it travels through the target and backing materials. The average velocity effects the Doppler shift as in the equation below,

$$\bar{E}_{lab} = (1 + \bar{\beta} cos(\theta))E_{cm} \tag{2.8}$$

where $\bar{\beta} = \bar{v}/c$ and $\bar{v}$ is a theoretical function of the lifetime. Since the ion must be stopped, often high Z materials like tantalum are used as a backing material. It is critical for this technique to accurately define the stopping power of the ion traveling through the target and stopper materials. The stopping of an ion in a material is a complex process that has many components including electronic and nuclear stopping processes, due to interactions such as the electrons of the stopping material interacting with the electrons of the traveling particle or interactions between the traveling particles and the electrons or nuclei of the stopping material. This is predominantly a statistical process and is usually determined from one of many models created to understand this complex interaction. Simulations that incorporate the use of these models can be used to constrain the uncertainties or ambiguities from assumptions in the various models and are used to compare with the data to determine the lifetime value of the short lived transition.

2.2.2 Recoil Distance Methods

The Recoil Distance Method (RDM) was developed to study lifetimes from 1ps to 1ns ($10^{-12}s - 10^{-9}s$). The first examples of this technique relied on stable beams at low energies, such as in Reference [26]. RDM measurements use a device called a plunger. This plunger device holds foils, traditionally a target foil and a stopper foil, inside the beam line and allows the distance between them to be accurately controlled. During a measurement, the plunger is installed in the beam line which is surrounded by gamma ray detectors. The beam encounters the target foil first, where a nuclear reaction occurs, and the remaining beam and the created reaction products continue moving down the beam line to the stopper, where the reaction products are stopped. The nuclear reaction produces the nuclei of interest in an excited state. The types of states that are populated depend on the kind of nuclear reaction that occurs.

These excited states then decay by gamma ray emission either while they are in motion or when they have been stopped in the stopper foil. If they were in between the foils, the gamma rays will experience a Doppler shift and will need to be corrected as described in a previous section. The lifetime, τ, is defined as the time it takes for the initial population of unstable particles to decay by 1/e, where e is Euler's constant. The position of decay gives information on the lifetime of the excited state as, very roughly, x=vt where x is the position of the decay, v is the velocity of the nucleus of interest and t is the time to decay, which is related to τ. The lifetime τ should not be confused with the half life, which is defined as the time it takes the initial population to decay by half. In this document, the lifetime τ is used to describe the lifetimes of excited states.

The decays are then observed in the gamma ray spectra. If the distance between the

target and stopper foil is close to the distance x=vτ, two peaks will be observed for each transition. One will be the Doppler shifted peak for the gamma rays emitted from the in-flight nuclei after the target foil, and it is called the fast peak. The other unshifted peak from the nuclei stopped in the stopper foil is called the stopped peak. The heights of these two peaks then give lifetime information as they measure the number of decays happening either between the two foils or in the stopper. If reactions in the stopper foil can be ignored, it is still necessary to constrain feeding effects from higher-lying states before calculating the lifetime. However, if a fast beam is used, such as a rare isotope beam this method needs to be modified.

In any RDM measurement, there are two major variables that effect the heights of the different peak components, the distance between the foils and the lifetime of the state. Since the lifetime is the value being studied, it is critical that care is taken to reduce uncertainty in the distance between the foils. This distance was calibrated for the experiment discussed in this thesis in a process described in Chapter 3. It is preferred to take data with multiple distance settings to understand not only the lifetime of the state but also feeding effects from higher-lying states.

RDM measurements using a fast beam are generally not fully stopped but only slowed by foils subsequent to the target foil. These foils, since they do not stop, but only slow the beam, are referred to as degrader foils. The higher energy of the beam also allows for a second optional degrader to be used to create three distinct sections that can then be sensitive to a greater lifetime range in one measurement. Thicker foils may also be used to increase the production of the isotope of interest. This does increase the chance of secondary reactions in the degrader foils that must be constrained for a proper measurement.

Despite additional challenges, fast rare isotope beams greatly improve experimental fea-

sibility to study more exotic nuclei than was possible with stable beams. Fast beams also allow for the possibility of identification of the products as the reaction products are not fully stopped, but continue along the beam line. If the beam line is connected to a spectrometer, isotope gating allows for a great reduction in the background in the gamma ray spectra which makes even relatively low beam rate experiments possible.

There are several key differences to a RDM using fast beams due to the many factors that need to be constrained. One of which is the secondary reactions in the degrader foils. These reactions will be of the same quantity for each distance as long as the beam parameters are not changed and these quantities are not affected by changing the distance between foils as this causes no change in the beam nor in the foil material. Therefore, at least two distance settings are measured to be able to constrain the reactions in the degrader foils. Additional data sets are used to calibrate a simulated beam that is used to compare various lifetimes of the excited state to the lifetime sensitive data set.

In a three foil measurement [35, 36] as applied in this work, three foils are mounted into the plunger device, a target foil, a first degrader foil, and a second degrader foil. When the beam reacts in the target, the reaction products travel down the beam line at roughly one third the speed of light. As they pass through the first degrader they lose energy and as they transit to the second degrader they travel at a reduced velocity. After passing through the second degrader, they continue traveling even slower down the beam line. These nuclei are created in an excited state and decay along their path. These gamma rays are all Doppler shifted, with three different β values. The gamma ray spectra are corrected with one β value, chosen from either the β value after the target, after the first degrader, or after the second degrader. Since each section of the plunger has a different velocity, schematically shown in Figure 2.2, three distinct peaks will be formed after the corrections are applied to the gamma

ray spectra. These three peaks are called the fast, reduced, and slow peaks, referring to the relative velocity of the reaction products that contribute to each peak.

As discussed above, the relative heights of these peaks give valuable information sensitive to the lifetime of interest, although other effects such as feeding effects and contributions from the reactions that occur in the degrader foils need to be taken into account. For the data studied in this thesis, the beam was traveling around 40% of the speed of light. This corresponds to a nucleus traveling roughly 1mm of distance down the beamline in 10ps. However, if the transition of interest is in a cascade, feeding effects from higher lying states can considerably affect the distribution between the Doppler shifted peaks for lower energy transitions populated from these feeder states.

A strong feeding component from a higher lying state can significantly change the perceived lifetime of a lower transition, effectively increasing its lifetime in the obtained result. This is due to the fact that the decay time is not just the decay of the transition, but the combined effects of the lifetimes of the transition and the feeder states. To correct for this feeding, the contribution due to feeding must be understood, constrained and incorporated by considering the initial population of the higher lying feeder states, their branching ratios and their lifetimes. This allows the contribution from feeding to be constrained and separated from the lower lying states of interest. This is done with careful modeling in the simulation of the level scheme.

A Monte Carlo based simulation is used to help understand variables in the experiment. Many different calibration data sets are taken to properly constrain many variables. These data sets include a long distance beam setting that sets the distances between foils to be very large, several τ, to allow most of the reaction products to decay before encountering the next foil. This gives a measurement of the relative number of reaction products produced in each

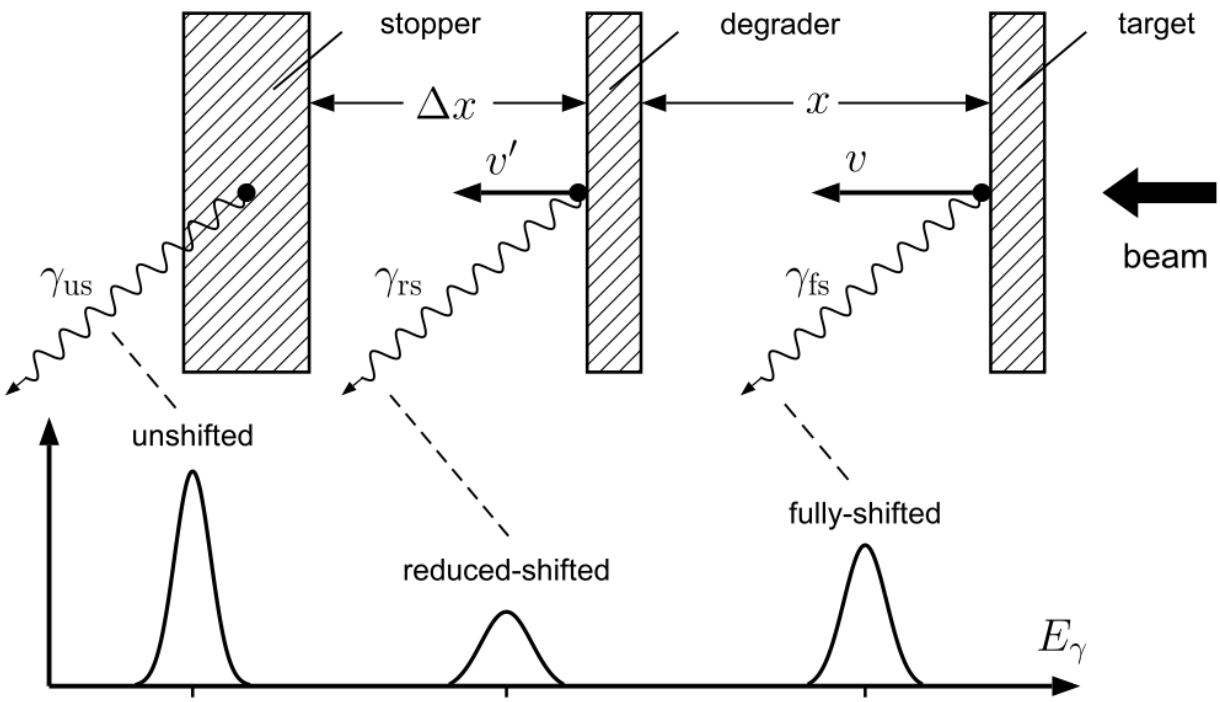

Figure 2.2: A schematic describing the basic concept of a three foil Recoil Distance Lifetime Measurement. The top of the figure describes how the different foils work to slow the reaction products created when the beam reacts with the target. The three peaks shown at the bottom of the figure show how a single gamma transition gets broken into three components, one for each foil for which the reaction products interact. The fully shifted peak comes from the decays between the target and first degrader, also called the target component. The reduced-shifted peak comes from the decays between the first and second degrader/stopper and is also known as the reduced component. The unshifted component comes from decays that occur within the stopper/second degrader foil or after the foil, if the beam is not fully stopped within the foil. This component is also known as the slow component where the velocity of the reaction products is the lowest. The figure is taken from Reference [26].

foil. Other data sets include target only data to constrain populations of each transition, and several data sets which are used to constrain beam parameters and determine the velocity of the beam between the foils. These data sets are in addition to the lifetime sensitive data sets that are taken to constrain the lifetimes of the states of interest.

2.2.3 Fast Timing Technique

The Fast Timing technique is a direct method of measuring the lifetime of an excited state using $\gamma - \gamma$ coincidence techniques. Unlike the previously mentioned Doppler Shift Attenuation Method and the Recoil Distance Measurement that rely on understanding and correcting for the Doppler shift effect, fast timing techniques instead use the timing difference between two detectors to directly measure the decay time of an excited transition [37]. This requires detection of a gamma transition that populates the state of interest and the detection of the deexcitation from this state. The gamma ray signal that evidences the population of the state whose lifetime is being measured is usually the start signal and the signal from the deexicitation gamma ray is the stop signal. Therefore, the time between these two signals can be statistically analyzed to determine the lifetime of the excited state.

The limitation in determining the time difference between these two signals is highly dependent on the timing resolution of both detectors. If the timing resolution is too large in comparison to the lifetime of the state of interest, the start and stop signals are not well separated and are harder to define as separate moments. The quality of these signals is also dependent on the choice of gamma ray that is used as the population signal and the branching ratio of the state. Therefore, appropriate care must be taken when choosing a detector for a fast timing measurement. Three factors: 1) energy resolution, for gating on the gamma rays, 2) timing resolution, for resolution of start and stop signals, 3) and efficiency, to increase $\gamma - \gamma$ coincidence statistics, must be considered. One choice has been the $LaBr_3$ detectors such as the ones in Reference [37]. Other considerations for fast timing measurements include the choice of the photomultiplier tube used with the detector crystal used.

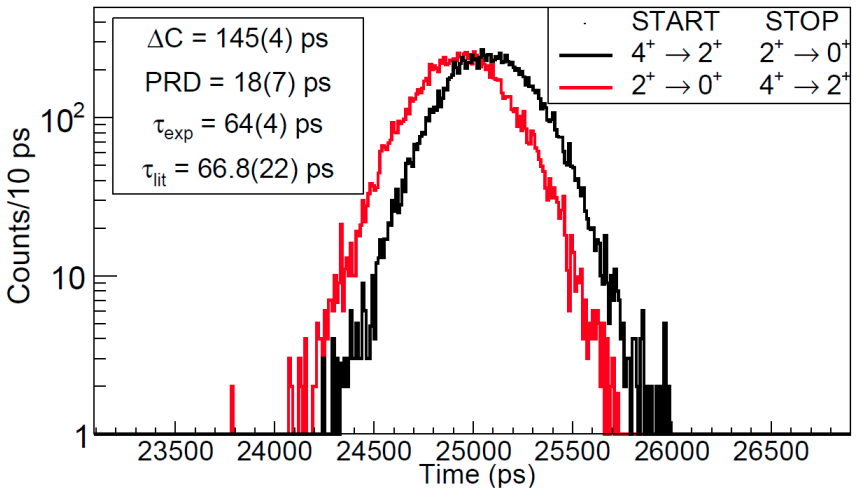

Figure 2.3: A figure showing the mean lifetime measurement of the 2_1^+ state in ^{200}Hg measured using the centroid difference method. The black line shows the standard order for stop and start signals where the red line shows the reversed start and stop signals. The difference in the centroids of these two distributions give 2τ. Figure taken from Reference [38].

After the physical detection system is established a Digital Data Acquisition System can also be developed to handle the precise time measurements required by this technique. The GRIFFIN system [38] at TRIUMF has been used for fast timing measurements. $LaBr_3$ detectors were utilized along with a specific fast scintillator at 90 degrees for the fast timing measurements. Additionally, a fast timing method using the centroid difference method was used to measure mean lifetimes, τ, greater than 100ps. This method reverses the standard start and stop signals to measure "negative" lifetime such that the centroid shift between the standard start and stop signals and the reversed start and stop signals measure 2τ to suppress systematic errors. All of these methods require careful choice of signal processing to reduce the energy resolution's effect on the rise time of the signals so that the errors in the calculation of a signal's time are minimized.

Chapter 3

Experimental Devices

3.1 National Superconducting Cyclotron Laboratory

The National Superconducting Cyclotron Laboratory (NSCL) is located on the campus of Michigan State University in East Lansing, Michigan. It is used for the purpose of creating rare isotopes that are too short lived to be able to be studied any other way. Studying these isotopes can lead to advancements in astrophysical science, basic science research such as nuclear structure and reactions as well as fundamental physics. The first cyclotron on the MSU campus, the K50, was a non-superconducting cyclotron that was able to produce beams of 50 MeV [39]. The K500 cyclotron, the first superconducting cyclotron, came online in 1981. A second cyclotron, subsequently called the K1200, was added to the facility in 1988 to run independently. By the year 2000, the K500 and the K1200 cyclotrons had successfully been linked together into the Coupled Cyclotron Facility [40] that was used for the experiment discussed in this dissertation. Currently, another upgrade is occurring at this facility. The Facility for Rare Isotope Beams (FRIB) [41] has been built to expand the range of rare isotopes able to be studied and to utilize the existing experimental equipment available at the NSCL. The expansion includes building a new superconducting linear accelerator and upgrading the ion sources.

Figure 3.1 shows the layout of the current available facilities. The beam line begins at the ion source. The SuSi ion source is an electron cyclotron resonance source that produces

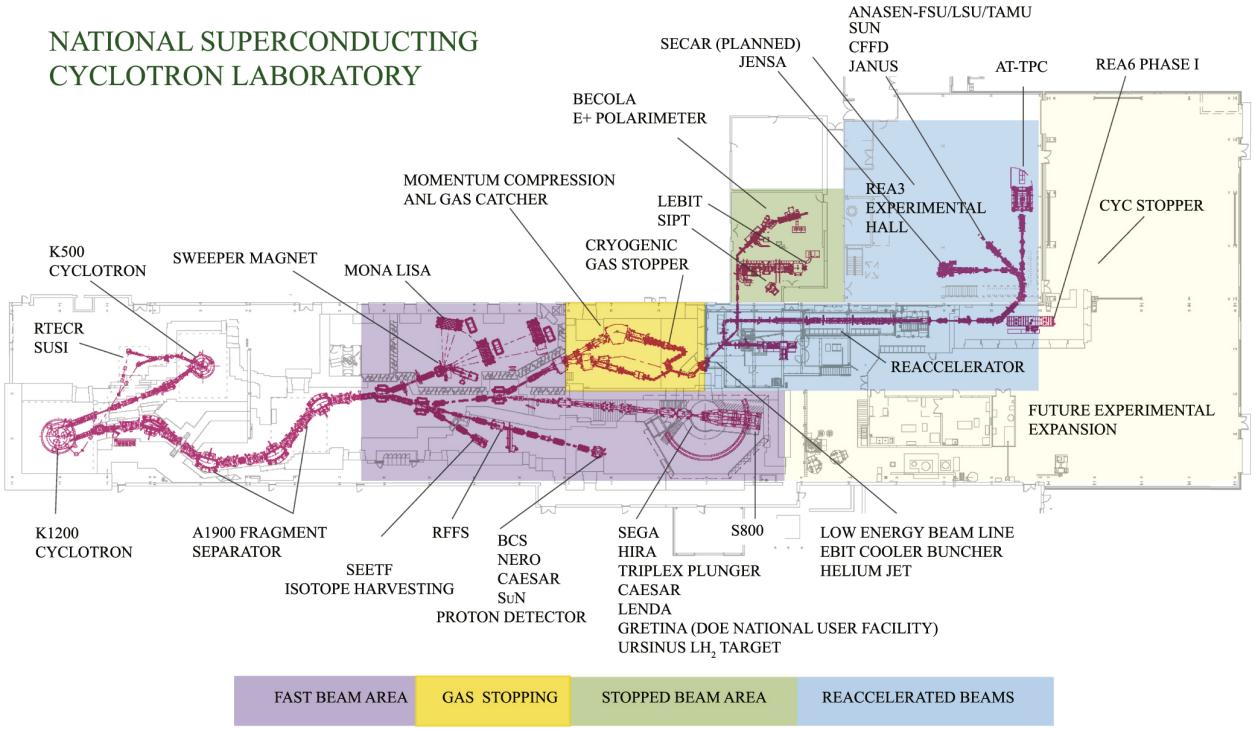

Figure 3.1: A schematic of the NSCL from Reference [42] showing a detailed view of the different experimental areas and some of the different detection systems available at the NSCL.

an intermediate charge state stable primary beam that is injected into the center of the K500 cyclotron. After the K500 accelerates the beam to a moderate energy, the intermediate charge state beam is fully stripped and sent to the center of the K1200 cyclotron to accelerate the primary beam to its final energy. The primary beam is then impinged on a target foil where the primary beam reacts via fragmentation to produce a cocktail beam that contains some of the original primary beam and many different isotopes. This cocktail beam needs to be purified to select the isotope of interest for the chosen experiment. To do this, it is sent to the A1900, a dual stage fragmentation separator that allows the cocktail beam to be purified in most cases to a very pure secondary beam. At this point, the secondary rare isotope beam is sent to a specific experimental area which can include the different experimental vaults such as the N2/3 vault where the MONA LISA detection system can be set up, or the S3

vault that contains the S800 Spectrograph, or to the ReA facility where the beam can be stopped in the gas stopper and then reaccelerated to energies better suited for certain types of experiments such as reactions of astrophysical interest.

3.1.1 SuSI Ion Source

The Superconducting Source for Ions (SuSI) was used to produce the ^{48}Ca primary beam for this experiment. SuSI is an Electron Cyclotron Resonance (ECR) source that utilizes a plasma of free electrons and an ionized gas trapped in magnetic fields to generate a moderately charged ion beam that is then guided to the K500 cyclotron via electric fields. SuSI was designed with superconducting magnets, the capability to operate with two frequencies, and the ability to tune the axial magnetic field to be able to better match the acceptance of the cyclotrons than previous ECR sources that relied on room temperature magnets to achieve higher beam intensities [43].

An ECR ion source generates intermediately charged ions by removing electrons one at a time via collisions with free electrons in a plasma of ions. The plasma is contained within a magnetic field and, since it is electrically charged, the ions rotate with a frequency described in equation 3.1:

$$\omega_c = \frac{eB}{\gamma m_e} \tag{3.1}$$

where ω_c is the cyclotron frequency, e is the charge of the electron, B is the magnitude of the magnetic field and m_e is the mass of the electron. The ion source only produces a gas up to 10^{-6} Torr to reduce ion-ion collisions which impair the ion source's ability to create higher charge state beams.

SuSI has the ability to operate with two frequencies, 18+14.5 GHz [43], which allows both the axial and radial magnetic fields to be tuned to optimize the desired charge state. The intensity of the generated beam has been shown to be related to the location of the plasma electrode relative to where the plasma is trapped in the magnetic field. SuSI has a stationary electrode and a movable axial magnetic field. The axial magnetic field is controlled by two sets of solenoid magnets on each end of the device, one set of two on the injection side and the other set of two at the extraction side.

3.1.2 Coupled Cyclotrons

A cyclotron accelerates ions in a spiral motion by using a magnetic field that is perpendicular to the plane of the ion's motion. This spiral motion allows the ions to be accelerated many times inside of the cyclotron from the center of the device across the electrodes, called "dees," with an electrical charge that produces an electric field that is then rapidly cycled using radio frequency allowing the ions to continually be accelerated across the gap between the dees. This principle works because as the ions increase their velocities, the circular path they follow gradually increases and the time spent traveling along the dees is the same for all passes after each acceleration. After the ions reach the maximum radius, they are extracted from the cyclotron.

The Coupled Cyclotron Facility uses two cyclotrons in series to enable maximum primary beam energies of 200 MeV/nucleon for light nuclei and on the order of 100 MeV/nucleon for higher mass regions. The K500 cyclotron accepts the intermediate charge state ions from the ion source and accelerates these ions to around 15-20 MeV per nucleon [40]. They are then stripped of electrons to reach their highest charge state and sent to the center of the K1200 to be accelerated to their final primary beam energy.

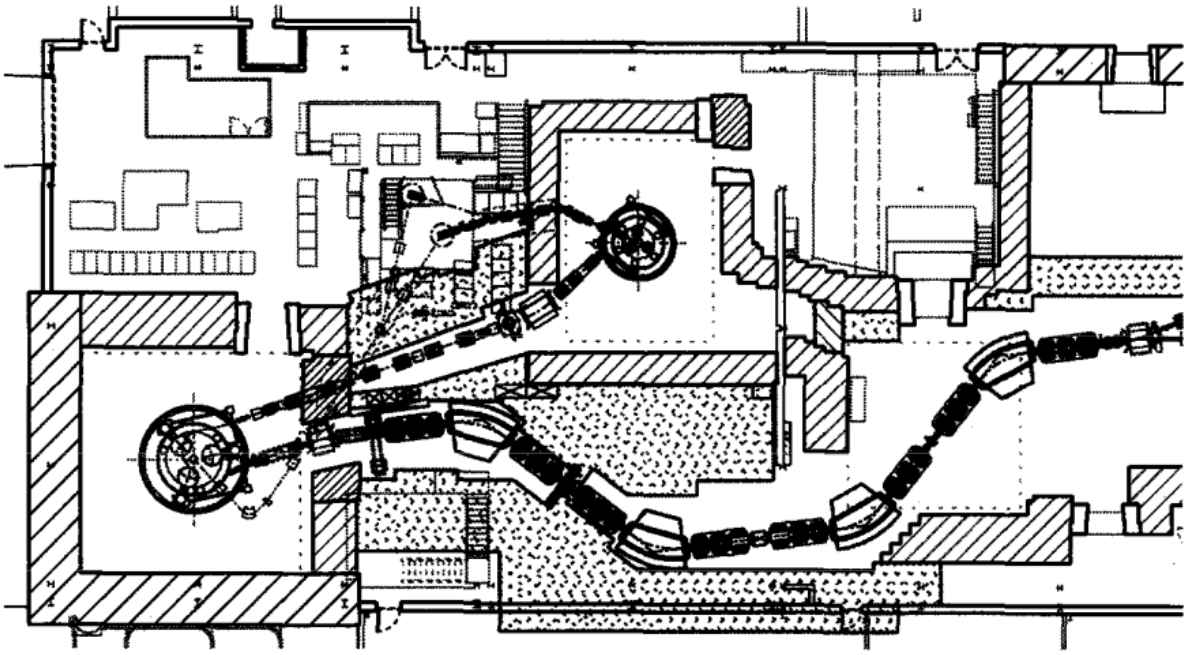

Figure 3.2: The above figure depicts a schematic looking down into the NSCL of the configuration of the ion source leading into the K500 and then the K1200 cyclotrons and then into A1900 fragment separator. Taken from Reference [40].

3.1.3 A1900 Fragment Separator

After the primary beam leaves the K1200 cyclotron, it is reacted on a ^{9}Be production target to produce a cocktail beam that then requires purification. The A1900 Fragment Separator uses two stages made up of 24 quadrupole magnets and four 45 degree dipole magnets to purify this cocktail beam to produce a secondary beam [44]. It does this by using dipole magnets with a bending power greater than the cyclotrons and a relatively large acceptance to be able to accept most of the secondary reaction products. The cocktail beam coming from the production target contains the unreacted primary beam and fragmentation reaction products and is sent to the first stage of the separator.

The first half of the A1900 is used to select a set of ions with the same magnetic rigidity.

Magnetic rigidity is defined in Equation 3.2.

$$B\rho = \frac{\gamma m v}{q} \tag{3.2}$$

where B is the magnetic field, ρ is the radius of the circular path the ions take, γ is the Lorentz factor, m the mass of the ion, v is the velocity and q is the charge of the ion. Since every ion is moving with roughly the same velocity after fragmentation, when the cocktail beam travels through a magnetic field produced by a dipole magnet, ions with different mass vs charge ratios, also known as the A/Q ratios, bend with different radii. Isotopes with a specifically chosen ratio can then be allowed to progress down the beam line using apertures. The beam then consists of many nuclei with the same A/Q ratio. The beam then travels to the wedge in the center of the A1900.

The degrading wedge is made of two separate aluminium pieces that can be rotated to create wedges with many different thickness to be able to efficiently separate the wide varieties of beams available at the NSCL. To select a single isotope, the beam needs to be separated by element. Energy loss through a target is proportional to the Z^2 of each ion. When the beam is passed through the wedge, heavier elements will lose the most energy and be traveling slower than lighter elements. This allows a second dispersive section of beam line to then select a more specific range of secondary reaction products to produce the final secondary beam.

The degrading wedge is located at image 2, which is between the first two dipoles (D1 and D2) and the second two dipoles (D3 and D4). The final stage of the A1900 uses two more dipoles to bend the beam again to select, in most cases, a very pure secondary beam. This stage uses two dipole magnets to again bend the beam. Since the ions have the same

A/Q ratio, but different velocities for each element, the heavier elements will be bent the most and the lighter elements the least. A final set of apertures can be used to select the now purified secondary beam to be sent to the experimental area.

3.1.4 GRETINA

The Gamma-Ray Energy Tracking In-beam Nuclear Array (GRETINA) is a semiconductor based gamma ray detector utilizing electrically segmented High Purity Germanium (HPGe) crystals. GRETINA was originally made up of seven detector modules with additional modules to be added. For the experiment described in this thesis, nine modules were used [32, 45, 46]. This array covers over 1 pi solid angle allowing this detector to reconstruct both the energy and location of gamma ray events in the detectors with high levels of precision and with great efficiency. GRETINA is the beginning of GRETA [47, 48] which will be complete when the array consists of 30 germanium detector modules and will have solid angle coverage of almost 4 pi.

Each detector module houses four tapered cylindrical germanium crystals that have hexagonal faces. The geometry of the hexagonal crystals were chosen to optimize the spherical coverage based on the mathematical approximations of the geodesic dome where a certain number of hexagons and twelve pentagons can approximate a sphere. GRETINA uses the 120 hexagon approximation with sixty hexagons each of two different shapes. Each detector module uses two of each kind of hexagonal crystals, A and B as shown in figure 3.3. The crystals are contained in aluminum housings that link them with Field-Effect Transistors (FETs), preamplifiers and a cryostat for maintaining the cryogenic temperatures required for the HPGe crystals.

A solid aluminium support frame holds the GRETINA detector modules and allows for

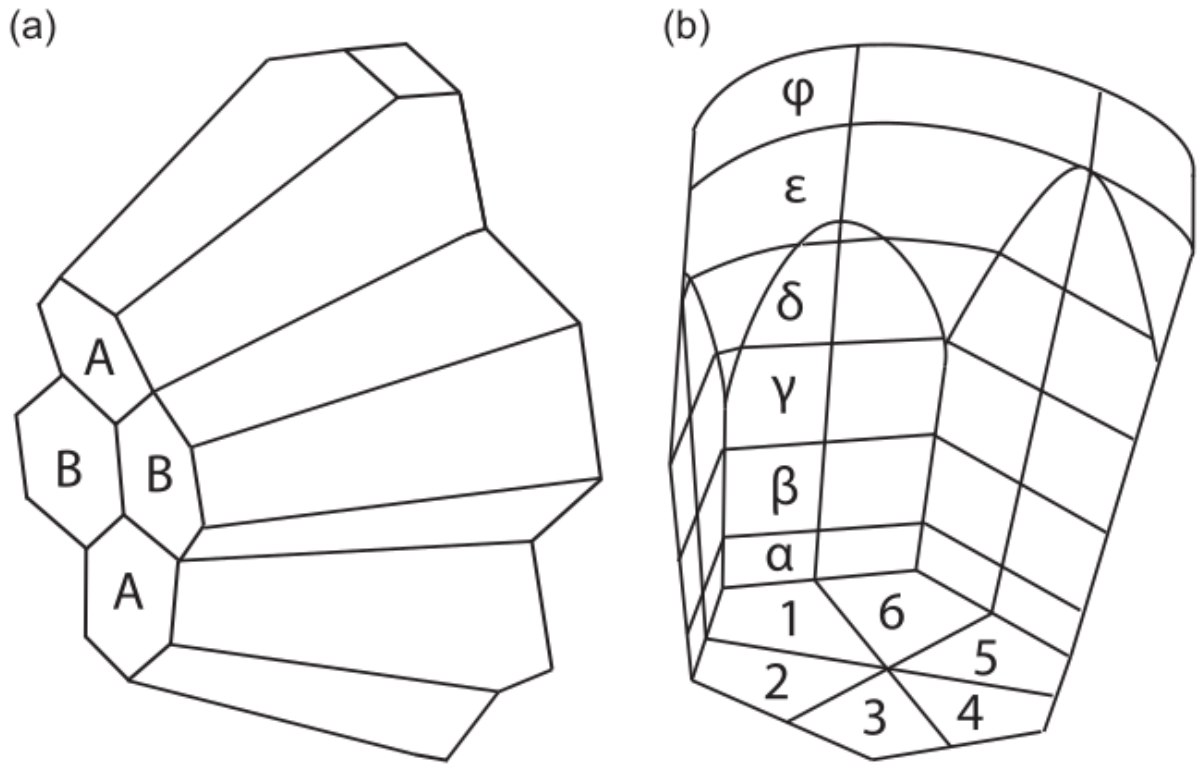

Figure 3.3: Figure (a) shows the geometry of the crystals in each detector module with both types of hexagons labeled A and B. Figure (b) shows the segmentation of each hexagonal germanium crystal. This figure was taken from Reference [49].

consistent positioning of the detector modules around the beam pipe holding the experimental target [32]. The frame consists of two hemispheres resting on a cart that allows for each hemisphere to be moved independently. The support frame allows the detectors to be positioned in rings around the beam pipe at 58, 90, 122, and 148 degrees with eight detector positions in the 90 degree ring, four in the 58 degree ring and five each in the other rings. This spacing allows for the frame to be situated in the experimental target area of the S800 Spectograph.

Each GRETINA crystal has 36 segments and a central core for a total of 37 electrical readouts from each crystal. The central core gives the best energy resolution of the gamma ray interaction. The high segmentation of each crystal allows for an algorithm using the signal decomposition to be used to achieve sub segment position resolution. The signal decomposition analyzes the waveform signals coming from each segment [49]. Multiple gamma ray interactions can occur in each recorded event. These events can be located in the same crystal or potentially in the same segment. The signal decomposition works to untangle these events by utilizing the image charges a gamma ray interaction causes in neighboring crystals. These digitized waveforms can then be compared to known examples of gamma ray interactions that occur at various points within the different crystals to pinpoint where the experimental gamma ray interacted inside the crystal. This process allows for the 2mm position resolution achievable using GRETINA.

The process can be taken one step further to link interaction events in order to track how a gamma ray interacts in the crystals and to determine the trajectory it takes within the GRETINA array. The process starts by grouping events likely to have occurred from a single gamma ray based on criteria such as angular separation. Then these events are sorted based on a figure of merit that is calculated based on the probability of possible

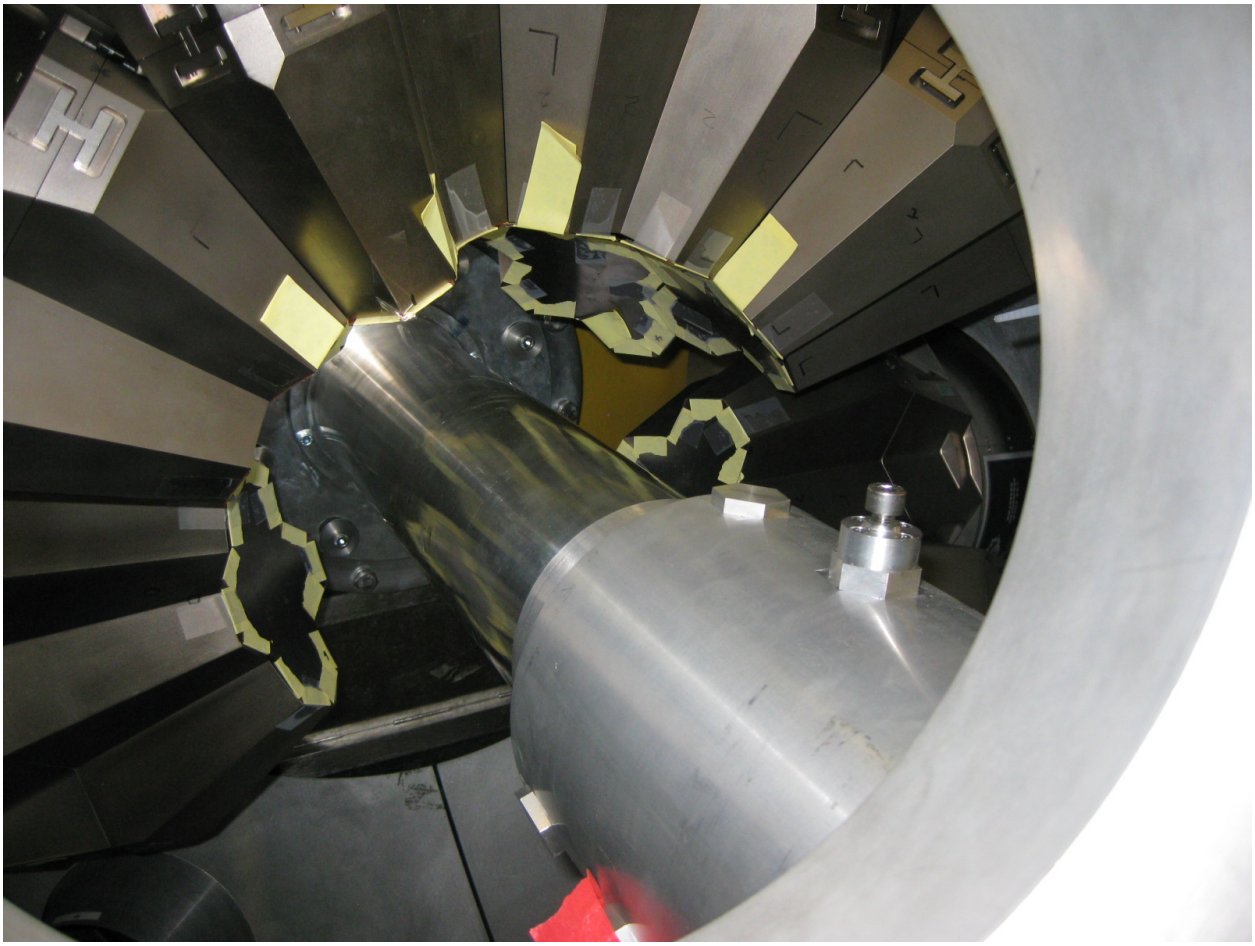

Figure 3.4: A photo of the configuration of the nine GRETINA modules for the experiment. The GRETINA crystals are surrounding the beam pipe TRIPLEX plunger device which is mounted in the beam pipe attached to the entrance of the S800 Spectrograph.

arrangements of the sequence of theses events. The figure of merit would ideally be zero for a fully absorbed gamma ray interaction. There would be non-zero figure of merits for other kinds of interactions. In principle, after tracking based on these figure of merits, the peak to total count ratio could be maximized. However, since the energy resolution and the position resolution are not exact, some events have similar figure of merits to true photopeak interactions. Since this reduces the relative tracking efficiency, tracking was not utilized for this experiment.

3.1.4.1 Addback Method

A method to reconstruct Compton scattered gamma ray events was introduced in this data analysis. This method, known as the Addback Method, was developed in References [50,51]. The greatest energy hit in a multiple gamma ray event is taken as the original hit position. If lesser energy events were found in the Addback radius, which is defined as 7.5 cm for this data set, they are added to the greatest energy hit to create a full photopeak event. This helps reduce the number of Compton scattering events in the gamma ray spectra to increase the peak to total ratio and recapture more true events lost in the background. This method was used because the transitions of interest were around 1 MeV where Compton scattering events are a significant contribution to the background events.

3.1.5 S800 Spectrograph

The S800 Spectrograph is a single detection system that combines the ability to have a high beam acceptance with high resolution particle identification [52]. The system is made up of two main components, the analysis line and the high acceptance spectrograph. The analysis section comes before the experimental target area and contains the tracking detectors that allow for reconstruction of the particles' trajectories. The spectrograph comes immediately after the target area and at the end of the spectrograph is its focal plane.

The spectrograph is unusually built with the dispersive plane in a vertical plane. This device spans three stories and weighs around 250 tons. The spectrograph covers a solid angle of 20 msr and has a momentum acceptance of 5 percent. The analysis line has a maximum rigidity of 4.5Tm to be able to separate the reaction products from the secondary beam in order to reduce the beam intensity in the focal plane.

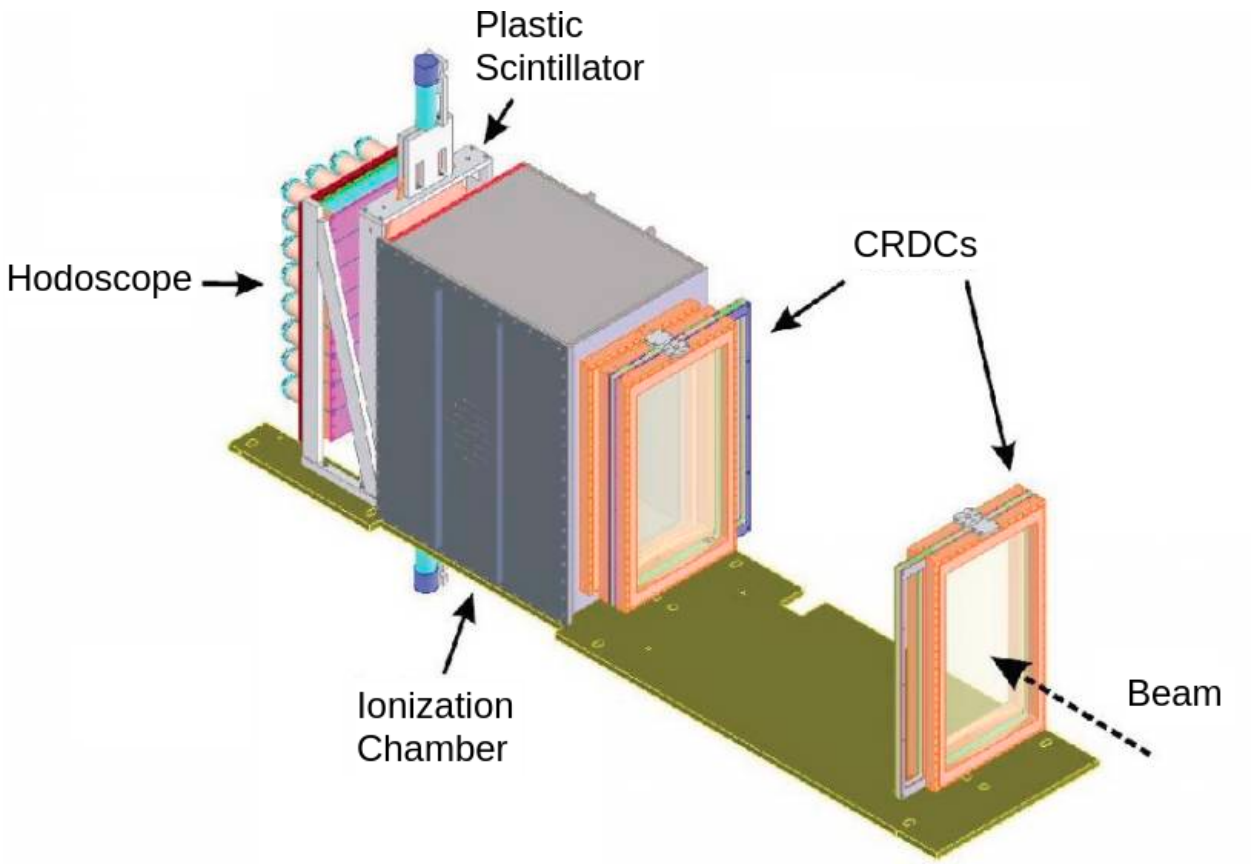

Figure 3.5: A schematic of the S800 Spectrograph focal plane. This highlights the various detectors including the Cathode Ray Drift Chambers (CRDCs), the ion chamber, the plastic scintilators, and the hodoscope.

3.1.5.1 The Focal Plane

The focal plane is a collection of detectors that contain two Cathode Readout Drift Chambers (CRDCs), a sixteen fold segmented ion chamber, four plastic scintillators ranging from 3 to 20mm thick and ends with a hodoscope used for identifying isomeric states. All detectors in the focal plane have an active area of 30cm x 59cm.

The CRDCs are separated by about one meter to provide both position and angular information on the ions that pass through them. Both CRDCs have 224 channels allowing for position resolution of about 0.5mm in both the x and y directions. The incoming particles are dispersed along the 59cm direction of the CRDCs. The CRDCs work on the same principle

as a single wire drift detector, but the position along the wire is obtained by induced cathode readout. The charge induced in each pad is read out and then fit using a Gaussian curve. The centroid of the Gaussian gives the position of interaction.

After the x and y position is determined in the CRDCs, the beam passes through the ion chamber. The ion chamber is Frisch gridded with 16 one inch wide anodes that are positioned perpendicular to the beam. The energy loss is sampled along the path of the ions through the ion chamber. The first plastic scintilator acts as the exit window of the ion chamber. This reduces the energy straggling normally associated with an exit window. Three further plastic scintilators measure total energy loss and timing information.

3.1.5.2 The Analysis Line

The tracking detectors determine the incoming positions and angles of the secondary beam before it reaches the experimental target area. These detectors are located between the two bends of the analysis line so any particles that react inside the detectors are deflected from the target area and do not affect the quality of the data collected. This technique allows for higher maximum beam rates. The detectors in the analysis line section of the S800 have not been used in recent experiments.

The set of detectors in the S800 allows for data on the particles to be reconstructed through the beam line using COSY transfer maps that are able to be created before the experiment. With the information from the map and the analysis beam line, the initial position and trajectory at the target location can be known for each particle.

3.1.6 TRIple PLunger for EXotic Beams

The TRIple Plunger for EXotic (TRIPLEX) Beams [53] is a device that can be used to measure the lifetimes of short lived excited states in exotic nuclei while in-flight. This kind of device [54–56] opens the possibility of directly measuring short lived states that can only be measured at facilities like the NSCL. The TRIPLEX is a plunger style device that uses multiple foils held in the beam line to perform Recoil Distance Measurements (RDM) and Differential Recoil Distance Measurements (DRDM) in conjunction with a gamma ray detection array such as the Segmented Germanium Array (SeGA) [57] or GRETINA [32]. There are three main components of the TRIPLEX plunger consisting of the support structure, the bearing unit and the foil unit.

The support structure can be seen in Figure 3.6, specifically part (A) which is the outer casing designed to hold the whole structure of the plunger device. The beam pipe has a diameter of six inches and has a flange to securely couple the beam pipe to the S800 Spectrometer but allows the main portion of the TRIPLEX plunger beam pipe to be precisely aligned with the S800 Spectrograph. The beam pipe has six alignment screws to align the plunger device within the pipe itself. This is necessary as beam spots of rare isotope beams can be as wide as a centimeter. Another portion of the support structure is the electrical feedthrough. This feedthrough allows the electrical connections necessary for the motors that drive the foil and the connections on the foils for distance measuring to be passed outside of the vacuum chamber. The inner structure consists of an outer support frame attached to an inner ring that supports all of the immobile parts, such as the two motors, the middle tube and the connectors.

Three stainless steel tubes separated by four sliding bearings make the bearing structure.

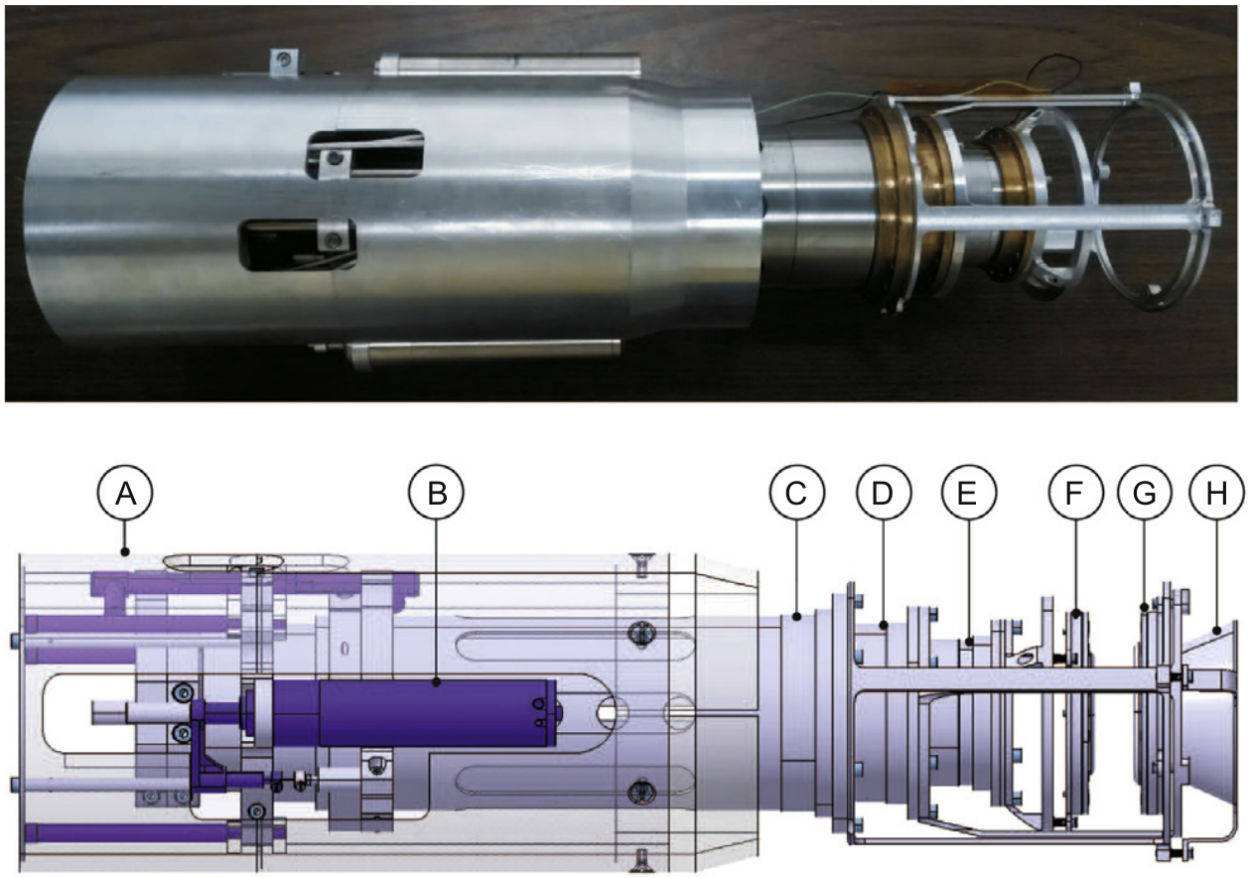

Figure 3.6: A photo of the TRIPLEX plunger along with a labeled schematic. (A) is the outer casing, (B) is showing one of the piezeoelectric motors, (C) is the outermost support ring for the second degrader, (D) is the stationary middle ring holding the first degrader, (E) is the inner ring that supports the target foil, (F) (G) and (H) are the locations of the target foil, first degrader, second degrader and their holding cones, respectively. The figure is taken from Reference [53].

The middle tube, which supports the first degrader, is in a fixed position. The bearings then support, separate, and hold the outer and inner tubes in alignment with the middle tube. This unit is critical for the functioning of the plunger device as the technique relies on the ability to precisely control the distance between the foils. The two motors are directly connected to the inner and outer tubes. Great care has been taken to insure that there are no forces opposing the motion of the tubes to avoid damaging or deforming the tubes.

A brass ring has been added to the end of each of the three tubes mentioned above, in order to attach the aluminum structures that hold the foils. One end of each foil unit is attached to a brass ring, and the other end allows for the cones that hold the foils to be attached with three screws. The cones are electrically isolated from the foil units to allow for the capacitance between the foils to be measured as a way of determining the distance setting. Due to the relatively large beam spots and the fact that the beam must pass through the length of the device, the dimensions of the foils are approximately 5cm $\times$ 5cm. Three unique styles of cones were designed, one for each ring of the device. The target and first degrader cones are connected in a way such that the foils face each other. To be able to achieve contact between the first and second degraders, the second degrader foil and cone are designed so that they can nest inside of the first degrader foil's cone.

The various components of the TRIPLEX plunger are controlled with modified software based on the software designed for the first plunger device made at the University of Cologne, Germany. A standard plunger has only two foils. Since the TRIPLEX can be thought of as two standard plungers combined into one device, the software was designed to be modular so each half has independent controls. The software controls the active components of the motors and the passive components such as the various distance measurement devices.

There are two motors located on either side of the device. One drives the target foil ring

and the other the second degrader foil ring. The motors are based on piezeoelectric technology that allows for accurate and reproducible small scale movements of the inner and outer foil rings. Knowing the relative distance between the foils with high accuracy is a key component in the analysis of the data collected in experiments using the TRIPLEX device. The linear actuator and the micrometer probe manufactured by the TESA group work together to determine the relative distance between the foils and gives real time measurements that assist in the driving of the foils during calibrations or experiments. All of the information given by these detectors is passed to the software system that is used to control the motors.

Usage of the software consists of controlling the graphical user interface (GUI) that comes with the software. One portion of the GUI controls the speed at which the chosen motor will drive the associated foil. The speed is chosen on a dial from 0-7. Where 0 corresponds to no movement and 7 being the fastest speed. Another part of the controls allows the motors to be turned on and off. While the motors are active, other parts of the GUI respond with information about the change in distance using information from the linear encoder at all distances and from the TESA micrometer when the distance between the foils is less than 1.0 mm. This allows the user to safely drive the foils within the device and to chose a precise location to where the foils will be moved.

This device allows for the Recoil Distance Method to be used to analyze gamma ray transitions of excited states in rare isotopes. This method is a modified version of in-beam gamma ray spectroscopy where instead of having only a target foil for the secondary beam to react upon, there is the ability to add one or two degrader foils which serve the purpose of slowing down the reaction products as the beam passes through. This creates distinct sections of differing velocities in which the reacted nucleus can deexcite. After applying a Doppler shift correction, these different sections cause each transition to make multipeak

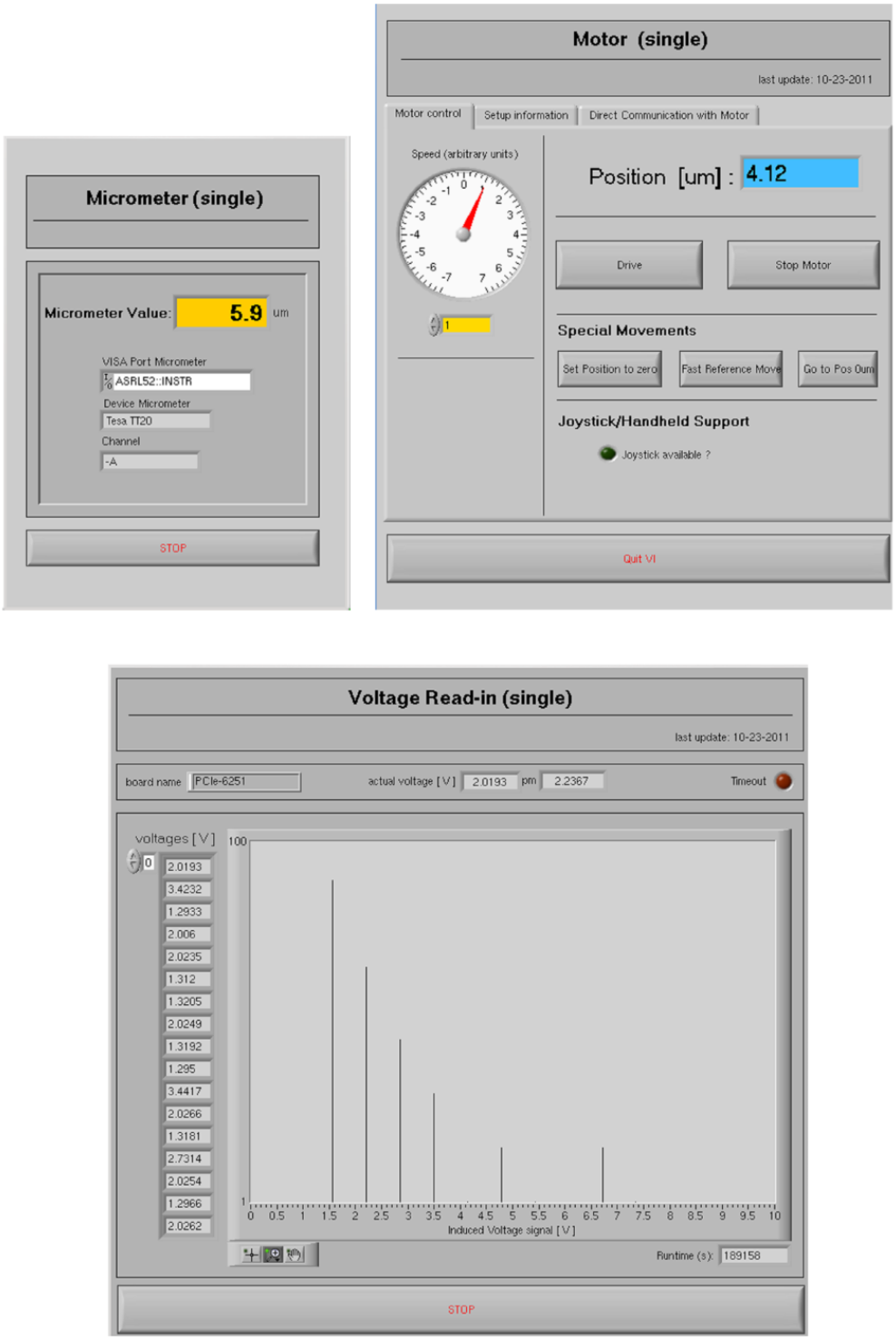

Figure 3.7: An example of parts of the GUI for controlling the TRIPLEX motors and measurement tools. The figure is taken from Reference [53].

structures instead of only a single peak as is seen in standard beam gamma ray spectroscopy.

3.1.7 Experimental Setup

The experiment detailed in this dissertation used the TRIPLEX plunger device set up in the experimental area of the S800 spectrograph beam line along with GRETINA. The data set taken in the present experiment is summarized in table 3.1. The TRIPLEX was configured with up to three foils, a target foil of 2mm thick Beryllium, a first degrader foil of 0.58mm thick Tantalum, and a second degrader of 0.25mm thick Tantalum. One primary beam, of ^{48}Ca, was generated for this experiment at 140 MeV/u. From this primary beam two secondary beams were generated, one of ^{44}Cl and another of ^{45}Cl. Target only data was taken with the ^{44}Cl beam at an energy of 99 MeV/u. Shortly after the target only data was completed, the secondary beam was lost due to failure of beam-line components and had to be recreated. After this, the energy was then 89 MeV/u for all other times the ^{44}Cl beam was used.

Three plunger distance settings, where the distances were sensitive to lifetimes around 1-20ps, were taken with the target and first degrader using the ^{44}Cl beam. These settings were with the following distances between the target and first degrader foils as measured from nearest faces of the foils, 0mm, 0.5mm, and 1mm. A single long distance data set, with the foils separated by 22mm, was also taken with this beam to constrain reactions generated in the degrader foil.

With the ^{45}Cl beam, only two distance settings were taken. One setting with 1mm between the target and first degrader and 10mm between the first and second degraders was taken for sensitivity to a larger range of lifetime, between 1-100ps. A long distance setting, with 25mm between all foils, was taken to constrain the ^{45}Cl reactions with the two

Beam		**Distance Setting**		
Primary	Secondary	Target Only	Two Foil	Three Foil
140 MeV/u ^{48}Ca	102 MeV/u ^{45}Cl	yes	—	1mm, 10mm 25mm, 25mm
	99 MeV/u ^{44}Cl	yes	—	—
	89 MeV/u ^{44}Cl	—	0mm 0.5mm 1mm 22mm	—

Table 3.1: This table summarizes the information on which distance settings of the TRIPLEX plunger device were used for each secondary beam produced from the primary beam. The primary beam was used to produce all secondary beams. The distance setting labeled "Target Only" denotes when there was data taken with only the target foil installed in the TRIPLEX for that beam setting. The distance setting for two foil data is the distance between the target and first degrader. For the three foil column, the first number indicates the distance between the target and the first degrader and the second number indicates the distance between the first and second degrader foils.

Tantalum degraders.

3.1.8 Calibration Procedure

Data files from the experiment were converted from the highly compressed format they were saved into and calibrated using GrRoot, a program based on CERN's ROOT [58]. The calibration process involved three main steps: 1) convert the raw data in its hexadecimal form and converting into a ROOT decimal format, 2) then calibrate and sort the information into ROOT trees, 3) convert this information into histograms using a separate script. The sorting step creates ROOT trees, a data type that is made of organized lists of correlated information for each event. Histograms make it easier to interpret the information and allows for visual gates to be made for selecting data of interest. The calibration and histogram

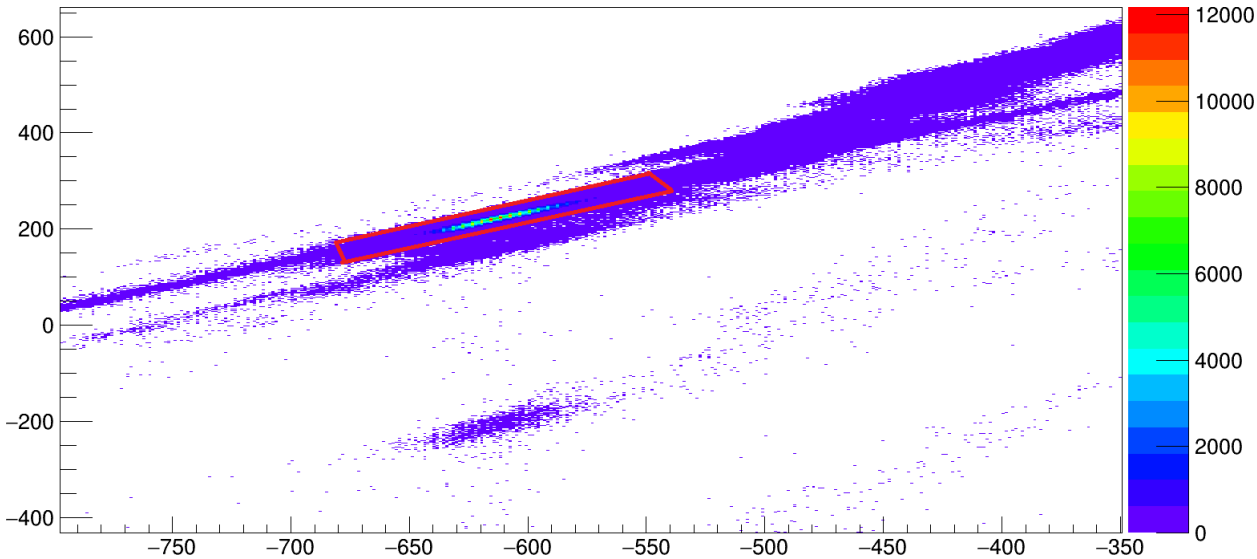

Figure 3.8: A plot showing the spectra of the incoming beam. From this plot an incoming beam gate is made to begin the calibration and particle identification. An example beam gate is shown in red for ^{44}Cl.

generating steps are completed multiple times as information is gathered throughout the calibration process and calibration parameters are determined.

The E1 Timing Scintillator measures the Time of Flight of the various particles that are traveling through the S800 Spectrograph. The time the ions take to travel through the S800 is a critical component in most of the latter calibrations that are used to clearly identify the nucleus in the S800. Time of flight information was modified to correct for the different paths the ions take through the S800. The ion's trajectory through the Spectrograph can be generally described by the uniform circular motion equation:

$$\frac{F}{m} = \frac{v^2}{r} \tag{3.3}$$

where, F, the force causing the motion from the dipole magnets, is:

$$F = Bqv \tag{3.4}$$

and m is the mass, v is the velocity of the ion, r is the radius of motion, and q is the charge of the particle. This leads to the relation between the mass to charge ratio and the TOF through the S800 Spectrograph as given in the derivation below. Note that in this case the mass of the ion m is also known as A, the number of nucleons and that r is also often referred to as ρ when the radial motion relates to magnetic fields. So the A/q ratio can be written as follows:

$$\frac{A}{q} = \frac{B\rho}{v} = B\rho\frac{t}{d} \tag{3.5}$$

where d is the distance traveled and t is the TOF. Generally, the quantity $\frac{B\rho}{d}$ is taken as a constant so the TOF is directly related to the mass to charge ratio. When the TOF corrections are applied, the Particle Identification (PID) becomes much clearer, with the different A/q ratios well defined and separated.

The TOF is also dependent on the distance traveled through the S800. In the first order, all ions travel roughly the same distance. However, the x position (XFP) and the angle (AFP) measured at the S800 focal plane can significantly effect the TOF. Therefore TOF corrections need to be applied to both the XFP and AFP. As seen in figure 3.9, before correction, while the different isotopes are somewhat defined, after corrections the plots are much more correlated and the different isotopes are more separated.

After creating an incoming beam gate and various outgoing particle gates, calibrations can be performed on some of the detectors mentioned above. The first step is to calibrate the Ion Chamber. After selecting an outgoing particle beam that covers the width of the chamber, the outputs from each of the sixteen segments need to be gain matched. This allows for an even response across the chamber so only one set of parameters are required to calibrate the detector. The calibration allows for an accurate measurement of the energy loss through

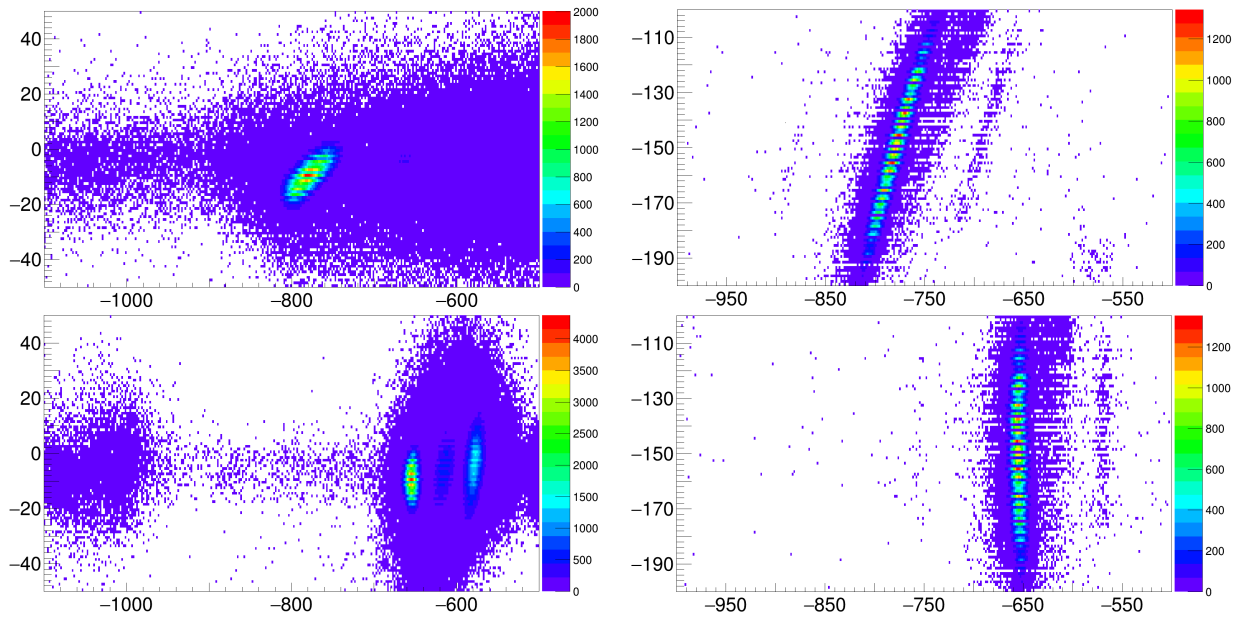

Figure 3.9: Plots showing the effects of the Timing Scintillator calibrations. The top row is before calibration and the bottom row is after calibration. The left column is the calibration for the AFP, angle at the focal plane, variable. The right column is the calibration for the AFP, x position at the focal plane, variable. The horizontal axis is the measured Time of Flight and the vertical axis is the AFP or XFP measurement respectively. After a proper calibration, the intense blobs will be shifted from a tilted position to being vertical.

the detector which is related to the Z number of the ion allowing elemental resolution. A proper calibration will take information from each of the sections of the ion chamber, which before calibration were not aligned horizontally, and align them so each section of the ion chamber has the same magnitude of response for the same kind of incoming particle.

Figure 3.10 shows the uncalibrated ion chamber in the top portion of the figure and the calibrated ion chamber in the bottom portion. After gain matching the Ion Chamber, the x position information from the ion chamber is then calibrated. Energy loss through the ion chamber is mostly dependent on the Z number of the ion, but the path length through the detector is another important factor. Since the dispersive plane lies in the x direction, the critical parameter to calibrate is Xfp. Before correction, the energy loss as a function of xfp has a distinct slope greater than one. After applying the correction, the line should turn horizontal, indicating that there is now no dependence in the measured energy loss due to the x position at which the ion enters the chamber. This correction helps the elemental separation in the final particle identification plot.

Both CRDCs must also be calibrated. A beam gate is chosen such that there is a significant response across the majority of the 224 pads, and then the electrical responses are gain matched in a similar process to the ion chamber. Figure 3.11 shows the uncalibrated CRDC in the top portion of the figure and the calibrated CRDC after calibrating the gain. Before the gain matching, the various 224 pads show a jagged response to a single type of incoming particle. After the response is fully gain matched using an iterative process, the detector response is much more cohesive. Once the gain matching has been completed, the x and y positions of the particles moving through the CRDCs must be calibrated.

To fully calibrate the x and y positions in the CRDCs, special calibration plates with small precise holes called Mask Plates are inserted into the beam in front of one of the

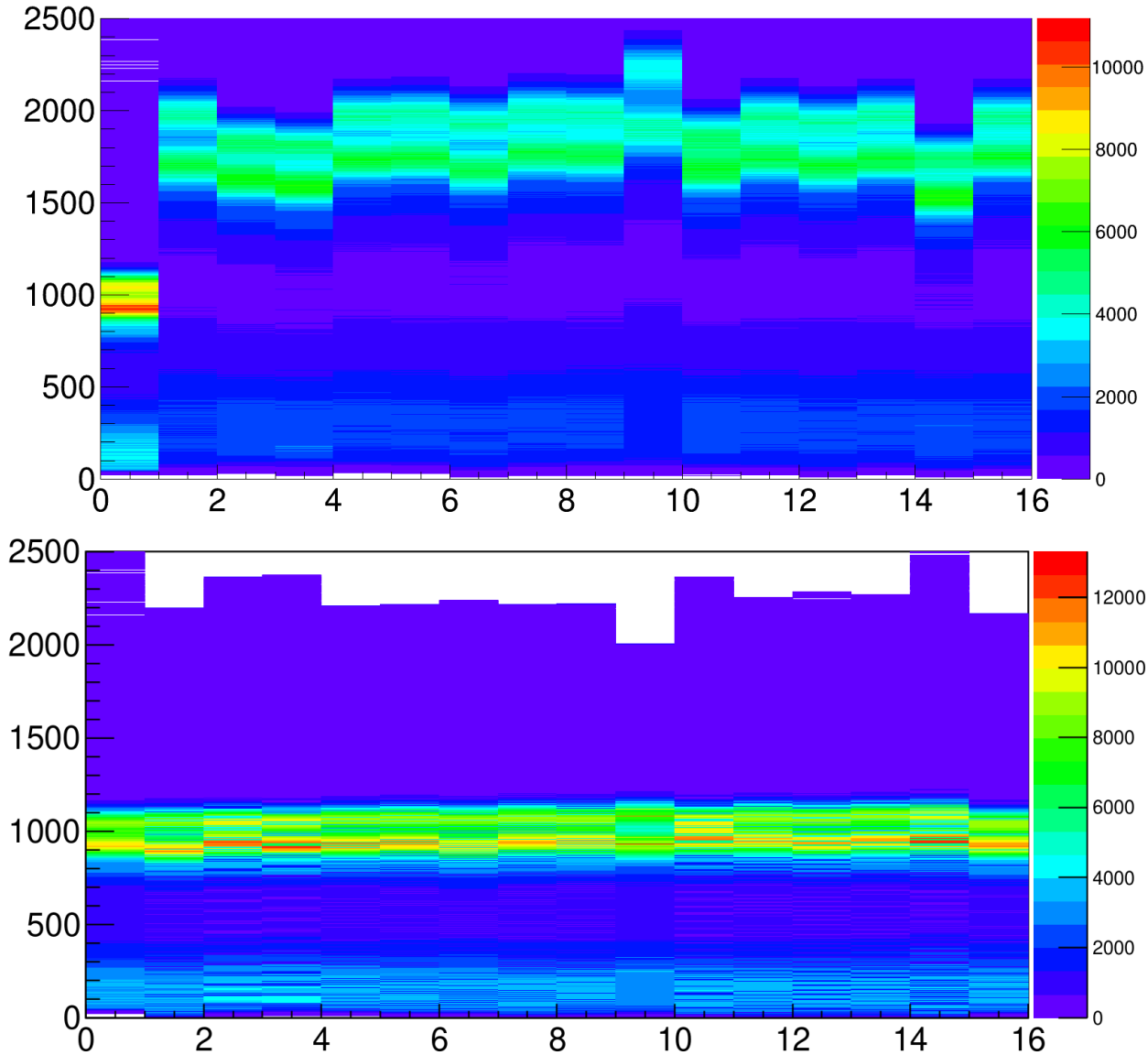

Figure 3.10: Plots showing the effects of the Ion chamber gain calibrations. The top figure is before calibration and the bottom figure is after calibration. The horizontal axis is the ion chamber channel number and the vertical axis is the response measured in each section. Before the gain matching, each pad has a similar response. After the calibration, the measured response becomes more cohesive across the ionization chamber.

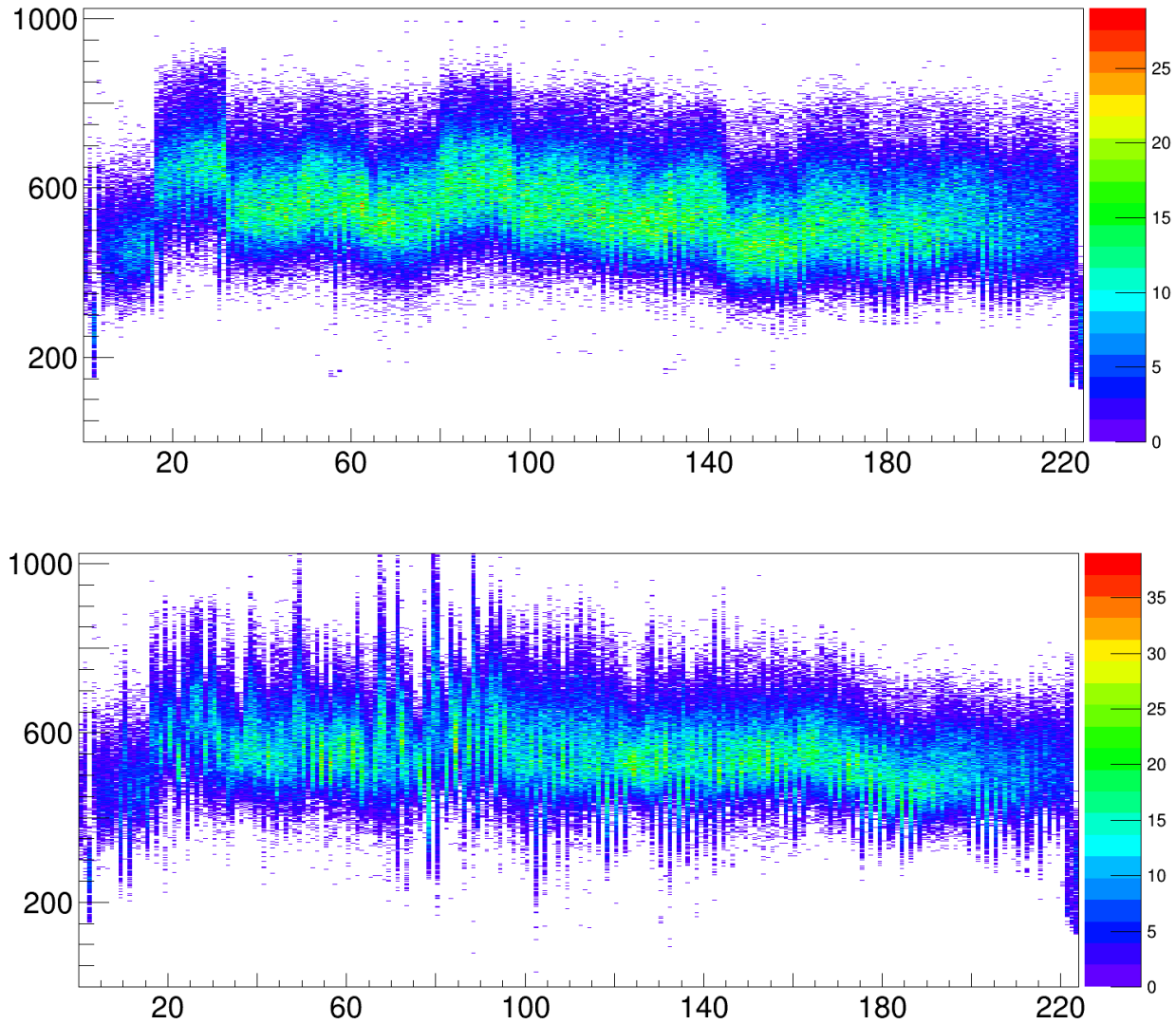

Figure 3.11: Plots showing the effects of the CRDC gain calibrations. The top figure is before calibration and the bottom figure is after calibration. The horizontal axis is the CRDC pad number and the vertical axis is the response measured in each section. Before the gain matching, response varied strongly by pad. After the calibration, the measured response becomes more consistent across the CRDC.

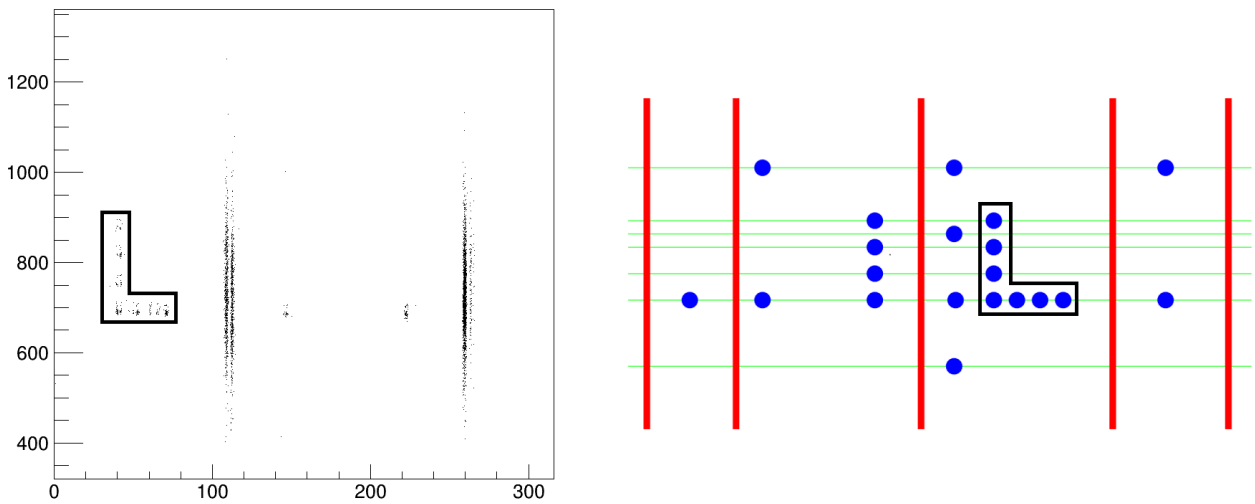

Figure 3.12: The left figure shows an example of what a mask run data set looks like. The right shows a Reference schematic of the mask plate. A key feature to note is the "L" shaped sequence of dots that allows for the orientation of the plate to be determined. Data is taken in the CRDC just long enough for the positions of the mask holes to become clear enough to calibrate the y positions in the CRDC.

CRDCs. There is a unique arrangement of the holes for each CRDC detector. The plate stops the beam from entering the detectors except for in the areas corresponding the precise holes. Matching the detectors response to the well known position of the holes in the mask allows for an accurate x and y position calibration. Figure 3.12 shows a diagram of the mask plate and an example of the data from a CRDC during the mask calibration run.

Once all of the main detector elements of the S800 spectrograph are calibrated, the proper COSY inverse map file must be added into the settings information file. These inverse maps allow for detailed information to be calculated about an ion's path throughout the Spectrograph. GrROOT takes the information from the map along with information from each of the detectors in the S800 to produce the best particle identification plot. One of the biggest advantages in using the S800 spectrograph is the very clear particle identification that can be used even for relatively heavy ions around Z=50. In figure 3.14 the PID for the target only data set is shown. The various blobs correspond to one isotope each. Each blob

is clearly separated and can be used to draw clean gates for data analysis of the gamma rays measured by GRETINA.

Additionally, the arrangement of the GRETINA modules must be noted in the settings file. This provides information on the number of modules and positions of each germanium crystal within the array and a derivation of the angle of the gamma rays when they interact with GRETINA. The angular information is critical for proper Doppler shift correction in the analysis.

There are several parameters that are associated with the ion detection by the S800 that vary slightly through time due to changes such as temperature or the pressure of gas in the detectors. This causes the Gaussian distribution center to vary slightly from 0. It is possible to make one overall parameter set where the distribution is centered around zero, but this is usually best for short data sets of a few runs close in time to prevent unnecessary broadening of the gamma ray photopeaks. Therefore, for most distance setting data sets, there are run-by-run corrections that are applied to each run. The parameters of interest are the y position of the ion at the focal plane (Yfp), the y position at the target (Yta), the angle of the ion's trajectory in the x direction at the target (Ata), and the angle in the y direction at the target (Bta). These parameters have some dependence on one another and must be corrected in a sequential manner starting with Yfp, and then continuing in order with Ata, Yta and finally Bta. Figure 3.13 shows the parameters after the corrections.

After all parts of the calibration process are complete, the final PID plot can be made. The S800 allows for most PID's where Z<50 to be very clear and for clean cuts to be made. Figure 3.14 is a PID plot of an incoming ^{44}Cl beam. The outgoing particles, seen in the various blobs of differing intensities, are well separated. Each roughly horizontal line corresponds to a particular element, while the vertical structures correspond to similar A/q

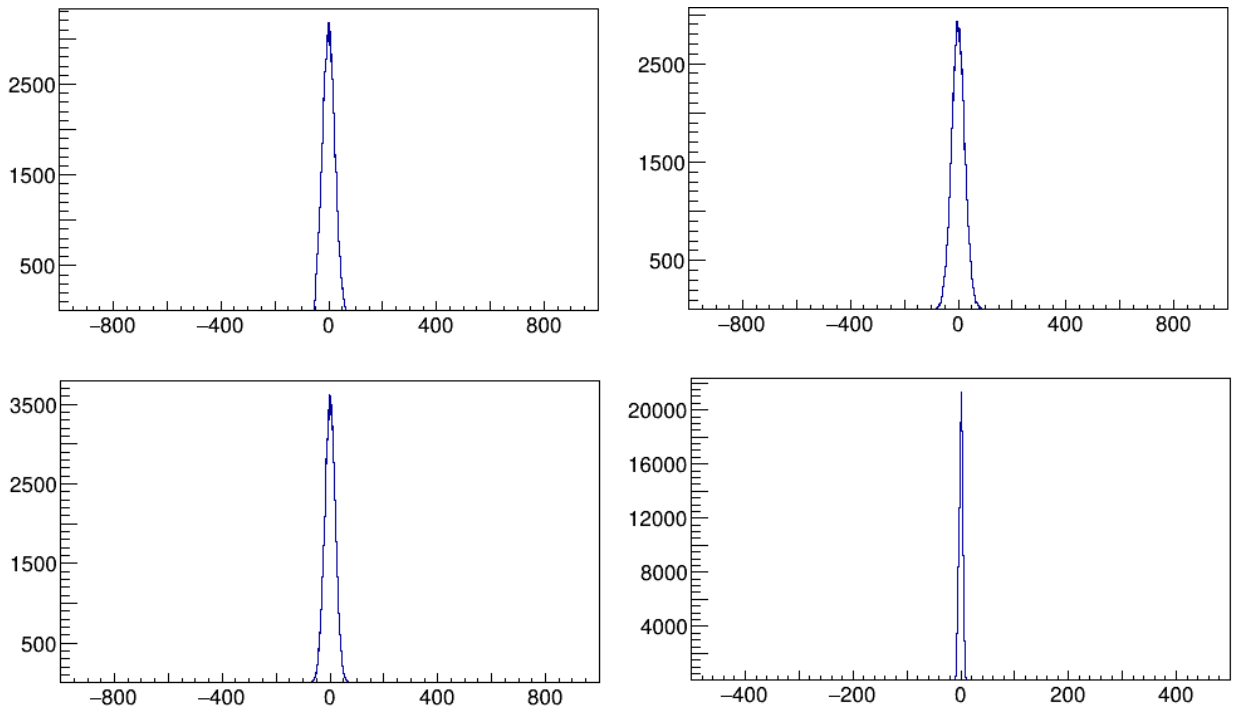

Figure 3.13: An example of a fully run-by-run corrected data set. The top row shows the distributions of the Ata variable on the left and the bta parameter on the right. The bottom row shows the Yfp parameter on the left and the Yta parameter on the right. All distributions are centered around zero to give the sharpest PID plot.

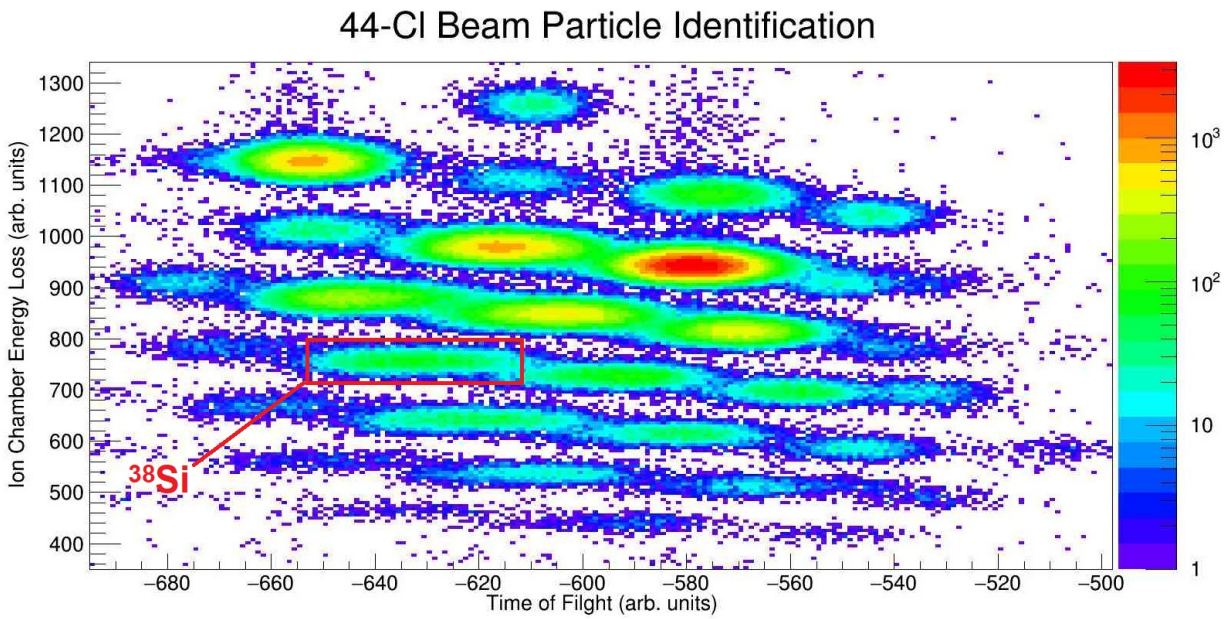

Figure 3.14: A particle identification plot from the ^{44}Cl secondary beam, target only data set. The vertical axis is the energy loss through the ion chamber and the horizontal axis is the time of flight. Each blob is a different nuclei that has been determined through the calibration process. The blob corresponding to ^{38}Si is centered around (-630, 750).

ratios.

3.1.9 G4Lifetime Simulations

One tool used to understand the many variables in the data sets is a simulation program called G4Lifetime [59, 60] that uses the GEANT4 toolkit [61] to reproduce the interactions of gamma rays in matter. These simulations allow comparison of how different lifetimes of excited states will effect the expected gamma ray spectra. To do this most accurately, the simulation must be carefully prepared with a detailed experimental geometry and a detailed parameter set. If the geometry is too oversimplified, effects such as Compton scattering and back scattering are reduced in the simulation output as there is less material in the simulation for the gamma rays to interact with. Of course, some simplification of the geometry is made

due to time limitations. Figure 3.15 shows an example of the simulated GRETINA detector module geometry along with the foil arrangement. Left out of this rendering of the simulation geometry is the shell that holds the GRETINA modules and the beam pipe to be able to more clearly show some of the internal structures of the experiment. These missing features are included in the simulation. The figure shows a view looking along the beam axis from the entrance of the S800 spectrograph showing the target foil in the red square, the two different GRETINA crystals in green and silver, and the detector cryostats in gray.

3.1.9.1 Beam Parameters

To have a proper response from the simulation, the simulation must be given accurate information about the incoming beam and information about the physical characteristics of the target and degrader foils. To properly fix these parameters, several calibration data sets are taken, all with unreacted beam. One with no foils, one with only the target foil, and then a data set with each additional foil that is added to the TRIPLEX device. Additional data sets will be taken if the secondary beam changes or if the energy of the secondary beam changes during the experiment.

First, the data set with no foils is used to parameterize the incoming beam. From this data set, the initial beam energy is determined along with the momentum width (dp). The beam particle and beam direction are also set at this time. This calibrates the beam and these parameters are not changed unless the experimental secondary beam changes. The four parameters that are used to calibrate the beam are 1) DTA, which is the momentum seen at the target area, 2) YTA, the y position at the target area, 3) and 4) ATA and BTA the angles in the x and y directions, respectively, as measured from the z axis at the target area. Figure 3.16 shows the calibration of the beam parameters DTA, ATA, BTA and YTA.

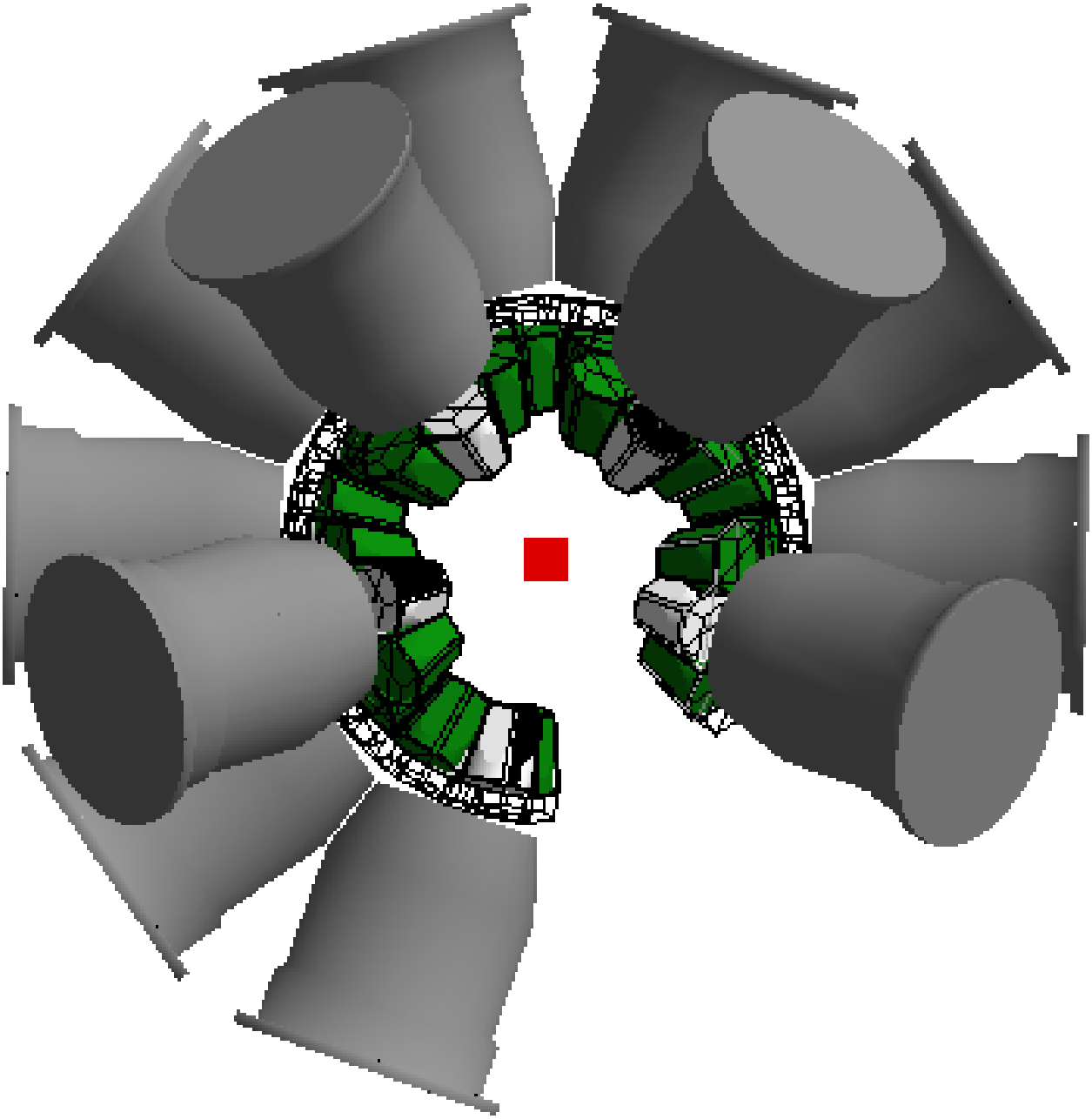

Figure 3.15: This is a figure generated with visualisation packages available in the Geant4 toolkit. It shows a rendered diagram of the GRETINA modules and crystals surrounding the beam pipe holding the foils. The view is looking down the beam axis upstream. This figure is generated with the geometry information given to the simulation.

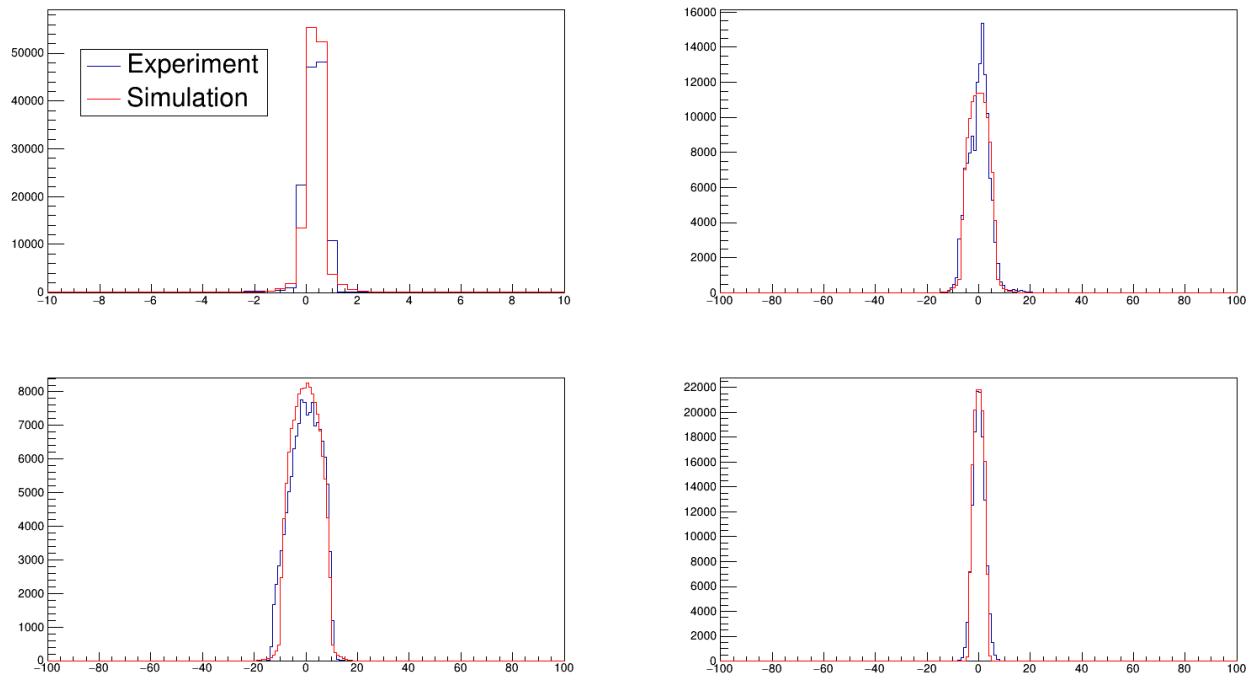

Figure 3.16: Four spectra are used to match beam parameters from data to calibrate the beam information for the simulation. The top left figure show the DTA spectrum, the top right the ATA spectrum, the bottom left the BTA spectrum and the bottom right is the YTA spectrum. Data is shown in blue and the simulated beam is in red.

Once the beam is well defined, each foil is then characterized such that the simulation can reproduce how the foils and incoming beam interact to produce the same beam profile in simulation as was seen during the calibration runs. Each foil's thickness is calibrated in this process and reproduces the same changes in the previous four parameters as was seen in the data set. The minimum list of necessary calibration data sets for a recoil distance measurement are unreacted beam, unreacted beam with a target foil, reacted beam with target foil, reacted beam with a target and degrader foil. Other important data sets would be a setting with three foils and long distance data sets. If the secondary beam changes, for each change, an additional unreacted beam measurement must be taken to reproduce the new beam in the simulation.

Chapter 4

Lifetime Analysis of ^{36}Si and ^{38}Si

Several different approaches were used to measure the lifetimes of ^{36}Si and ^{38}Si described in this work. ^{36}Si was measured using a two foil Recoil Distance Method whereas ^{38}Si was measured using a three foil Recoil Distance Method. Both used the TRIPLEX plunger device along with GRETINA to measure the gamma rays from the low-lying states in the nuclei and use the Doppler-shift effects to determine the lifetimes of the low-lying states of the Si isotopes. The magnitude of these lifetimes ranged from 1ps to 100ps, which required careful analysis to properly understand the systematic effects that impact on the lifetime results obtained.

4.1 Silicon Isotopic Chain

The Silicon isotopic chain displays shell evolution [8,9,14,19,22,24]. With ^{34}Si demonstrating a doubly magic closed shell structure at N=20 [8, 19], ^{42}Si makes a marked contrast since the expected increase in the first 2^+ state energy expected at N=28 is absent. One method to probe the collectivity of even-even nuclei is to examine the ratio of the energy of the yrast 2^+ and 4^+ states [21]. This ratio will have characteristic values for a nucleus that has a vibrational nature vs a rotational nature. These two modes produce unique level scheme structures from basic collective models of the nucleus. Figure 4.1 shows the level energy ratio for the even-even silicon isotopes from ^{34}Si to ^{42}Si. As summarized in table 4.1 this ratio

Ratio	Vibrational	Triaxial	Deformed
$E(4^+)/E(2^+)$	2	2.67	3.3
$\frac{B(E2;4^+\rightarrow 2^+)}{B(E2;2^+\rightarrow 0^+)}$	2	1.39	1.43

Table 4.1: This table summarizes the information on the characteristic ratios of the yrast energy levels and B(E2) for various types of collectivity. These values are taken from Reference [13].

will have characteristic values of 2.0 or 3.3 for vibrational or rotational nuclei respectively. The transition from vibrational towards rotational modes seems to begin at ^{38}Si by using this ratio as the determining factor.

Another way to probe the collectivity is to examine another ratio, the B(E2) ratio of the transitions between these two yrast states and the ground state. The B(E2;$4^+\rightarrow 2^+$)/B(E2;$2^+\rightarrow 0^+$) ratio again has characteristic values that can independently assess the collective nature of an even-even nucleus. However, to calculate these values, the lifetimes of both the 2^+ and 4^+ states have to be known. There are very few lifetimes of these states known in this region, as the heaviest Si isotope where both of these quantities are known is ^{30}Si with N=16 [1,62]. Therefore, an experiment was conducted to determine these lifetimes in order to deepen the understanding of the changes in the collective nature along the Si isotopic chain toward the neutron-rich regime.

4.2 Recoil Distance Measurement for ^{36}Si

The experiment used a ^{48}Ca primary beam to produce two secondary beams of ^{44}Cl and ^{45}Cl. Each of these secondary beams was identified using the timing information gathered by the S800 spectrograph. Figure 3.8 shows the spectrum where the gate on the secondary beam

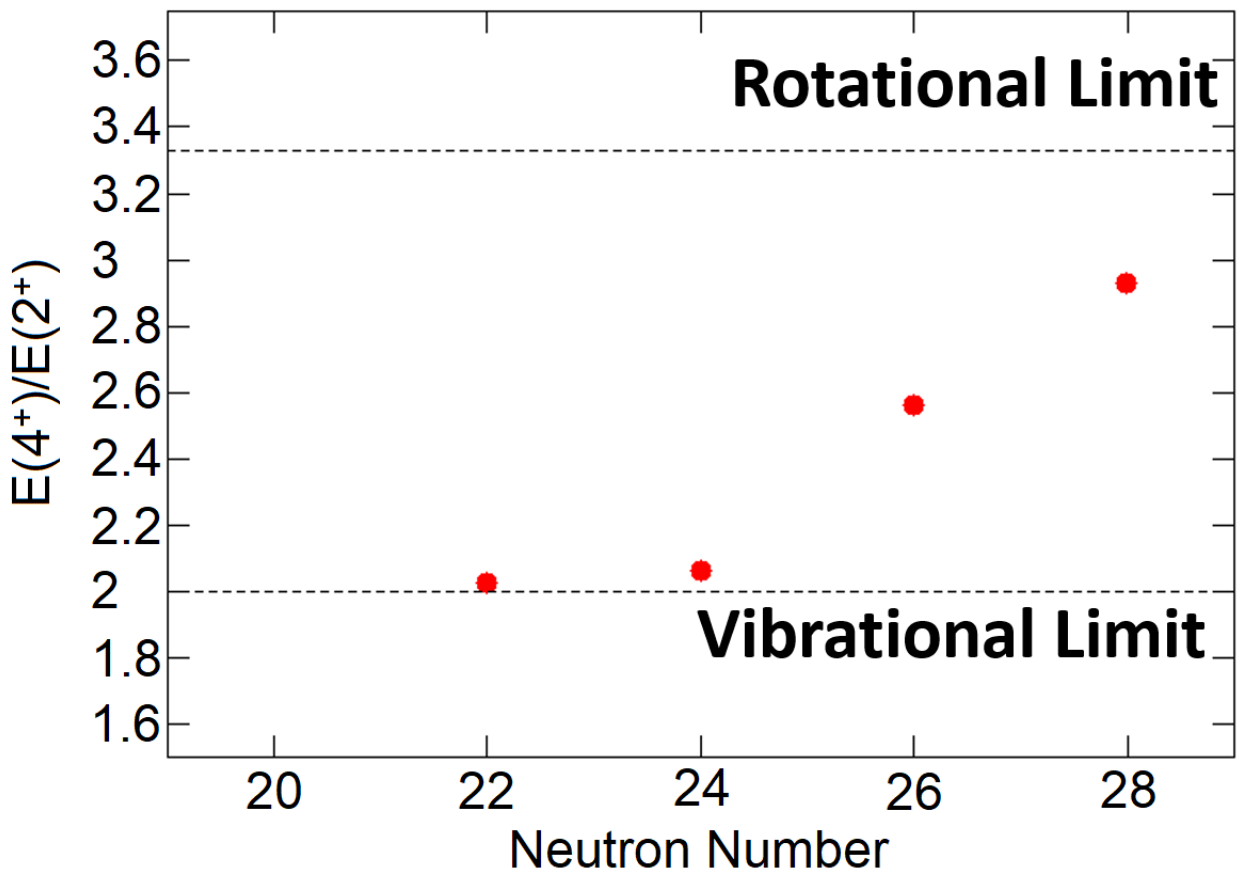

Figure 4.1: The figure shows the ratio of the energy of the gamma transition of the yrast 2^+ and 4^+ states for even-even silicon isotopes. This value is used to understand the collectivity of the nucleus and to understand some characteristics properties of the isotope. The two dotted lines show the theoretical values of the vibrational and rotational limits of this ratio that have been calculated from the energy levels of the perfect harmonic oscillator potential. Data comes from References [1, 9, 13, 19].

was made. Since the secondary beam is usually a cocktail beam of several reaction products produced by the primary beam, this spectrum is useful to clean the subsequent spectra with contaminates and allows for a better final PID spectrum. This figure's x axis is the time of flight difference between the E1 timing scintillator and the OBJ (object) scintillator in the S800 focal plane. Similarly, the y axis is the timing difference between the E1 scintillator and the XFP (extended focal plane) scintillator.

Once the secondary beam is isolated, a clean particle identification plot such as figure 3.14 can be made and then used to select the isotope of interest. Gates made on the isotopes can then be used to make the gamma ray spectra with only the gamma rays that are coincident with the gated isotope. These spectra are then able to be used to study the gamma ray transitions of the isotope. In this work, data from ^{36}Si and ^{38}Si will be discussed in further detail below.

The Recoil Distance Measurement for ^{36}Si used a two foil configuration of the TRIPLEX plunger device. The foils used in this measurement were a 2mm ^{9}Be target foil and a 0.58mm Ta degrader foil. The primary beam for this measurement was 140 MeV/u ^{48}Ca beam that was used to produce the 99 MeV/u and 89 MeV/u ^{44}Cl secondary beams. The 99 MeV secondary beam was used for the Target Only data and the 89 MeV/u beam was used for the short distance settings and the long distance setting for the two foil measurements. The goal of this measurement was to measure the lifetime of the 4^+ state and the higher lying 6^+ state. It was important to accurately characterize the feeding of the 6^+ state as the feeding modifies the apparent lifetime of the 4^+ state. The level scheme shown in figure 4.2 shows the energies of the transition and how the gamma ray cascade is structured.

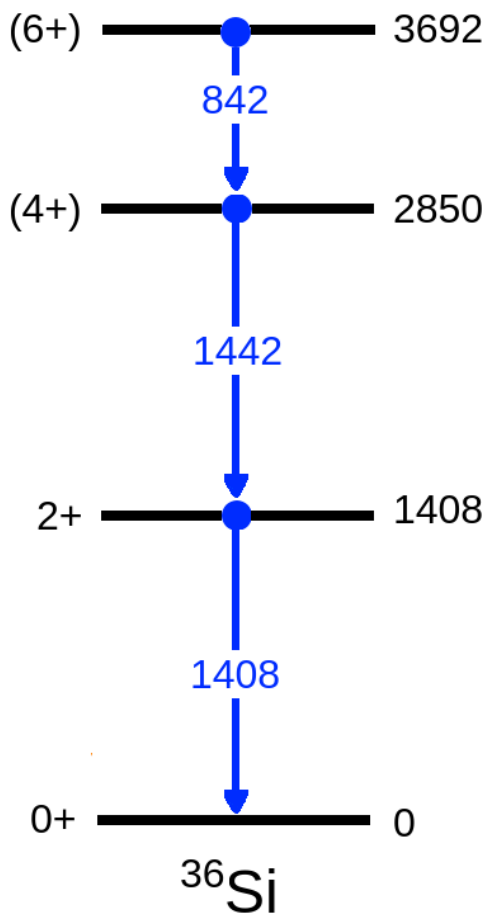

Figure 4.2: The figure shows the level scheme of ^{36}Si as taken from the NNDC [1]. The energies of the levels are given on the right and the energy of the transitions are labeled in blue. All energies are listed in keV.

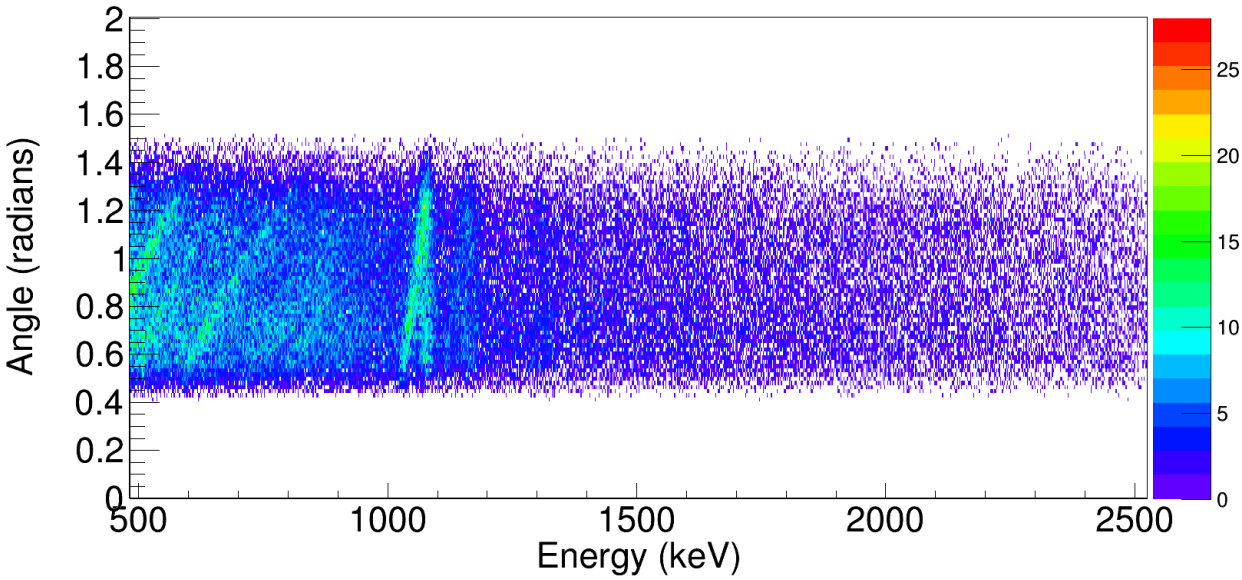

Figure 4.3: An example from a three foil ^{38}Si measurement of a two dimensional gamma ray figure. Gamma ray energy in keV is on the x axis and the y axis is the measured gamma ray emission angle (in radians) from the beam axis. The structure around 1074 keV is the $2^+ \rightarrow 0^+$ transition in ^{38}Si. The figure shows how the gamma transition is split into two components (with non-visible third components); one of which is angled and the other being a vertical line. Since the energy of a gamma ray is not Doppler shifted if it is emitted at a 90 degree angle, both components meet at $\pi/2$ radians in the center of mass frame, corresponding to approximately 1.2 radians in the laboratory frame as shown in the figure. Therefore an angle cut corresponding to 40 degrees is used in the multi foil measurement for better peak resolution while minimizing the loss of statistics.

4.2.1 Gamma ray Spectra

The following sections describe some of the various gamma ray spectra that play critical roles in the lifetime analysis using the Recoil Distance Method. All of these spectra are the gamma ray spectra measured using GRETINA along with the S800 spectrograph to make isotopic gates.

As described later, a gate is made to select gamma-ray emission angles below 40 degrees to maximize the amount of Doppler shifts in the measured spectra. On the other hand, this angle cut introduces additional background peaks where the laboratory-frame background gamma rays form peak-like structures in the Doppler-shift corrected spectra. In this work,

various neutron induced gamma rays are Doppler corrected into regions near which gamma rays of interest from ^{36}Si also fall. Figure 4.6 shows an example of a gamma ray spectrum for ^{36}Si where the neutron background is encroaching on a region of interest for the 842 keV transition coming from the 6^+ state. The two broad peaks that are outlined in blue at the base line are the two relevant neutron induced gamma rays. The right one comes from the ^{27}Al reaction and the ^{70}Ge(n,n') reaction that produces gamma rays near 1000 keV in the laboratory frame spectra.

4.2.1.1 Target Only Data

Target only data, where only the target foil was inserted into the beam line, is taken to see which states are populated in the data sets. Target only data is the cleanest of the data sets taken since there is only one foil for the beam to react in and only one velocity that the ions are traveling at since there is not anything else in the beam line to slow the reaction products. From the target only spectra, transitions are identified by energy and the initial population of each transition is determined. This data set is not sensitive to most lifetimes in the range of study for typical recoil distance method experiments. Due to the lack of lifetime effects, all gamma rays, regardless of angle are included in the spectra for these data sets.

The population is determined by analysing the Doppler shift corrected target only spectra, such as the one shown in Figure 4.4 for the ^{36}Si target only data set. Three transitions were studied using the spectrum including gamma ray peaks at 1408(1),1442(3), and 842(1) keV. Since the 1408 and 1442 keV peaks are close in energy and the effects of Doppler broadening, these two transitions are forming the large peak seen around 1420 keV. In this figure, the blue points show the data and the red line is a GEANT4 based simulation that has been

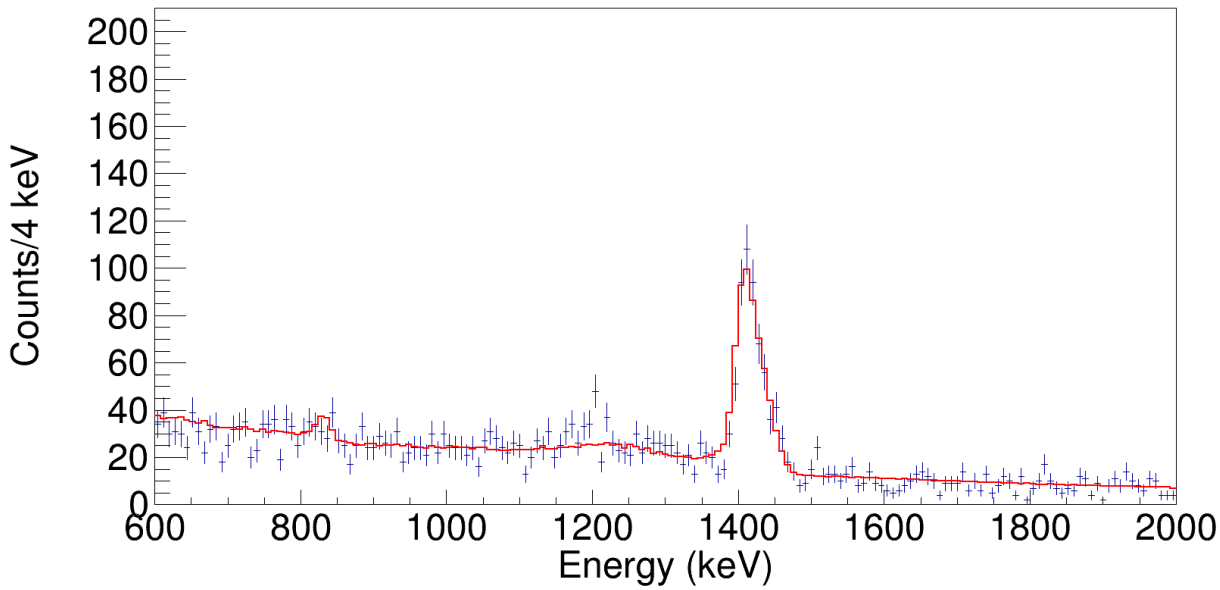

Figure 4.4: A gamma ray spectrum showing the Target Only data for ^{36}Si in blue compared with a GEANT4 simulation in red. The small peak on the left is the 6^+ transition and the larger peak on the right is a combination of the 2^+ and 4^+ transitions as they are closer in energy than the resolution of the system due to the effects of the Doppler broadening after the Doppler shift correction.

fit to the data set. The 842 keV peak was not strongly populated, but it is very important to include due to the feeding effect it caused to the 4^+ state's lifetime.

The fit to the simulations was used to determine the initial populations of each of these states. From this data set it was found that 55(6)% of the excited ^{36}Si were produced in the 2^+ state, 35(5)% in the 4^+ state and only 10(2)% in the 6^+ state. The quoted error includes the statistical uncertainties given by the fit and systematic uncertainty of 5% for the absolute efficiency determination of the system. These are added in quadrature. Ideally, the only change in the following data sets would be an addition of a degrader foil and the change of distance between these foils. Therefore, these initial populations in the reaction products produced in the target should remain constant. However, experimental conditions changed, including the beam energy, after the target only data was taken. It was assumed that these populations would remain consistent and were used in all the following data analysis portions

for ^{36}Si.

4.2.1.2 Two Foil Data

After adding the degrader foil, the gamma ray spectra become more complex. As shown in Figure 4.3, each previously seen transition is split into multiple components. These different components can be seen in the two dimensional figure that compares the gamma ray energy to the angle it was emitted from the nuclei of interest. Once Doppler corrections are applied with a proper velocity parameter β, the angular dependence of the gammma-ray energies disappear, and the components show themselves as nearly vertical lines. The slightly tilted line corresponds to the component for which the Doppler correction is not optimized. This is because only one β value is able to be chosen to complete the Doppler shift corrections, but each component has a different velocity. Since there is no shift in the energy due to the Doppler shift correction at 90 degrees, both components will meet at 90 degrees. To separate both components in a one dimensional spectra, a 40 degree angle cut is applied to all of the multi foil data sets except for the long distance data set for ^{38}Si, which will be discussed later in the chapter.

To measure the lifetimes of the excited states seen in ^{36}Si, three distance setting measurements were taken that were sensitive to the expected lifetimes of the 2^+ and 4^+ states. Those distances were 0mm, 0.5mm and 1mm between the target and first degrader foils. These distances are sensitive to lifetimes on the order of 10ps – 20ps, which is the expected lifetime range of the 2^+ and 4^+ transitions from previous experiments [35, 45, 46]. The lifetime of the 6^+ transition was unknown, but expected to be longer given the small energy spacing for the transition.

In Figure 4.5, a close view of the 2^+ and 4^+ transitions is shown for all three distance

settings. The data from the experiment is shown in blue and a GEANT4 comparison simulation is shown in red. The 0 mm data set is on the top of Figure 4.5, the 0.5 mm is in the center and the 1 mm data set is on the bottom. Three peaks can be observed in each data set. The leftmost peak is the slow component of the 1408 keV gamma ray from the 2^+ state, the central peak is the slow component of the 1442 keV gamma ray from the 4^+ state and the rightmost peak is their combined fast components. Again, these two gamma ray transitions have overlapping components due to the small energy difference between the two gamma rays and the effect of Doppler broadening.

These figures show how the relative heights of these components change with the distance setting. In the 0mm data set, the slow and fast components have roughly the same number of counts, whereas in the 1mm data set, the fast component is clearly larger than the slow components. The data was fit with GEANT4 simulations and a χ^2 analysis was performed to determine the lifetime of these excited states.

Due to the complication of the overlapping components, the literature value for the 2^+ transition was adopted as the value for the lifetime of the 2^+ state in ^{36}Si, 3.9(+1.1-0.6)ps [1, 19]. The lifetime of the 4^+ transition was then determined to be 10.3(3.1)ps. The quoted error includes the statistical error determined from the fit(0.7ps) as well as systematic errors due to the feeding effects(3ps) and degrader contributions(0.3ps) added in quadrature. The summary is given later in the chapter. The simulation shown in red is a simulation with 3.9ps for the lifetime of the 2^+ and 10ps for the 4^+ transition. Note that this analysis included the feeding effects from the 6^+ state as well as contributions from reactions in the degrader, as mentioned below.

Figure 4.6 shows a spectrum containing the 6^+ transition. This spectra also includes two neutron induced background components around 650 keV and 800 keV. The component that

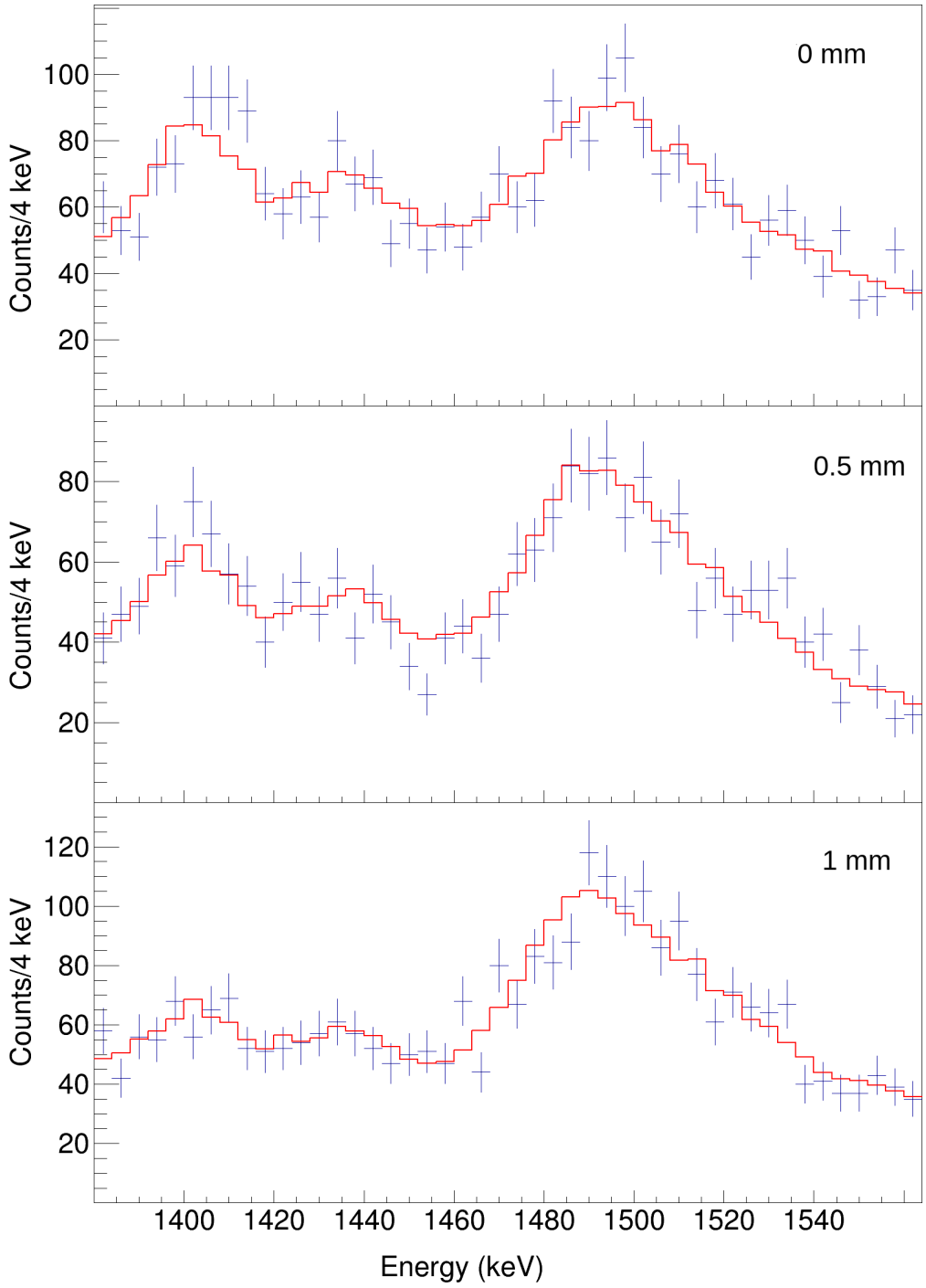

Figure 4.5: This figure shows the gamma ray spectra focused on the two foil data using a 2mm Be target and a 0.58mm Ta degrader for ^{36}Si. The top figure shows the 0mm separation distance data set with the 0.5 mm data set immediately below and the 1mm data set is the bottom spectra. For all three, the data is shown in blue with a comparison with a GEANT4 simulation in red with the 4^+ lifetime being 10ps.

is around 800keV does interfere with the 826 keV 6^+ slow component and must be taken into account. The background components were constrained by examining the laboratory frame spectra and important background components were identified and quantified. Figure 4.8 shows a laboratory frame spectra with background components identified in the upper portion of the figure and how they are affected by the Doppler shift correction to the center of mass frame is shown in the lower portion of the figure. These quantities were then simulated and added into the fitting routine such that the lifetime of the 6^+ gamma ray transition was able to be properly determined without a bias due to uncounted background components in the sensitive region of the transition. The effective lifetime for the 6^+ state was thus determined to be 98(12)ps.

4.2.1.3 Long distance data

The recoil distance method applied with relativistic rare isotope beams in this work needs to account for reaction contributions in the degrader, which adds counts to the slow component peak, effectively increasing the lifetime result if these contributions are neglected. These reactions are measured in the long distance data set.

Figure 4.7 shows the long distance data set for ^{36}Si. The distance between the foils was 22 mm and a 40°angle cut has been applied to see separation in the fast and slow components. The peak at 1420 keV is the combined fast components from the 2^+ and 4^+ transitions and the peak at 1400 keV is the combined slow components. The broad peak around 1200 keV is the Compton scattering component. Compton scattering is never fully reproduced in the simulations due to not every component of the experimental vault being simulated. The leftmost structure includes the fast and slow components for the 6^+ transition as well as the background contributions from the neutron-induced reaction (see Figure 4.8).

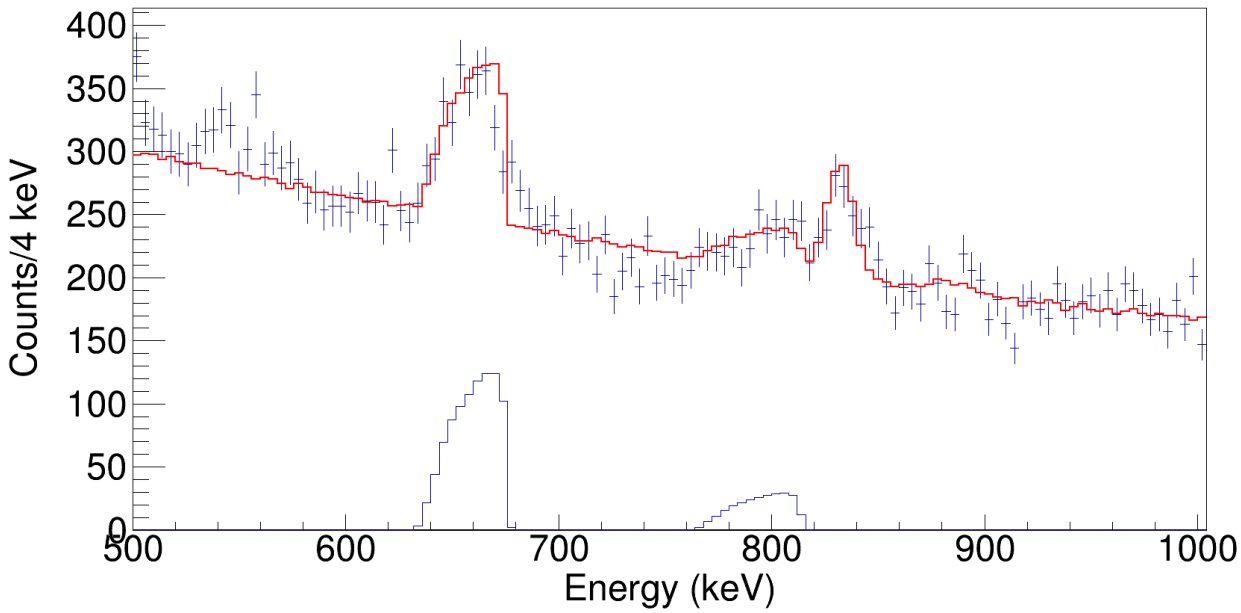

Figure 4.6: A gamma spectra showing the effects of neutron background reactions. Data with distance settings 0mm, 0.5mm and 1mm separations are added in the figure. The peak shown on the left is the Doppler shifted component of the ^{27}Al reactions at 850 keV. The small component to the left side of the other feature is the Doppler shifted component of the ^{27}Al reaction and the ^{70}Ge(n,n') reaction around 1000 keV. The right side of the feature around 840 keV is the slow component of the 6^+ transition in ^{36}Si. The is data shown by the cross symbols where the vertical lines represent statistical errors. Simulated neutron background contributions shown in blue below the fit. The red line is the GEANT4 simulation with the added neutron background.

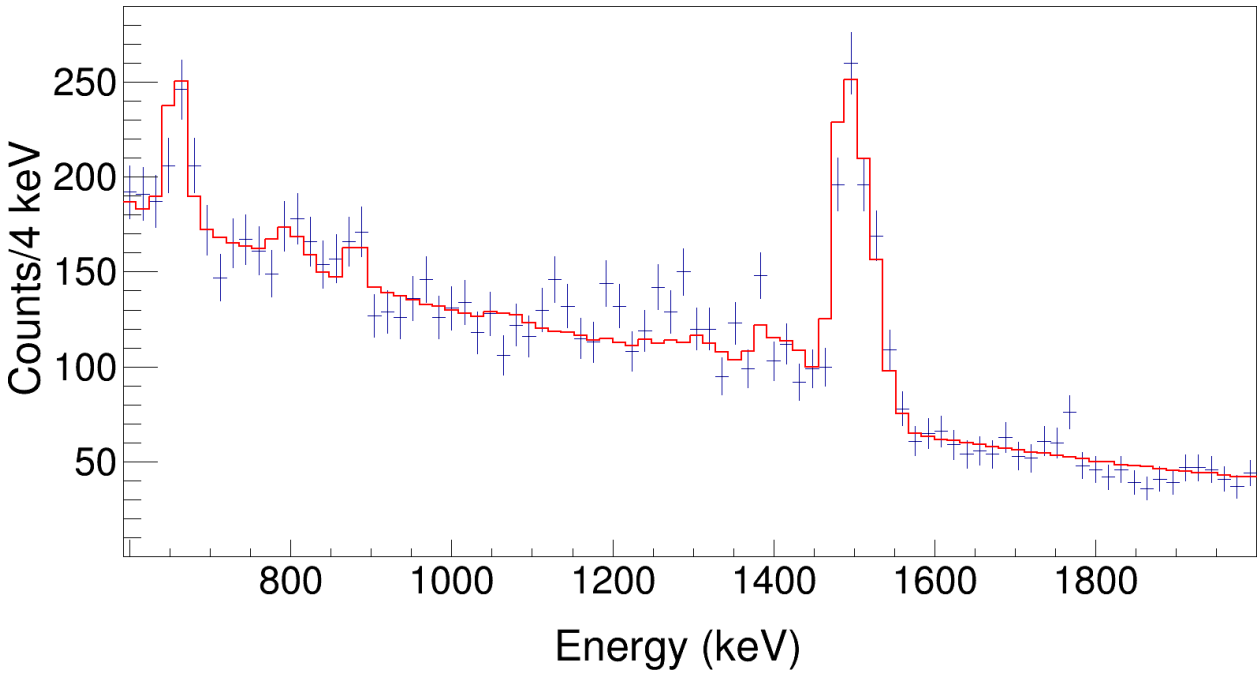

Figure 4.7: The long distance ^{36}Si gamma ray spectrum. The distance between the target and first degrader foils was 22mm. This spectra is used to constrain the ratio of reaction products being produced in the degrader as compared with the products being produced in the target foil.

This distance corresponds to approximately 220 ps of flight time. This is several times the lifetimes expected for the 2^+ and 4^+ states and more than twice the lifetime of the weakly populated 6^+ state. This time allows for the reaction products created in the target to decay before the beam encounters the degrader foil. Therefore, the slow peak measures the reaction products created in the degrader and the fast peak measures the reaction products created in the target. This data set constrains the amount of reaction products created in the degrader. The ratio of reaction products created in the target vs the degrader was determined to be 3(+2-1).

4.2.2 Laboratory Frame Background

Figure 4.8 shows the laboratory frame gamma spectrum in the upper portion with several common neutron induced background gamma rays. The ones that are marked include several isotopes of germanium neutron induced reactions that come from neutrons reacting in the germanium of the detectors and various ^{27}Al reactions where the neutrons react with the aluminum beam pipe. These gamma peaks will shift in energy when the Doppler shift correction is applied to study the in-flight gamma rays from the nuclei of interest. The bottom portion shows where these transitions move after the Doppler shift correction.

Figure 4.3 shows what the Doppler shift corrected neutron background transitions look like in the center of mass frame. The diagonal lines on the left side of the figure correspond to some of the lower lying prominent transitions seen in Figure 4.8. If no angle cut is applied, the neutron background is not as noticeable since it forms a very wide, broad peak. However, if an angle cut is applied after the Doppler shift correction, as is done in the lifetime analysis, these transitions can cause a distinct peak in the spectrum. This effect can be seen in Figure 4.6 where the two peaks shown at the bottom of the spectra correspond to ^{27}Al and germanium reactions near 843 keV and 1014-1040 keV in the laboratory frame. The key background component for this experiment comes from the background gamma rays at 1014 keV in the laboratory frame.

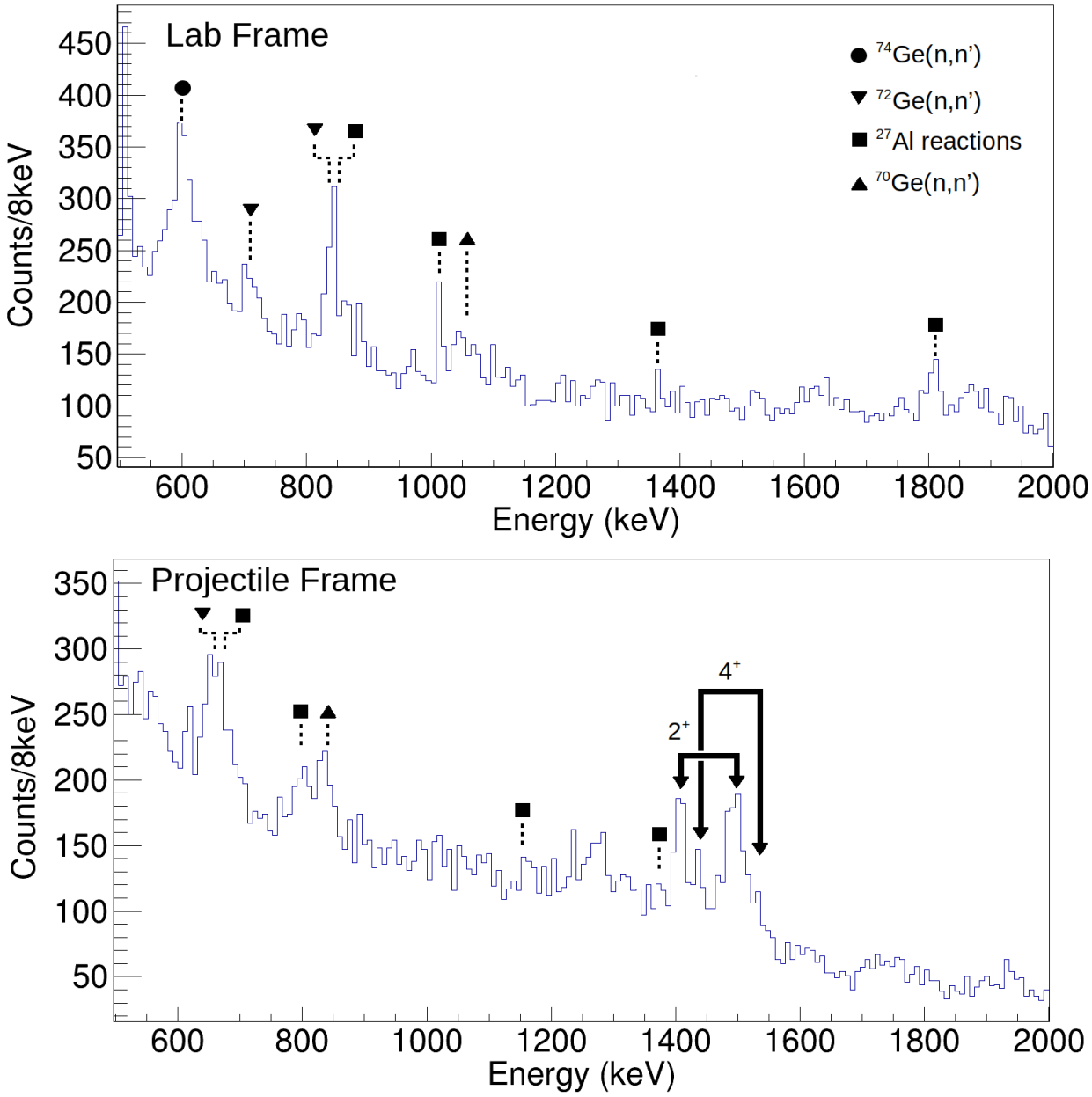

Figure 4.8: The top spectrum shows the laboratory frame gamma spectra with the peaks corresponding to the various background reactions. The bottom spectrum shows how these reactions shift in energy after the Doppler shift correction has been applied to reconstruct the ^{36}Si transitions.

4.3 Recoil Distance Measurement for ^{38}Si

4.3.1 Gamma ray Spectra

The Recoil Distance Measurement for ^{38}Si used a three foil configuration of the TRIPLEX plunger device. The foils used in this measurement were a 2mm ^{9}Be target foil, a 0.58mm Ta first degrader foil and a 0.25mm Ta second degrader foil. The primary beam for this measurement was 140 MeV/u ^{48}Ca beam that was used to produce the 102 MeV/u ^{45}Cl secondary beams. The secondary beam was used for all data sets discussed here. The goal of the experiment was to measure the lifetime of the 2^+ state and the 4^+ state and to constrain the lifetime of the higher lying state with unknown J^π. The level scheme shown in figure 4.9 shows the energies of the transitions and what gamma ray cascade this experiment supports. This is a partial level scheme simplified to contain only the transitions seen here.

4.3.1.1 Target Only Data

Figure 4.10 shows the target only gamma spectrum for the target only data. Three gamma ray transitions were clearly seen in the spectrum, the 1074(2) kev gamma ray, the 1159(2) keV gamma ray and the gamma ray at 1308 keV. The 2382 keV state energy was not well constrained by previous experiments and is in agreement within error of Reference [63]. In this figure, the blue points show the data and the red line is a GEANT4 based simulation that has been fit to the data set. The 1308 keV peak was not strongly populated, but it is important to include in order to confirm the energy of the state and constrain the lifetime of the 2382 keV state.

The fit to the simulations was used to determine the initial populations of each of these states. From this data set it was found that 31(3)% of the excited ^{38}Si were produced in the

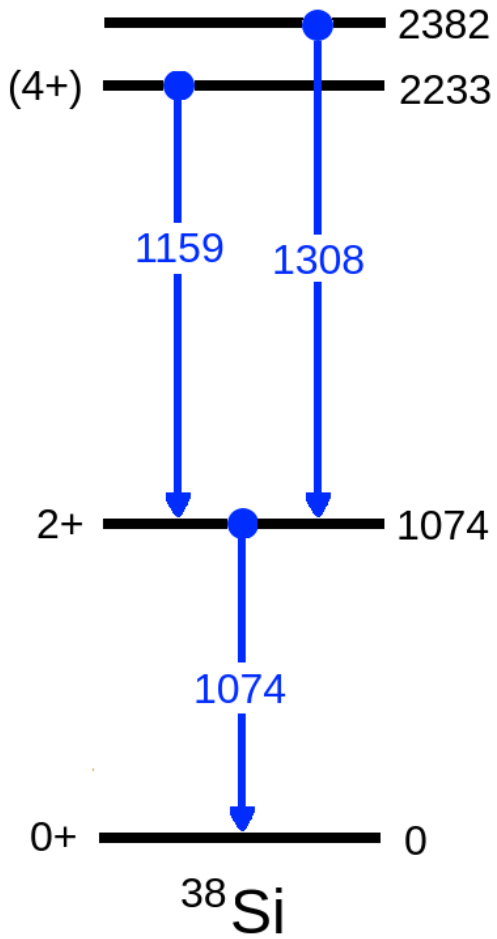

Figure 4.9: A partial level scheme for ^{38}Si with information experimentally determined by this work. Spin and parities of the states are listed on the left hand side and the energy of the states are listed in keV in black on the right hand side. Transitions that were seen are shown in blue arrows and the energies are in keV in blue.

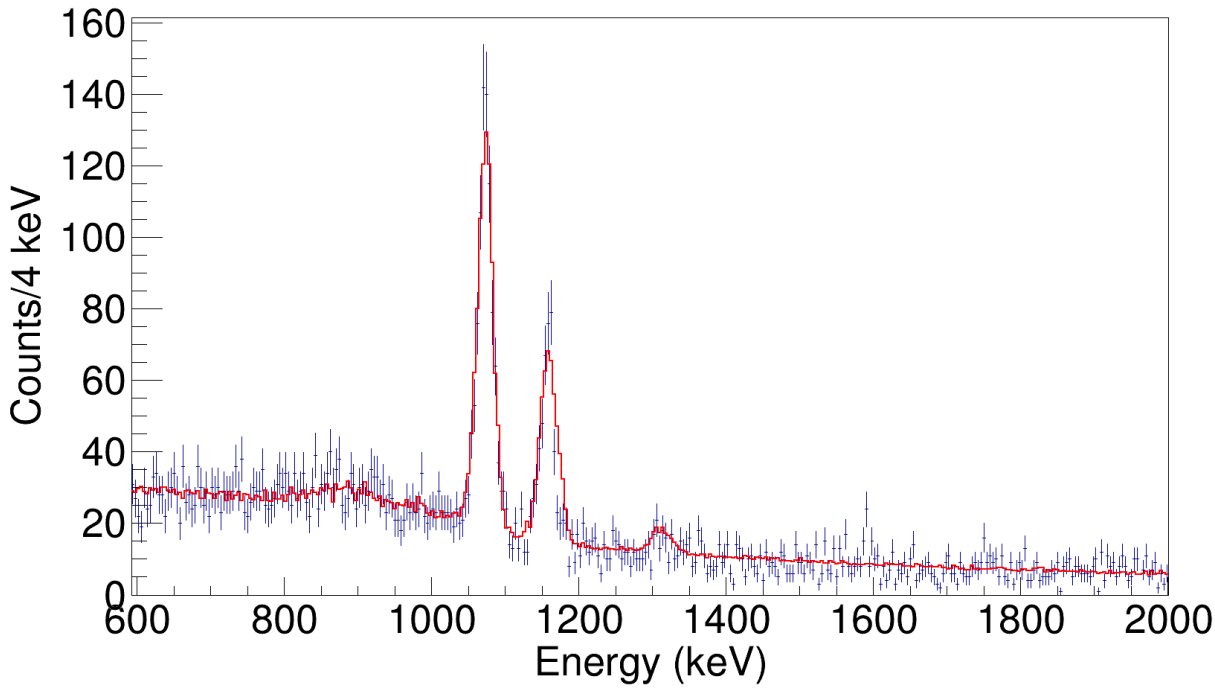

Figure 4.10: The figure shows the target only data for ^{38}Si. Three transitions are visible with gamma ray energies of 1074 keV, 1159 keV, and 1308 keV.

2^+ state, 59(3)% in the 4^+ state and only 10(5)% in the 2382 keV state. The only change in the following data sets was the additions of the degrader foils and the change of distance between these foils; therefore, these initial populations in the reaction products produced in the target should remain constant. The assumption was made that these populations would remain constant and were used in the data analysis portions for ^{38}Si.

4.3.1.2 Three Foil Data

To measure the lifetimes of the excited states in ^{38}Si, a three foil TRIPLEX measurement was performed. One distance setting sensitive to the lifetimes of the excited states was used. The distance between the target and first degrader was 1mm and the distance between the first and second degrader was 10mm. The distance between the target and first degrader was sensitive to lifetimes on the order of 10ps – 20ps, which is the expected lifetime range of

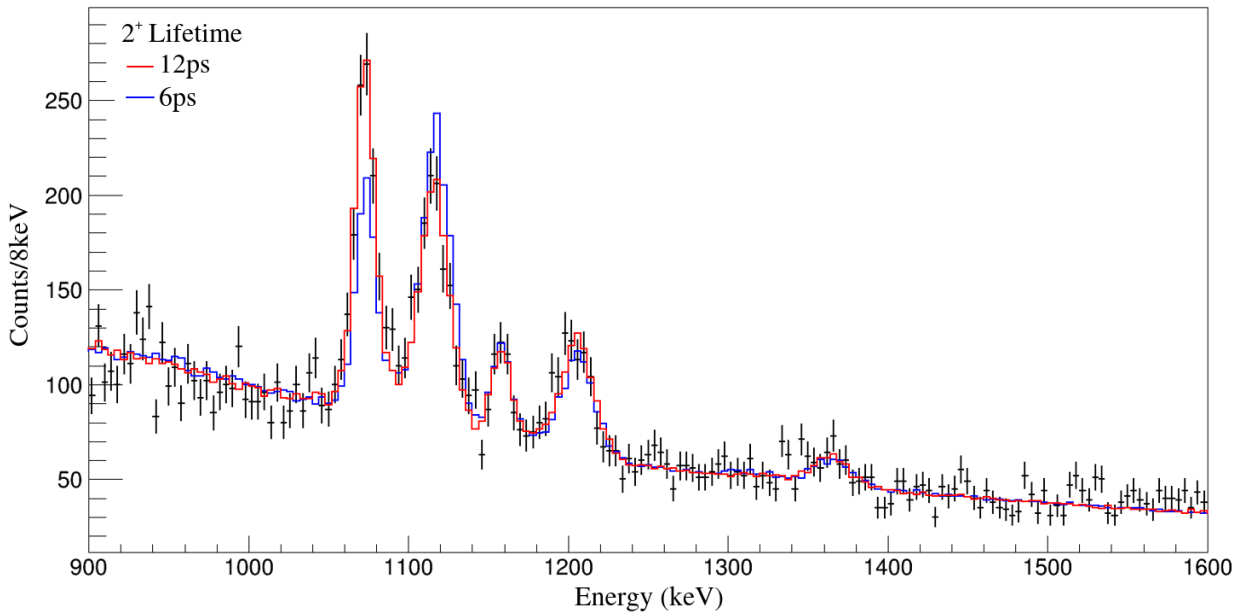

Figure 4.11: The three foil ^{38}Si gamma ray spectrum. The distance between the target and first degrader foils was 1mm and the distance between the first and second degraders was 10mm. This spectra is used to determine the lifetime of the excited states. The red and blue lines show GEANT4 simulations with a simulated 2^+ lifetime of 12ps and 6ps respectively.

the 2^+ and 4^+ transitions from previous experiments [23]. The second distance, between the first and second degraders, was sensitive to lifetimes on the order of 100ps. Since no states in ^{38}Si seen in this experiment were this long, there was no strong second degrader component seen for any transitions. In figure 4.11, a full spectrum showing transitions from the 2^+, 4^+ and 2382 keV states are shown for the three foil data set. The data from the experiment is shown in black and two GEANT4 comparison simulations are shown in red and blue. Five peaks can be observed in the spectra. From left to right they are: the reduced component of the 1074 keV gamma ray, the fast component of the 1074 keV gamma ray, the reduced component of the 1159 keV gamma ray, the fast component of the 1159 keV gamma ray, and the fast component of the 1308 keV gamma ray from the 2382 keV state.

The data was fit with GEANT4 simulations and a χ^2 analysis was performed to determine the lifetime of these excited states. The red line shows a simulation using 12ps, 13ps and

3ps for the 2^+, 4^+, and 2382 keV states respectively. The blue line shows an example where the 2^+ lifetime is 6ps.

Figure 4.11 shows a single broad peak for the 2382 keV transition. The peak is broader than the peaks for the gamma rays coming from the 2^+ and 4^+ states. This is due to the effect of the thick target combined with the short, on the order of 1ps, lifetime of the 2382 keV state [64]. Since the target is 2mm thick, the beam takes roughly 20ps to pass fully through the target and can react at any point within. Since the lifetime of the 2382 keV state is much shorter than 20ps, ^{38}Si is reacted and decays at many points within the target causing a continuum of velocities at which the 2382 keV state decays rather than one distinct velocity as seen in decays between the foils.

Due to the low statistics and the fast nature of the transition, only the upper limit of 5ps was determined for the lifetime of the 2382 keV state. The lifetime of the 2^+ and 4^+ states were determined to be 12.6(+2.2-1.4) ps and 13.2(+1.8-1.4) ps respectively. The errors included the contributions from the statistical error, the feeding from the 4^+ state and the contributions from the reaction products from the degrader foils.

4.3.1.3 Long distance data

To constrain reaction products produced in the degrader foils for the three foil measurement, a long distance data set was taken. The distance between the target and first degrader was 25mm and the distance between the first and second degraders was also 25mm. This corresponds to roughly 250ps of flight time, well above the lifetimes expected from the excited states in ^{38}Si which allowed for the reaction products produced in the degraders to be measured.

In Figure 4.12, the slow peak measures the reaction products created in the second

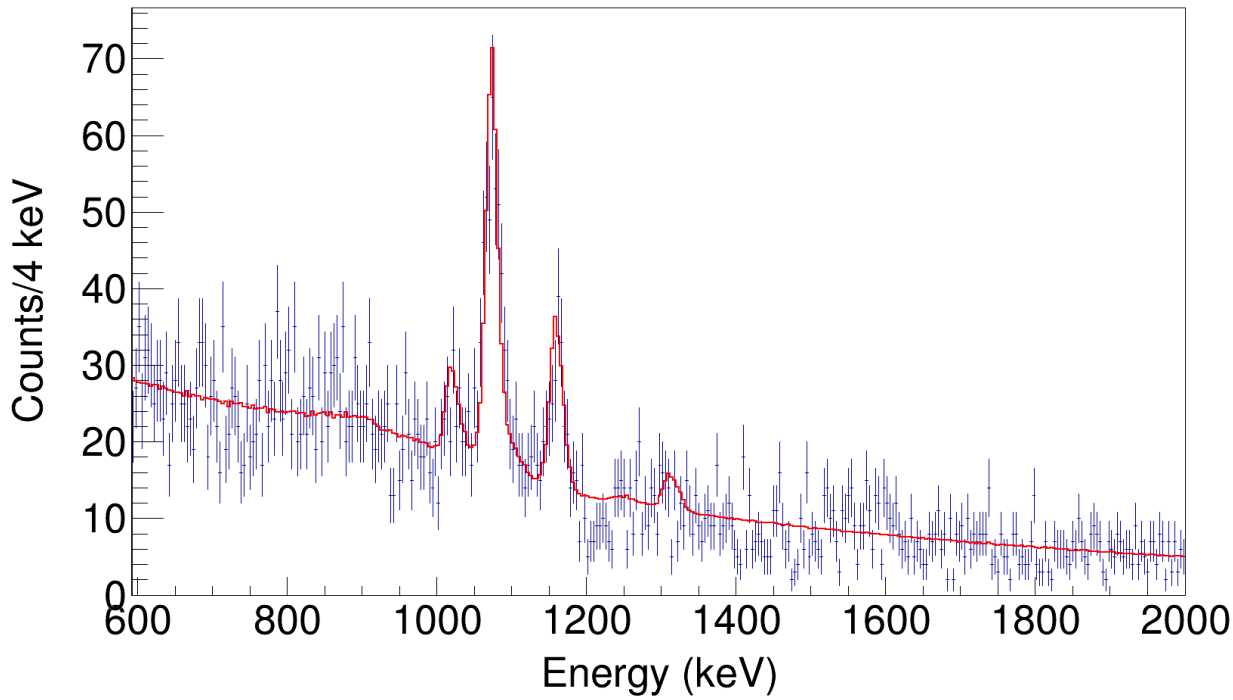

Figure 4.12: The long distance ^{38}Si gamma ray spectrum. The distance between the target and first degrader foils was 25mm and the distance between both degraders was also 25mm. This spectra is used to constrain the ratio of reaction products being produced in the degraders as compared with the products being produced in the target foil.

degrader, the reduced peak measures the reaction products created in the first degrader, and the fast peak measures the reaction products created in the target. Due to the second degrader being very thin, no strong slow component was observed for any transition. The left most peak is the reduced component of the 1074 keV gamma ray, the tallest peak is the combined fast component from the 1074 keV gamma ray and the reduced component from the 1159 keV gamma ray. This combination of components causes the asymmetric tail seen on this peak. The peak to the right of the combined peak is the fast component of the 1159 keV gamma ray. The small peak on the right is the fast component, and only component, seen from the 2382 keV state. From this data set the amount of reaction products produced in the degrader are constrained. The ratio of reaction products created in the target vs degrader was determined to be 1.4(1).

4.3.2 Laboratory Frame Background

The laboratory frame spectra was analyzed for ^{38}Si in the same manner as for ^{36}Si. A similar spectrum to Figure 4.8 was produced and studied. However, unlike in the case for ^{36}Si, no neutron induced background gamma rays were produced that would impact the regions in which the gamma rays seen from the excited states in ^{38}Si are located.

4.4 ^{36,38}Si Lifetime Analysis

The lifetime results of the analysis of ^{36}Si and ^{38}Si are summarized in table 4.2. Errors were first considered from the effects of the reaction products produced in the degrader(s). A χ^2 analysis was performed to determine how changes in the ratio of reaction products in the target vs degrader affected the lifetimes of the states. Then how contributions from the 6^+ state in ^{36}Si and the 4^+ state in ^{38}Si affected the next state in their respective gamma-ray cascade were considered. Finally, another χ^2 analysis was used to determine the statistical error of each lifetime.

Nucleus	State	State Energy keV	Population %	Gamma Energy keV	Lifetime ps
^{36}Si	2^+	1408(1)	55(6)	1408(1)	3.9 (+1.1-0.6)[1]
	4^+	2849(4)	35(5)	1442(3)	10.3 (3.1)
	6^+	3691(4)	10(2)	842(1)	98 (12)
^{38}Si	2^+	1074(2)	59(3)	1074(2)	12.6 (+2.2-1.4)
	4^+	2233(3)	31(2)	1159(2)	13.2 (+1.8-1.4)
	J^π	2382(20)	10(5)	1308 (15)	

Table 4.2: This table summarizes the information on the quantities measured in this experiment for the various transitions seen. Table includes the state information including the initial population in percentage, the energy of the state in keV, the energy of the gamma ray emmitted from the state in keV and the lifetime of the state. All lifetimes are as measured in this experiment except for the one marked with a [1], which is the accepted NNDC value.

Chapter 5

Discussion of Results

The experiment was able to determine lifetimes of the first 4^+ and 6^+ states in ^{36}Si as well as the first 2^+ and 4^+ states of ^{38}Si. Experimental results in this work are summarized in Table 5.1. These lifetimes were then used to calculate the reduced transition strengths, B(E2) which provide critical information on the structure of the nuclei. The B(E2) probes the collectivity of the nuclei by giving information about how strongly two states are connected via E2 transitions. In this chapter, the measured B(E2) values and their ratios are discussed in comparison to the predictions from large-scale shell model calculations.

The present data of B(E2) for ^{36,38}Si displays the B(E2) ratio between the 4^+ and 2^+ decays (denoted $B_{4/2}$ ratio hearafter) less than 1 as consistently predicted in the shell model calculations. The vast majority of the nuclei with a known $B_{4/2}$ ratio fall within the range of the calculated rotational limit and the vibrational limit, 1.43 to 2.0 respectively [65]. As shown in the data compilation shown in Figure A1 in Appendix A, nuclei with $B_{4/2}$ less than one typically occur around the classical magic numbers [12]. This indicates that ^{36}Si and ^{38}Si share some of the same characteristics as nuclei that display a closed shell structure with reduced collectivity.

In addition the ^{38}Si 2382 keV state that had been previously seen, but the spin and parity of this state hadn't been confirmed. However, this experiment didn't collect enough information to definitively determine the J^π of this state. Further experiments would be needed to conclusively determine the spin and parity assignment for this state.

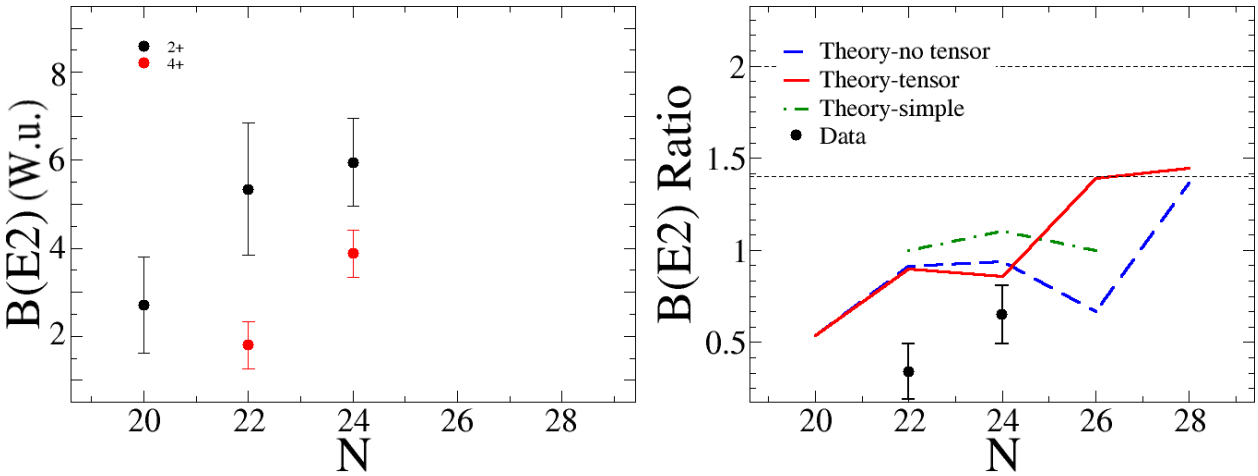

Figure 5.1: The left plot shows the known B(E2;$2_1^+ \rightarrow 0_1^+$) values in black and the (E2:$4_1^+ \rightarrow 2_1^+$) values in red for even-even isotopes of Si with Neutron numbers (N) from 20 to 28. The right plot compares the ratio of the B(E2) values for both ^{36}Si and ^{38}Si measured in this experiment and the theoretical ratios summarized in table 5.2.

5.1 Experimental Systematics Along Isotopic Chain

One B(E2) value or energy ratio holds information on the collectivity of a nucleus, but of more interest is usually how these values change along an isotopic chain. While the yrast 2^+ and 4^+ states are known for all of the even-even silicon isotopes from N=20 to N=28, very few B(E2) values had been measured. In particular, none of the B(E2;$4_1^+ \rightarrow 2_1^+$) in this intriguing region where the shell structure is drastically changing were previously known. This experiment provides the first measurement of this quantity for both ^{36}Si and ^{38}Si. Figure 5.1 shows the known B(E2;$2_1^+ \rightarrow 0_1^+$) and B(E2;$4_1^+ \rightarrow 2_1^+$) in the left figure. The right side of the figure compares the experimental (black) B(E2) ratios along with three theoretical calculations of the ratios taken from Table 5.2. Also labeled are the vibrational (1.43) and rotational (2.0) limits between which most known B(E2) ratios in the nuclear chart fall [65].

5.2 Comparisons to Shell Model Calculations

Several shell model calculations for the even-even silicon isotopes from N=20 to N=28 are compared to present data. The calculations compared three kinds of interactions, a simple model filling the $f_{7/2}$ shell with neutrons [66], one without the tensor interaction, and one that includes the tensor force [14]. The tensor force calculation used the SDPF-MU effective interaction which includes the specific tensor interaction described in Chapter 1. Table 5.2 summarises the results of this calculation in the first set of A_p, A_n and B(E2) values. The calculation without the tensor force component used the SDPF-MU interaction which has the tensor component removed from the calculation. Table 5.2 summarises the results of this calculation in the second set of A_p, A_n and B(E2) values. The bare E2 matrix elements, A_p and A_n were calculated for both the $2_1^+ \rightarrow 0_1^+$ and $4_1^+ \rightarrow 2_1^+$ transitions for every isotope. This allowed for the B(E2) values to be calculated according to equation 5.1 using the effective charges $e_p = 1.35$ and $e_n = 0.35$ for protons and neutrons respectively. From these values, the B(E2) ratio, B(E2;$4_1^+ \rightarrow 2_1^+$)/B(E2;$2_1^+ \rightarrow 0_1^+$), to be calculated and compared to the B(E2) ratios measured in the experiment for both ^{36}Si and ^{38}Si.

$$B(E2; J_i \rightarrow J_j) = \frac{(e_p * A_p + e_n * A_n)^2}{(2J_i + 1)} \tag{5.1}$$

Figure 5.1 compares the three theoretical calculations of the B(E2) ratio with the ratios measured in this work. For the SDPF-MU calculations, the SD indicates that the sd shell is occupied with protons and the PF indicates that neutrons are in the pf shell, however both calculation's predictions on the $B_{4/2}$ ratios for ^{36,38}Si are surprisingly similar to those given by the $f_{7/2}$ shell model which involves active neutrons only in the $f_{7/2}$ shell. This indicates that strong shell closures at Z=14 and N=28 are suggested by the theory and the current

data supports this view. There is no strong impact from the tensor force addition until ^{40}Si at N=24 and enhanced collectivity is driven by the tensor force only at N=26 and after, moving the $B_{4/2}$ ratio towards the collective values. The consistency between the present data and shell model calculations in the $B_{4/2}$ trends support this view and points to the persistence of the shell closure (Z=14 and N=28) for ^{36,38}Si. It should also be mentioned that the present experimental $B_{4/2}$ ratios are even smaller than shell-model predictions. Note that the B(E2) result of 45.2(+7.9-5.0)e^2fm^4 for the 2^+ decay of ^{38}Si is consistent with the literature values of 38.6(142)e^2fm^4 [19] and 51.8(94)e^2fm^4 [67], which also agree with the SDPF-MU shell model predictions with tensor shown in Table 5.2. Therefore further understanding on the reduced collectivity for the 4^+ state would remain an intriguing open question.

As summarized in Table 5.1, the result of the $B(E2;6_1^+ \rightarrow 4_1^+)/B(E2;2_1^+ \rightarrow 0_1^+)$, ratio for ^{36}Si of 0.52(18) is also smaller than one, indicating the reduced collectivity for higher spin states. The SDPF shell model without the tensor interaction predicts B(E2) values of 27.58 e^2fm^4 and 11.98 e^2fm^4 for the 2^+ and 6^+ decays, respectively, yielding the B(E2) ratio of 0.43. This value is also consistent with the prediction (0.45) given by the $f_{7/2}$ model [66], confirming the single particle character of the low-lying E2 excitation in ^{36}Si.

As compared in Figure 5.1, the divergence of the theories at ^{40}Si indicate that the $B_{4/2}$ ratio is a sensitive probe to track the evolution of the collectivity. This change was not seen in the energy ratio [14], which can also probe the collectivity. It would be interesting to test by a lifetime measurement of the 2^+ and 4^+ states in ^{40}Si in the near future.

Isotope	$\mathbf{J}_i \rightarrow J_f$	**Gamma Energy (keV)**	**Lifetime (ps)**	**B(E2)**	**B(E2) Ratio**	**Energy Ratio**
^{36}Si	$2_1^+ \rightarrow 0_1^+$	1408(2)	$3.9^{+1.1}_{-0.6}$	$37.7^{+10.6}_{-6.8}$	—	—
	$4_1^+ \rightarrow 2_1^+$	1442(3)	$10.3^{+3.1}_{-3.1}$	12.7(38)	0.34(15)	2.02
	$6_1^+ \rightarrow 4_1^+$	842(1)	98(12)	19.6(25)	0.52(18)	2.62
^{38}Si	$2_1^+ \rightarrow 0_1^+$	1074(2)	$12.6^{+2.2}_{-1.4}$	$45.2^{+7.9}_{-5.0}$	—	—
	$4_1^+ \rightarrow 2_1^+$	1159(2)	$13.2^{+1.8}_{-1.4}$	$29.5^{+4.0}_{-3.1}$	0.65(18)	2.08

Table 5.1: A summary of the information gathered in this experiment. Lifetimes and B(E2) values for the transitions measured are listed in the table. The lifetime for the 2_1^+ transition in ^{36}Si is taken from Reference [1]. All B(E2) ratios are with the listed transition to the B(E2;$2_1^+ \rightarrow 0_1^+$).

Isotope	$J_i \rightarrow J_f$	$\mathbf{A}_p$	$\mathbf{A}_n$	**B(E2)** (e^2fm^4)	**Ratio**	$\mathbf{A}_p$	$\mathbf{A}_n$	**B(E2)** (e^2fm^4)	**Ratio**
^{34}Si	$2_1^+ \rightarrow 0_1^+$	9.595	0.000	33.56	—	9.595	0.000	33.56	—
	$4_1^+ \rightarrow 2_1^+$	9.450	0.000	18.08	0.54	9.450	0.000	18.08	0.54
^{36}Si	$2_1^+ \rightarrow 0_1^+$	6.021	11.731	29.94	—	5.776	11.273	27.58	—
	$4_1^+ \rightarrow 2_1^+$	7.098	17.022	26.83	0.90	6.958	16.154	25.16	0.91
^{38}Si	$2_1^+ \rightarrow 0_1^+$	5.853	18.245	40.83	—	5.074	16.890	32.57	—-
	$4_1^+ \rightarrow 2_1^+$	6.729	24.781	35.04	0.86	6.249	23.403	30.72	0.94
^{40}Si	$2_1^+ \rightarrow 0_1^+$	7.505	22.388	64.57	—	4.607	18.418	32.08	—
	$4_1^+ \rightarrow 2_1^+$	12.729	32.113	89.77	1.39	5.053	20.144	21.38	0.67
^{42}Si	$2_1^+ \rightarrow 0_1^+$	11.296	25.259	116.07	—	7.865	20.723	63.87	—
	$4_1^+ \rightarrow 2_1^+$	18.326	40.402	167.97	1.45	12.526	31.786	87.33	1.37

Table 5.2: This table summarizes the information from two shell model calculations. The first set of values used the SDPF-MU effective interaction(with tensor component). The second set used the SDPF-MU interaction(without tensor component). The calculations are used to determine the B(E2) values for the even-even isotopes of Si from ^{34}Si to ^{42}Si. A_p and A_n are the bare E2 matrix elements. The B(E2) values were calculated using the effective charges $e_p = 1.35$ and $e_n = 0.35$ for protons and neutrons respectively.

Chapter 6

Conclusion

The work described in this dissertation furthered research into the changes in the collectivity of nuclei near the island of inversion. A measurement of lifetimes of the 2_1^+ and 4_1^+ states allowed the reduced electromagnetic transition strengths to be determined and they offer a powerful tool to probe the structure of nuclei. These measurements were conducted using the recoil distance method which used several devices in combination such as GRETINA and the TRIPLEX plunger to determine the lifetimes of the excited states in the neutron-rich isotopes of ^{36}Si and ^{38}Si. This experiment was performed at the National Superconducting Cyclotron Laboratory using the Coupled Cyclotron Facility, including the A1900 fragment separator and S800 spectrograph.

The lifetimes of the 4_1^+ and 6_1^+ states in ^{36}Si and the 2_1^+ and 4_1^+ states in ^{38}Si were measured and added to the information known about the nuclei in this isotopic chain. The B(E2) of interest to calculate its ratio were not previously known for silicon isotopes beyond ^{30}Si. This experiment added information on the B(E2) ratio for the neutron-rich Si isotopes. Significantly, they were both surprisingly small, less than one. B(E2) ratios less than one are very rare for isotopes not along magic number lines near stability. The experimental results were compared to three theoretical calculations. One was the simple single-particle picture which serves as a reference value to consider the trend of the B(E2) ratio. Two shell model calculations, performed, both in the SDPF model space and with and without the tensor force contributions are compared. Both shell model theories predicted the surprising B(E2)

ratio less than one and are both in line with the experimental results. However, the two theories diverge in their predictions for ^{40}Si and ^{42}Si, showing the importance of the tensor force effects approaching N=28.

Consequently, further work into the structure and collectivity of ^{40}Si and ^{42}Si would be useful for determining the effects of the tensor force in the evolving collectivity of the neutron-rich silicon isotopes. Additional research would include investigating whether or not the bubble structure found in ^{34}Si persists along the isotopic chain.

APPENDIX

Appendix

Appendix A

This appendix contains a figure showing the very few isotopes with known $B_{4/2}$ ratios of less than 1. Figure A1 shows the nuclear landscape with the isotopes with a known $B_{4/2}$ ratio less than one with a colored square. The black lines indicate classical magic numbers and help orient where these isotopes are located in the nuclear landscape. Experimental data taken from NuDat 2.8 [1].

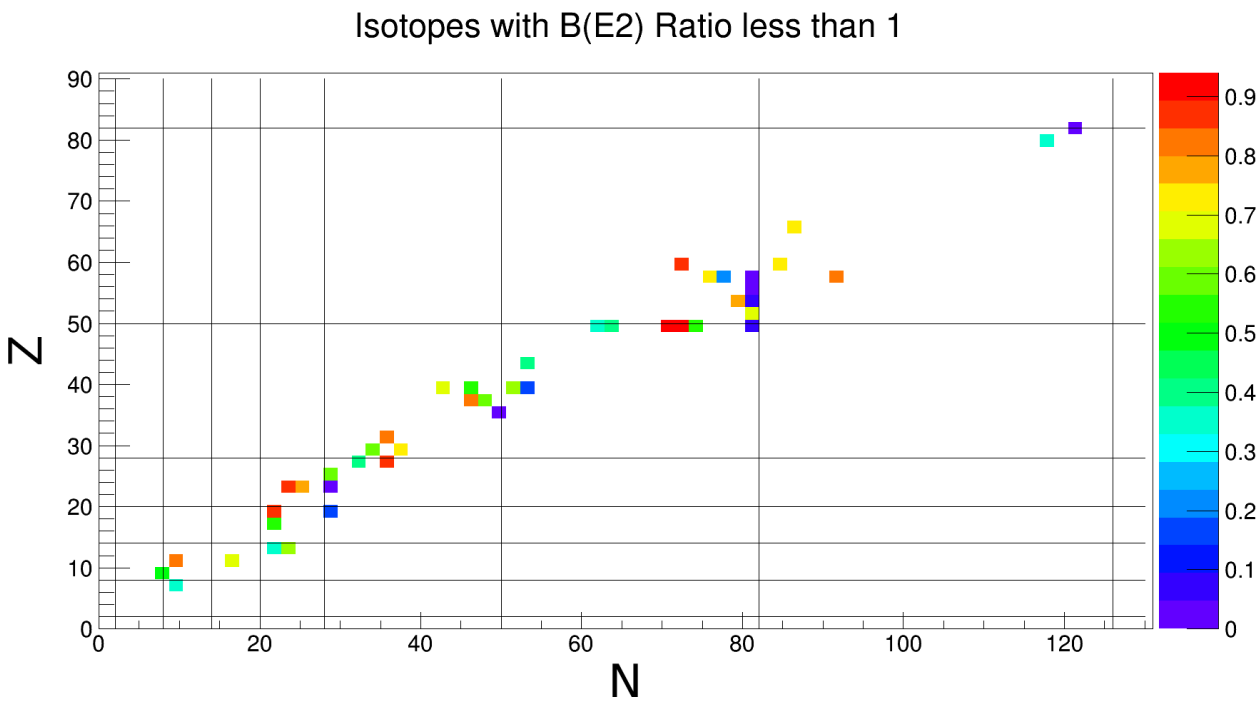

Figure A1: A plot of all isotopes with known B(E2) ratios less than 1. The horizontal axis is the neutron number and the vertical axis is the proton number. The black horizontal lines indicate the standard magic numbers 2,8,20,28,50,82, and 126.

REFERENCES

REFERENCES

[1] National Nuclear Data Center. https://www.nndc.bnl.gov/, 2022. Accessed: 2022-22-06.

[2] Werner Heisenberg. On the structure of atomic nuclei. *Z. Phys*, 77(1), 1932.

[3] Maria Goeppert Mayer. On closed shells in nuclei. ii. *Physical Review*, 75(12):1969, 1949.

[4] Otto Haxel, J Hans D Jensen, and Hans E Suess. On the" magic numbers" in nuclear structure. *Physical Review*, 75(11):1766, 1949.

[5] B. A. Brown. Lecture notes on nuclear structure. 2017.

[6] E. K. Warburton, J. A. Becker, and B. A. Brown. Mass systematics for A=29–44 nuclei: The deformed A∼32 region. *Phys. Rev. C*, 41:1147–1166, Mar 1990.

[7] A Poves and J Retamosa. Onset of deformation at the N= 20 neutron shell closure far from stability. *Phys. Lett. B;(Netherlands)*, 184(4), 1987.

[8] O. Sorlin and M.-G. Porquet. Nuclear magic numbers: New features far from stability. *Progress in Particle and Nuclear Physics*, 61(2):602–673, 2008.

[9] B. Bastin, S. Grévy, D. Sohler, O. Sorlin, Zs. Dombrádi, N. L. Achouri, J. C. Angélique, F. Azaiez, D. Baiborodin, R. Borcea, C. Bourgeois, A. Buta, A. Bürger, R. Chapman, J. C. Dalouzy, Z. Dlouhy, A. Drouard, Z. Elekes, S. Franchoo, S. Iacob, B. Laurent, M. Lazar, X. Liang, E. Liénard, J. Mrazek, L. Nalpas, F. Negoita, N. A. Orr, Y. Penionzhkevich, Zs. Podolyák, F. Pougheon, P. Roussel-Chomaz, M. G. Saint-Laurent, M. Stanoiu, I. Stefan, F. Nowacki, and A. Poves. Collapse of the N = 28 shell closure in ^{42}Si. *Phys. Rev. Lett.*, 99:022503, Jul 2007.

[10] Takaharu Otsuka, Rintaro Fujimoto, Yutaka Utsuno, B. Alex Brown, Michio Honma, and Takahiro Mizusaki. Magic numbers in exotic nuclei and spin-isospin properties of the *NN* interaction. *Phys. Rev. Lett.*, 87:082502, Aug 2001.

[11] Takaharu Otsuka, Toshio Suzuki, Rintaro Fujimoto, Hubert Grawe, and Yoshinori Akaishi. Evolution of nuclear shells due to the tensor force. *Phys. Rev. Lett.*, 95:232502, Nov 2005.

[12] B.A Brown, W.A Richter, R.E Julies, and B.H Wildenthal. Semi-empirical effective interactions for the 1s-od shell. *Annals of Physics*, 182(2):191–236, 1988.

[13] W.-T. Chou, D. S. Brenner, R. F. Casten, and R. L. Gill. Level lifetime measurements and the structure of neutron-rich ^{78}Ge. *Phys. Rev. C*, 47:157–162, Jan 1993.

[14] Yutaka Utsuno, Takaharu Otsuka, B. Alex Brown, Michio Honma, Takahiro Mizusaki, and Noritaka Shimizu. Shape transitions in exotic si and s isotopes and tensor-force-driven jahn-teller effect. *Phys. Rev. C*, 86:051301, Nov 2012.

[15] L. P. Gaffney, P. A. Butler, M. Scheck, A. B. Hayes, F. Wenander, M. Albers, B. Bastin, C. Bauer, A. Blazhev, S. Bönig, N. Bree, J. Cederkäll, T. Chupp, D. Cline, T. E. Cocolios, T. Davinson, H. De Witte, J. Diriken, T. Grahn, A. Herzan, M. Huyse, D. G. Jenkins, D. T. Joss, N. Kesteloot, J. Konki, M. Kowalczyk, Th. Kröll, E. Kwan, R. Lutter, K. Moschner, P. Napiorkowski, J. Pakarinen, M. Pfeiffer, D. Radeck, P. Reiter, K. Reynders, S. V. Rigby, L. M. Robledo, M. Rudigier, S. Sambi, M. Seidlitz, B. Siebeck, T. Stora, P. Thoele, P. Van Duppen, M. J. Vermeulen, M. von Schmid, D. Voulot, N. Warr, K. Wimmer, K. Wrzosek-Lipska, C. Y. Wu, and M. Zielinska. Studies of pear-shaped nuclei using accelerated radioactive beams. *Nature*, 497, 2013.

[16] A. Mutschler, A. Lemasson, O. Sorlin, D. Bazin, C. Borcea, R. Borcea, Z. Dombrádi, J. P. Ebran, A. Gade, H. Iwasaki, E. Khan, A. Lepailleur, F. Recchia, T. Roger, F. Rotaru, D. Sohler, M. Stanoiu, S. R. Stroberg, J. A. Tostevin, M. Vandebrouck, D. Weisshaar, and K. Wimmer. A proton density bubble in the doubly magic ^{34}Si nucleus. *Nature Physics*, page 152156, 2017.

[17] V. F. Weisskopf. Radiative transition probabilities in nuclei. *Phys. Rev.*, 83:1073–1073, Sep 1951.

[18] M. Thoennessen. Discovery of the isotopes with $11 \leq Z \leq 19$. *Atomic Data and Nuclear Data Tables*, 98(5):933–959, 2012.

[19] R. W. Ibbotson, T. Glasmacher, B. A. Brown, L. Chen, M. J. Chromik, P. D. Cottle, M. Fauerbach, K. W. Kemper, D. J. Morrissey, H. Scheit, and M. Thoennessen. Quadrupole collectivity in ^{32,34,36,38}Si and the $N = 20$ shell closure. *Phys. Rev. Lett.*, 80:2081–2084, Mar 1998.

[20] C. M. Campbell, N. Aoi, D. Bazin, M. D. Bowen, B. A. Brown, J. M. Cook, D.-C. Dinca, A. Gade, T. Glasmacher, M. Horoi, S. Kanno, T. Motobayashi, W. F. Mueller, H. Sakurai, K. Starosta, H. Suzuki, S. Takeuchi, J. R. Terry, K. Yoneda, and H. Zwahlen. Measurement of excited states in ^{40}Si and evidence for weakening of the N = 28 shell gap. *Phys. Rev. Lett.*, 97:112501, Sep 2006.

[21] S. Takeuchi, M. Matsushita, N. Aoi, P. Doornenbal, K. Li, T. Motobayashi, H. Scheit, D. Steppenbeck, H. Wang, H. Baba, D. Bazin, L. Càceres, H. Crawford, P. Fallon, R. Gernhäuser, J. Gibelin, S. Go, S. Grévy, C. Hinke, C. R. Hoffman, R. Hughes, E. Ideguchi, D. Jenkins, N. Kobayashi, Y. Kondo, R. Krücken, T. Le Bleis, J. Lee, G. Lee, A. Matta, S. Michimasa, T. Nakamura, S. Ota, M. Petri, T. Sako, H. Sakurai, S. Shimoura, K. Steiger, K. Takahashi, M. Takechi, Y. Togano, R. Winkler, and K. Yoneda. Well developed deformation in ^{42}Si. *Phys. Rev. Lett.*, 109:182501, Nov 2012.

[22] S. R. Stroberg, A. Gade, J. A. Tostevin, V. M. Bader, T. Baugher, D. Bazin, J. S. Berryman, B. A. Brown, C. M. Campbell, K. W. Kemper, C. Langer, E. Lunderberg, A. Lemasson, S. Noji, F. Recchia, C. Walz, D. Weisshaar, and S. J. Williams. Single-particle structure of silicon isotopes approaching ^{42}Si. *Phys. Rev. C*, 90:034301, Sep 2014.

[23] K Steiger, S Nishimura, Z Li, R Gernhäuser, Y Utsuno, R Chen, T Faestermann, C Hinke, R Krücken, M Kurata-Nishimura, et al. Nuclear structure of 37, 38si investigated by decay spectroscopy of 37, 38al. *The European Physical Journal A*, 51(9):1–9, 2015.

[24] A. Gade, B. A. Brown, J. A. Tostevin, D. Bazin, P. C. Bender, C. M. Campbell, H. L. Crawford, B. Elman, K. W. Kemper, B. Longfellow, E. Lunderberg, D. Rhodes, and D. Weisshaar. Is the structure of ^{42}Si understood? *Phys. Rev. Lett.*, 122:222501, Jun 2019.

[25] T. Glasmacher. Coulomb excitation at intermediate energies. *Annual Review of Nuclear and Particle Science*, 48(1):1–31, 1998.

[26] A. Dewald, O. Möller, and P. Petkov. Developing the recoil distance doppler-shift technique towards a versatile tool for lifetime measurements of excited nuclear states. *Progress in Particle and Nuclear Physics*, 67(3):786–839, 2012.

[27] H. Morinaga and P.C. Gugelot. Gamma rays following (α, xn) reactions. *Nuclear Physics*, 46:210–224, 1963.

[28] R. Anne, D. Bazin, R. Bimbot, M.J.G. Borge, J.M. Corre, S. Dogny, H. Emling, D. Guillemaud-Mueller, P.G. Hansen, P. Hornshøj, et al. Projectile coulomb excitation with fast radioactive beams. *Zeitschrift für Physik A Hadrons and Nuclei*, 352(4):397–401, 1995.

[29] T. Motobayashi, Y. Ikeda, K. Ieki, M. Inoue, N. Iwasa, T. Kikuchi, M. Kurokawa, S. Moriya, S. Ogawa, H. Murakami, S. Shimoura, Y. Yanagisawa, T. Nakamura,

Y. Watanabe, M. Ishihara, T. Teranishi, H. Okuno, and R.F. Casten. Large deformation of the very neutron-rich nucleus ^{32}Mg from intermediate-energy coulomb excitation. *Physics Letters B*, 346(1):9–14, 1995.

[30] Alexandra Gade and Thomas Glasmacher. In-beam nuclear spectroscopy of bound states with fast exotic ion beams. *Progress in Particle and Nuclear Physics*, 60(1):161–224, 2008.

[31] Glenn F Knoll. *Radiation Detection and Measurement*. John Wiley & Sons, Chichester, England, 4 edition, August 2010.

[32] D. Weisshaar, D. Bazin, P.C. Bender, C.M. Campbell, F. Recchia, V. Bader, T. Baugher, J. Belarge, M.P. Carpenter, H.L. Crawford, M. Cromaz, B. Elman, P. Fallon, A. Forney, A. Gade, J. Harker, N. Kobayashi, C. Langer, T. Lauritsen, I.Y. Lee, A. Lemasson, B. Longfellow, E. Lunderberg, A.O. Macchiavelli, K. Miki, S. Momiyama, S. Noji, D.C. Radford, M. Scott, J. Sethi, S.R. Stroberg, C. Sullivan, R. Titus, A. Wiens, S. Williams, K. Wimmer, and S. Zhu. The performance of the γ-ray tracking array gretina for γ-ray spectroscopy with fast beams of rare isotopes. *Nuclear Instruments and Methods in Physics Research Section A: Accelerators, Spectrometers, Detectors and Associated Equipment*, 847:187–198, 2017.

[33] P. J. Nolan and J. F. Sharpey-Schafer. The measurement of the lifetimes of excited nuclear states. *Reports on Progress in Physics*, 42(1):1–86, jan 1979.

[34] D.B. Fossan and E.K. Warburton. Vii.h - lifetime measurements. In JOSEPH CERNY, editor, *Nuclear Spectroscopy and Reactions, Part C*, volume 40 of *Pure and Applied Physics*, pages 307–374. Elsevier, 1974.

[35] C. Morse, H. Iwasaki, A. Lemasson, A. Dewald, T. Braunroth, V.M. Bader, T. Baugher, D. Bazin, J.S. Berryman, C.M. Campbell, A. Gade, C. Langer, I.Y. Lee, C. Loelius, E. Lunderberg, F. Recchia, D. Smalley, S.R. Stroberg, R. Wadsworth, C. Walz, D. Weisshaar, A. Westerberg, K. Whitmore, and K. Wimmer. Lifetime measurement of the 2_1^+ state in ^{74}Rb and isospin properties of quadrupole transition strengths at N=Z. *Physics Letters B*, 787:198–203, 2018.

[36] H Iwasaki, A Lemasson, C Morse, A Dewald, T Braunroth, V.M Bader, T Baugher, D Bazin, J.S Berryman, C.M Campbell, et al. Evolution of collectivity in 74Kr: Evidence for rapid shape transition. *Physical Review Letters*, 112(14):142502, 2014.

[37] I. Deloncle, B. Roussière, M. A. Cardona, D. Hojman, J. Kiener, P. Petkov, D. Tonev, and T.s. Venkova. Fast timing: Lifetime measurements with LaBrsub3/subscintillators. *Journal of Physics: Conference Series*, 205:012044, jan 2010.

[38] A.B. Garnsworthy, C.E. Svensson, M. Bowry, R. Dunlop, A.D. MacLean, B. Olaizola, J.K. Smith, F.A. Ali, C. Andreoiu, J.E. Ash, W.H. Ashfield, G.C. Ball, T. Ballast, C. Bartlett, Z. Beadle, P.C. Bender, N. Bernier, S.S. Bhattacharjee, H. Bidaman, V. Bildstein, D. Bishop, P. Boubel, R. Braid, D. Brennan, T. Bruhn, C. Burbadge, A. Cheeseman, A. Chester, R. Churchman, S. Ciccone, R. Caballero-Folch, D.S. Cross, S. Cruz, B. Davids, A. Diaz Varela, I. Dillmann, M.R. Dunlop, L.J. Evitts, F.H. Garcia, P.E. Garrett, S. Georges, S. Gillespie, R. Gudapati, G. Hackman, B. Hadinia, S. Hallam, J. Henderson, S.V. Ilyushkin, B. Jigmeddorj, A.I. Kilic, D. Kisliuk, R. Kokke, K. Kuhn, R. Krücken, M. Kuwabara, A.T. Laffoley, R. Lafleur, K.G. Leach, J.R. Leslie, Y. Linn, C. Lim, E. MacConnachie, A.R. Mathews, E. McGee, J. Measures, D. Miller, W.J. Mills, W. Moore, D. Morris, L.N. Morrison, M. Moukaddam, C.R. Natzke, K. Ortner, E. Padilla-Rodal, O. Paetkau, J. Park, H.P. Patel, C.J. Pearson, E. Peters, E.E. Peters, J.L. Pore, A.J. Radich, M.M. Rajabali, E.T. Rand, K. Raymond, U. Rizwan, P. Ruotsalainen, Y. Saito, F. Sarazin, B. Shaw, J. Smallcombe, D. Southall, K. Starosta, M. Ticu, E. Timakova, J. Turko, R. Umashankar, C. Unsworth, Z.M. Wang, K. Whitmore, S. Wong, S.W. Yates, E.F. Zganjar, and T. Zidar. The griffin facility for decay-spectroscopy studies at triumf-isac. *Nuclear Instruments and Methods in Physics Research Section A: Accelerators, Spectrometers, Detectors and Associated Equipment*, 918:9–29, 2019.

[39] NSCL, Michigan State University. Nscl history. https://nscl.msu.edu/about/history.html, 2020. Accessed: 2022-07-03.

[40] D.J. Morrissey. The coupled cyclotron project at the nscl. *Nuclear Physics A*, 616(1):045055, 1997. Radioactive Nuclear Beams.

[41] Jie Wei, Hiroyuki Ao, Steven Beher, Nathan Bultman, Fabio Casagrande, S Cogan, C Compton, J Curtin, L Dalesio, K Davidson, et al. Advances of the FRIB project. *International Journal of Modern Physics E*, 28(3):1930003, 2019.

[42] A Gade and B M Sherrill. NSCL and FRIB at michigan state university: Nuclear science at the limits of stability. *Physica Scripta*, 91(5):053003, apr 2016.

[43] P.A. Zavodszky, B. Arend, D. Cole, J. DeKamp, G. Machicoane, F. Marti, P. Miller, J. Moskalik, J. Ottarson, J. Vincent, and A. Zeller. Design of susi – superconducting source for ions at nscl/msu – ii. the conventional parts. *Nuclear Instruments and Methods in Physics Research Section B: Beam Interactions with Materials and Atoms*, 241(1):959–964, 2005. The Application of Accelerators in Research and Industry.

[44] D.J. Morrissey, B.M. Sherrill, M. Steiner, A. Stolz, and I. Wiedenhoever. Commissioning the a1900 projectile fragment separator. *Nuclear Instruments and Methods in Physics Research Section B: Beam Interactions with Materials and Atoms*, 204:90–96, 2003.

14th International Conference on Electromagnetic Isotope Separators and Techniques Related to their Applications.

[45] T. Mijatović, N. Kobayashi, H. Iwasaki, D. Bazin, J. Belarge, P. C. Bender, B. A. Brown, A. Dewald, R. Elder, B. Elman, A. Gade, M. Grinder, T. Haylett, S. Heil, C. Loelius, B. Longfellow, E. Lunderberg, M. Mathy, K. Whitmore, and D. Weisshaar. Lifetime measurements and triple coexisting band structure in ^{43}S. *Phys. Rev. Lett.*, 121:012501, Jul 2018.

[46] C. Loelius, N. Kobayashi, H. Iwasaki, D. Bazin, J. Belarge, P. C. Bender, B. A. Brown, R. Elder, B. Elman, A. Gade, M. Grinder, S. Heil, A. Hufnagel, B. Longfellow, E. Lunderberg, M. Mathy, T. Otsuka, M. Petri, I. Syndikus, N. Tsunoda, D. Weisshaar, and K. Whitmore. Enhanced electric dipole strength for the weakly bound states in ^{27}Ne. *Phys. Rev. Lett.*, 121:262501, Dec 2018.

[47] I.Y. Lee. Gamma-ray tracking detectors. *Nuclear Instruments and Methods in Physics Research Section A: Accelerators, Spectrometers, Detectors and Associated Equipment*, 422(1-3):195–200, 1999.

[48] GRETINA Users Executive Committee. Greta whitepaper. https://drive.google.com/file/d/1Yd63o8VGzKNXSiBvorBlgaD26TF73NEB/view, 2014. Accessed: 2022-07-16.

[49] S. Paschalis, I.Y. Lee, A.O. Macchiavelli, C.M. Campbell, M. Cromaz, S. Gros, J. Pavan, J. Qian, R.M. Clark, H.L. Crawford, D. Doering, P. Fallon, C. Lionberger, T. Loew, M. Petri, T. Stezelberger, S. Zimmermann, D.C. Radford, K. Lagergren, D. Weisshaar, R. Winkler, T. Glasmacher, J.T. Anderson, and C.W. Beausang. The performance of the gamma-ray energy tracking in-beam nuclear array gretina. *Nuclear Instruments and Methods in Physics Research Section A: Accelerators, Spectrometers, Detectors and Associated Equipment*, 709:44–55, 2013.

[50] C. Loelius, H. Iwasaki, B. A. Brown, M. Honma, V. M. Bader, T. Baugher, D. Bazin, J. S. Berryman, T. Braunroth, C. M. Campbell, A. Dewald, A. Gade, N. Kobayashi, C. Langer, I. Y. Lee, A. Lemasson, E. Lunderberg, C. Morse, F. Recchia, D. Smalley, S. R. Stroberg, R. Wadsworth, C. Walz, D. Weisshaar, A. Westerberg, K. Whitmore, and K. Wimmer. Lifetime measurement of the 4_1^+ state of ^{58}Ni with the recoil distance method. *Phys. Rev. C*, 94:024340, Aug 2016.

[51] Charles Robert Loelius. *Electromagnetic Transition Strengths Studied with Doppler-Shift Techniques Across the Contours of the Valley of Stability.* PhD thesis, Michigan State University, East Lansing, MI, 2017.

[52] D. Bazin, J.A. Caggiano, B.M. Sherrill, J. Yurkon, and A. Zeller. The s800 spectrograph. *Nuclear Instruments and Methods in Physics Research Section B: Beam Interactions with Materials and Atoms*, 204:629–633, 2003. 14th International Conference on Electromagnetic Isotope Separators and Techniques Related to their Applications.

[53] H. Iwasaki, A. Dewald, T. Braunroth, C. Fransen, D. Smalley, A. Lemasson, C. Morse, K. Whitmore, and C. Loelius. The triple plunger for exotic beams triplex for excited-state lifetime measurement studies on rare isotopes. *Nuclear Instruments and Methods in Physics Research Section A: Accelerators, Spectrometers, Detectors and Associated Equipment*, 806:123–131, 2016.

[54] A. Chester, G.C. Ball, N. Bernier, D.S. Cross, T. Domingo, T.E. Drake, L.J. Evitts, F.H. Garcia, A.B. Garnsworthy, G. Hackman, et al. Recoil distance method lifetime measurements at triumf-isac using the tigress integrated plunger. *Nuclear Instruments and Methods in Physics Research Section A: Accelerators, Spectrometers, Detectors and Associated Equipment*, 882:69–83, 2018.

[55] M.J. Taylor, D.M. Cullen, A.J. Smith, A. McFarlane, V. Twist, G.A. Alharshan, M.G. Procter, T. Braunroth, A. Dewald, E. Ellinger, et al. A new differentially pumped plunger device to measure excited-state lifetimes in proton emitting nuclei. *Nuclear Instruments and Methods in Physics Research Section A: Accelerators, Spectrometers, Detectors and Associated Equipment*, 707:143–148, 2013.

[56] J. Ljungvall, G. Georgiev, S. Cabaret, N. Karkour, D. Linget, G. Sedes, Rémy Chevrier, I. Matea, M. Niikura, M.D Salsac, et al. The orsay universal plunger system. *Nuclear Instruments and Methods in Physics Research Section A: Accelerators, Spectrometers, Detectors and Associated Equipment*, 679:61–66, 2012.

[57] W.F. Mueller, J.A. Church, T. Glasmacher, D. Gutknecht, G. Hackman, P.G. Hansen, Z. Hu, K.L. Miller, and P. Quirin. Thirty-two-fold segmented germanium detectors to identify γ-rays from intermediate-energy exotic beams. *Nuclear Instruments and Methods in Physics Research Section A: Accelerators, Spectrometers, Detectors and Associated Equipment*, 466(3):492–498, 2001.

[58] Rene Brun and Fons Rademakers. Root—an object oriented data analysis framework. *Nuclear instruments and methods in physics research section A: accelerators, spectrometers, detectors and associated equipment*, 389(1-2):81–86, 1997.

[59] A. Lemasson, H. Iwasaki, C. Morse, D. Bazin, T. Baugher, J. S. Berryman, A. Dewald, C. Fransen, A. Gade, S. McDaniel, A. Nichols, A. Ratkiewicz, S. Stroberg, P. Voss, R. Wadsworth, D. Weisshaar, K. Wimmer, and R. Winkler. Observation of mutually enhanced collectivity in self-conjugate $^{76}_{38}\mathrm{Sr}_{38}$. *Phys. Rev. C*, 85:041303, Apr 2012.

[60] P. Adrich, D. Enderich, D. Miller, V. Moeller, R.P. Norris, K. Starosta, C. Vaman, P. Voss, and A. Dewald. A simulation tool for recoil distance method lifetime measurements at nscl. *Nuclear Instruments and Methods in Physics Research Section A: Accelerators, Spectrometers, Detectors and Associated Equipment*, 598(2):454–464, 2009.

[61] S. Agostinelli, J. Allison, K. Amako, J. Apostolakis, H. Araujo, P. Arce, M. Asai, D. Axen, S. Banerjee, G. Barrand, F. Behner, L. Bellagamba, J. Boudreau, L. Broglia, A. Brunengo, H. Burkhardt, S. Chauvie, J. Chuma, R. Chytracek, G. Cooperman, G. Cosmo, P. Degtyarenko, A. Dell'Acqua, G. Depaola, D. Dietrich, R. Enami, A. Feliciello, C. Ferguson, H. Fesefeldt, G. Folger, F. Foppiano, A. Forti, S. Garelli, S. Giani, R. Giannitrapani, D. Gibin, J.J. Gómez Cadenas, I. González, G. Gracia Abril, G. Greeniaus, W. Greiner, V. Grichine, A. Grossheim, S. Guatelli, P. Gumplinger, R. Hamatsu, K. Hashimoto, H. Hasui, A. Heikkinen, A. Howard, V. Ivanchenko, A. Johnson, F.W. Jones, J. Kallenbach, N. Kanaya, M. Kawabata, Y. Kawabata, M. Kawaguti, S. Kelner, P. Kent, A. Kimura, T. Kodama, R. Kokoulin, M. Kossov, H. Kurashige, E. Lamanna, T. Lampén, V. Lara, V. Lefebure, F. Lei, M. Liendl, W. Lockman, F. Longo, S. Magni, M. Maire, E. Medernach, K. Minamimoto, P. Mora de Freitas, Y. Morita, K. Murakami, M. Nagamatu, R. Nartallo, P. Nieminen, T. Nishimura, K. Ohtsubo, M. Okamura, S. O'Neale, Y. Oohata, K. Paech, J. Perl, A. Pfeiffer, M.G. Pia, F. Ranjard, A. Rybin, S. Sadilov, E. Di Salvo, G. Santin, T. Sasaki, N. Savvas, Y. Sawada, S. Scherer, S. Sei, V. Sirotenko, D. Smith, N. Starkov, H. Stoecker, J. Sulkimo, M. Takahata, S. Tanaka, E. Tcherniaev, E. Safai Tehrani, M. Tropeano, P. Truscott, H. Uno, L. Urban, P. Urban, M. Verderi, A. Walkden, W. Wander, H. Weber, J.P. Wellisch, T. Wenaus, D.C. Williams, D. Wright, T. Yamada, H. Yoshida, and D. Zschiesche. Geant4—a simulation toolkit. *Nuclear Instruments and Methods in Physics Research Section A: Accelerators, Spectrometers, Detectors and Associated Equipment*, 506(3):250–303, 2003.

[62] M Shamsuzzoha Basunia. Nuclear data sheets for A= 30. *Nuclear Data Sheets*, 111(9):2331–2424, 2010.

[63] C.M. Campbell, N. Aoi, D. Bazin, M.D. Bowen, B.A. Brown, J.M. Cook, D.-C. Dinca, A. Gade, T. Glasmacher, M. Horoi, S. Kanno, T. Motobayashi, L.A. Riley, H. Sagawa, H. Sakurai, K. Starosta, H. Suzuki, S. Takeuchi, J.R. Terry, K. Yoneda, and H. Zwahlen. Quadrupole collectivity in silicon isotopes approaching neutron number N=28. *Physics Letters B*, 652(4):169–173, 2007.

[64] C. Morse, E.A. McCutchan, H. Iwasaki, C.J. Lister, V.M. Bader, D. Bazin, S. Beceiro Novo, P. Chowdhury, A. Gade, T.D. Johnson, et al. Enhanced collectivity in ^{12}Be. *Physics Letters B*, 780:227–232, 2018.

[65] J. P. Delaroche, M. Girod, J. Libert, H. Goutte, S. Hilaire, S. Péru, N. Pillet, and G. F. Bertsch. Structure of even-even nuclei using a mapped collective hamiltonian and the D1S gogny interaction. *Phys. Rev. C*, 81:014303, Jan 2010.

[66] W. Kutschera, B.A. Brown, and K. Ogawa. The empirical $(1f^n_{7/2}$ model. *Riv. Nuovo Cim*, 1(12):1–116, 1978.

[67] Andrew Ratkiewicz. *Collectivity of Exotic Silicon Isotopes*. PhD thesis, Michigan State University, East Lansing, MI, 2011.

ProQuest Number: 29326195

INFORMATION TO ALL USERS
The quality and completeness of this reproduction is dependent on the quality
and completeness of the copy made available to ProQuest.

Distributed by ProQuest LLC (2022).
Copyright of the Dissertation is held by the Author unless otherwise noted.

This work may be used in accordance with the terms of the Creative Commons license
or other rights statement, as indicated in the copyright statement or in the metadata
associated with this work. Unless otherwise specified in the copyright statement
or the metadata, all rights are reserved by the copyright holder.

This work is protected against unauthorized copying under Title 17,
United States Code and other applicable copyright laws.

Microform Edition where available © ProQuest LLC. No reproduction or digitization
of the Microform Edition is authorized without permission of ProQuest LLC.

ProQuest LLC
789 East Eisenhower Parkway
P.O. Box 1346
Ann Arbor, MI 48106 - 1346 USA